

**MEASUREMENT OF MUON NEUTRINO
CHARGED-CURRENT HIGH Q^2 DIFFERENTIAL
CROSS-SECTION USING THE PI-ZERO
DETECTOR AT T2K**

by

Damon Hansen

B.A in Physics,
B.A in Philosophy,
College of Charleston, 2007

Submitted to the Graduate Faculty of
the Kenneth P. Dietrich School of Arts and Sciences in partial
fulfillment

of the requirements for the degree of
Doctor of Philosophy in Physics and Astronomy

University of Pittsburgh

2017

UNIVERSITY OF PITTSBURGH

KENNETH P. DIETRICH SCHOOL OF ARTS AND SCIENCES

This dissertation was presented

by

Damon Hansen

It was defended on

April 26, 2017

and approved by

Vittorio Paolone, Ph.D

Donna Naples, Ph.D

Tao Han, Ph.D

Michael Wood-Vasey, Ph.D

Roy Briere, Ph.D

Dissertation Director: Vittorio Paolone, Ph.D

ABSTRACT

MEASUREMENT OF MUON NEUTRINO CHARGED-CURRENT HIGH Q^2 DIFFERENTIAL CROSS-SECTION USING THE PI-ZERO DETECTOR AT T2K

Damon Hansen, PhD

University of Pittsburgh, 2017

Tokai-to-Kamioka (T2K) is a long baseline neutrino oscillation experiment. A high intensity beam of muon neutrinos is produced at the Japan Proton Accelerator Research Complex (J-PARC) and travels 295 km across Japan towards the Super-Kamiokande (SuperK) water Cherenkov detector. A suite of near detectors (ND280) is located 280 m downstream of the production point and contained within a 0.2 T dipole magnet. The Pi-Zero Detector (P \emptyset D) is a component of the near detector complex. The P \emptyset D is designed to constrain the π^0 background at SuperK, and is optimized to detect electromagnetic showers. It is composed of alternating layers of plastic scintillator and water targets which can be drained or filled, allowing for measurements in both a “water-in” and “water-out” configuration. The neutrino beam is directed 2.5° off-axis to produce a flux peaked at ~ 600 MeV at the near and far detectors. For this paper, the total beam used is 2.5×10^{20} protons on target (p.o.t) for water-in running, and 3.6×10^{20} p.o.t for water-out.

This thesis will present the selection for a P \emptyset D-contained charged-current 0-pion (CC- 0π) single-track sample in both water-in and water-out modes. This selection is the first P \emptyset D-specific analysis to be implemented fully in the ND280 analysis framework, Highland2. Several tools were developed to determine the directionality of P \emptyset D tracks, and this selection

is also the first P θ D analysis to use the full angular phase-space of the out-going muon. A Bayesian unfolding engine is then used to calculate the double differential CC-0 π cross-section on water. The results are presented in bins of the reconstructed muon momentum, p_μ , and angle from the neutrino direction, $\cos(\theta_\mu)$ for both data and Monte Carlo fake data.

TABLE OF CONTENTS

1.0 NEUTRINO INTERACTIONS AND OSCILLATIONS	1
1.1 A Brief History of Neutrinos	1
1.2 The Standard Model	2
1.2.1 Weak Interactions	4
1.2.2 Neutrino Interaction Modes	7
1.2.3 Current Charged-Current Quasi-Elastic Measurements	10
1.3 Neutrino Oscillations	11
2.0 THE T2K EXPERIMENT	17
2.1 Beam and Neutrino Production	18
2.1.1 J-PARC	19
2.1.2 T2K Neutrino Beamline	20
2.1.2.1 Primary Beamline	21
2.1.2.2 Secondary Beamline	21
2.1.3 Neutrino Flux Prediction	23
2.2 Near Detectors	23

2.2.1	INGRID	24
2.2.2	The PØD	27
2.2.3	The Tracker	31
2.2.4	The Electromagnetic Calorimeters	32
2.2.5	The Side Muon Range Detector	33
2.3	Super Kamiokande	33
2.4	T2K Software	35
2.4.1	Data Collection	35
2.4.2	Reconstruction	37
2.4.2.1	PØD Reconstruction	38
2.4.2.2	Hit Preparation	39
2.4.2.3	Tracking Reconstruction	40
2.4.2.4	Michel Tagging	41
2.4.3	Analysis Software	42
3.0	THE PØD-CONTAINED ν_μ CC-0π ANALYSIS	44
3.1	Analysis Strategy	45
3.2	Selection Criteria	47
3.2.1	Event Quality	48
3.2.2	One and Only One PØD Track	49
3.2.3	No Other GlobaRecon Objects	49
3.2.4	Track is Fully Contained	49

3.2.5	Vertex in the Fiducial Volume	50
3.2.6	Momentum Reconstruction	50
3.2.7	Direction Criteria	54
3.2.8	Proton/Muon Particle Identification	58
3.2.9	Selection Kinematics	59
3.3	Water Subtraction Method	68
3.3.1	Bayesian Unfolding	68
3.3.1.1	Background	71
3.3.2	Fake Data Studies	75
4.0	SYSTEMATIC ERRORS	92
4.1	Flux & Interaction Systematics	92
4.2	Detector Systematics	95
4.2.1	P \emptyset D Mass	97
4.2.2	Out of Fiducial Volume	98
4.2.3	Angular Resolution	100
4.2.4	Backward Track Selection	101
4.2.5	Particle ID Pull	104
4.2.6	P \emptyset D Energy Scale	106
4.3	Total Systematic Uncertainty	108
5.0	RESULTS	110
5.1	Fake Data	110

5.2 Data	119
6.0 SUMMARY	130
APPENDIX A. NEUTRINO MIXING PARAMETERS	132
APPENDIX B. MAJORANA AND DIRAC NEUTRINOS	134
BIBLIOGRAPHY	135

LIST OF TABLES

1	Table of M_A Values	10
2	Event Rate by Cut	48
3	PØD DAQ Efficiency	49
4	PØD Material Density	53
5	Table of Directional Variables	56
6	Event Topologies in Final Selection	67
7	T2KReWeight CCQE Dials	96
8	PØD Mass Uncertainties	98
9	Out of Fiducial Volume Rates	99
10	Δ_{time} Systematic Values	104
11	ADC Values for Water-In and Water-Out Mode	107
12	Uncertainty on Total Cross-Section by Error Source	109
13	Current ν Oscillation Parameters	133

LIST OF FIGURES

1	The Particle of the Standard Model	3
2	Charged and Neutral Current Feynman Diagrams	4
3	Total ν_μ Cross-Section by E_ν	8
4	Existing ν_{μ} Quasi-Elastic Scattering Cross-Sections	11
5	The Invisible Partial Width of Z^0	12
6	The PMNS Neutrino Mixing Matrix	13
7	The T2K Experiment	17
8	E_ν as a Function of E_π	19
9	The Survival Probability of Muon Neutrinos at SuperK	20
10	The T2K Neutrino Beamline	21
11	The Secondary Beamline	21
12	The Magnetic Horns	22
13	The Horn Current	22
14	The Flux Prediction Flow Diagram	24
15	The Near Detector Complex	25

16	The Off-Axis Detector	25
17	The INGRID on-axis detector	26
18	A Schematic of an INGRID module	27
19	The Pi-Zero Detector	29
20	The charge amplitude spectrum of a MPPC	30
21	A diagram of a TPC	32
22	A Diagram of Super Kamiokande	34
23	Reconstructed T2K events at SuperK	34
24	A comparison of NEUT $\nu_\mu n \rightarrow \mu^- p$ to data	37
25	A comparison of GENIE $\nu_\mu n \rightarrow \mu^- p$ to data	38
26	A Flow Diagram of the P \emptyset D Reconstruction Software	39
27	Diagram of Kinematics Definitions	45
28	Containment Diagram	51
29	Bethe-Bloch	52
30	Momentum Resolution Vs Length	54
31	Muon Momentum Resolution	54
32	Δ_{time} for Data and MC	57
33	Sand muon Charge Profile	59
34	Proton/Muon PID by particle	60
35	Water-In Reconstructed Muon Kinematics	62
36	Water-Out Reconstructed Muon Kinematics	63

37	Water-In Selection Efficiency	64
38	Water-out Selection Efficiency	65
39	Muon Phase Space: Water-In	66
40	Muon Phase Space: Water-Out	66
41	Diagram of the Bayesian Binning Scheme	69
42	Toy MC Unfolding Results	71
43	Binning Schematic	72
44	Differential Cross-Section by Iterations: Water-in NEUT Fake Data	76
45	Differential Cross-Section by Iterations: Water-out NEUT Fake Data	77
46	Differential Cross-Section by Iterations: Water-in Genie Fake Data	78
47	Differential Cross-Section by Iterations: Water-out Genie Fake Data	79
48	Fractional Bias by bin: NEUT Fake Data	81
49	Fractional Bias by bin: GENIE Fake Data	82
50	Unfolded Cross-Section by Iterations: CC Resonance @ 50%	84
51	Unfolded Cross-Section by Iterations: CC Resonance @ 150%	85
52	Absolute Bias by Bin: Reweighted CC Resonance	86
53	Unfolded Cross-Section by Iterations: M_A^{CCQE} @ 50%	87
54	Unfolded Cross-Section by Iterations: M_A^{CCQE} @ 150%	88
55	Absolute Bias by Bin: Reweighted M_A^{CCQE}	89
56	Unfolded Cross-Section: Reweighted Fake Data	90
57	Absolute Bias by Bin: Reweighted by Formula	91

58	Spectral Function and RFG $\nu/\bar{\nu}$ QE Spectra	94
59	Angular Resolution for Water-In	102
60	Variance of PID Pull Variable	106
61	Water-In Fake Data Cross-Section Results by Bin	111
62	Water-Out Fake Data Cross-Section Results by Bin	111
63	On-Water Fake Data Cross-Section Results by Bin	112
64	Water-In Cross-Section for Fake Data by Angle: $\text{Cos } \theta < 0$	113
65	Water-In Cross-Section for Fake Data by Angle: $\text{Cos } \theta > 0$	114
66	Water-Out Cross-Section for Fake Data by Angle: $\text{Cos } \theta < 0$	115
67	Water-Out Cross-Section for Fake Data by Angle: $\text{Cos } \theta > 0$	116
68	On-Water Cross-Section for Fake Data by Angle: $\text{Cos } \theta < 0$	117
69	On-Water Cross-Section for Fake Data by Angle: $\text{Cos } \theta > 0$	118
70	Water-In Reconstructed Muon Kinematics	120
71	Water-Out Reconstructed Muon Kinematics	121
72	Water-In Cross-Section Results by Bin	122
73	Water-Out Cross-Section Results by Bin	122
74	On-Water Cross-Section Results by Bin	123
75	Water-In Cross-Section by Angle: $\text{Cos } \theta < 0$	124
76	Water-In Cross-Section by Angle: $\text{Cos } \theta > 0$	125
77	Water-Out Cross-Section by Angle: $\text{Cos } \theta < 0$	126
78	Water-Out Cross-Section by Angle: $\text{Cos } \theta > 0$	127

79	On-Water Cross-Section by Angle: $\text{Cos } \theta < 0$	128
80	On-Water Cross-Section by Angle: $\text{Cos } \theta > 0$	129
81	The PMNS Neutrino Mixing Matrix	134

1.0 NEUTRINO INTERACTIONS AND OSCILLATIONS

The following sections will provide an overview of both the historical development and the current state of particle physics, with an emphasis on how each pertains to neutrino physics.

1.1 A BRIEF HISTORY OF NEUTRINOS

The existence of the neutrino was first proposed in 1930 by Wolfgang Pauli to account for the continuous spectrum of the kinetic energy of the electron in beta decay[1]. He speculated that a light, electrically neutral third particle must be involved in some way. He also apologized for positing the existence of such a particle, as he doubted that it could ever be detected. While he correctly anticipated the difficulty of the task, the neutrino was indeed discovered 26 years later at the Savannah River Plant[2] (technically it was the anti-electron neutrino that was first observed).

In 1968, the Davis experiment reported the first measurements of the neutrino flux from fusion reactions in the sun[3]. Located nearly a mile underground at the Homestake mine in South Dakota, a 500 ton tank of C_2Cl_4 was used as a target to capture solar neutrinos and produce ^{37}Ar via inverse beta decay (at a rate of ~ 0.5 atoms per day!). The flux was then determined by counting the number of argon atoms found in the tank. However, the observed rate was only a third of what was predicted[4]. Over the next 20

years, further experiments[5][6][7] would confirm this discrepancy, which became known as the *solar neutrino problem*.

Bruno Pontecorvo suggested neutrino oscillations as a possible explanation almost immediately[8], but confirmation would have to wait until the end of the century¹. Three experiments together gave unequivocal evidence that neutrinos of one flavor can transform in transit to another flavor. Super Kamiokande provided the first convincing signs in 1999[9]. By measuring the ratio $\frac{\nu_\mu}{\nu_e}$ from atmospheric neutrinos as a function of zenith angle, researchers could show a deficit of ν_μ depending on the distance traveled just as predicted. Two years later, the Sudberry Neutrino Observatory, a heavy-water Cherenkov detector sensitive to all three flavors, confirmed that the solar neutrino problem was no problem at all, when you know what to look for[10][11].

1.2 THE STANDARD MODEL

The overarching goal of particle physics research is to describe the universe in terms of a small set of fundamental interactions and particles. By our current understanding, the Standard Model is that set. It encompasses the electromagnetic, weak, and strong forces, their associated gauge bosons, and 12 fundamental particles (see Figure 1). The subset of the Standard Model that describes the strong force is quantum chromodynamics (QCD), while the electromagnetic and weak forces can be unified into a singular “electroweak” force described by the Glashow-Weinberg-Salam (GWS) model.

There are 12 fermions (spin 1/2 particles) in the Standard Model, which are divided into quarks and leptons. Quarks are not known to exist in isolation. Rather, they are found in combinations of quark-antiquark pairs (mesons) or quark/antiquark triplets (baryons)².

¹Pontecorvo had already anticipated neutrino oscillations as a possible phenomenon a decade earlier as a lepton analog of neutral meson mixing

²Other combinations of quarks are possible in theory, and there have been hints of both tetraquarks[12][13] and pentaquarks[14] experimentally (four and five quark particles, respectively). However, it is not yet clear if these states are particles in their own right or “molecules” of known mesons and baryons.

There are three generations of the six quarks: up/down, strange/charm, and top/bottom. The up, charm, and top quarks each have a charge of $+\frac{1}{3}e$, while the other three each have a charge of $-\frac{2}{3}e$, where e is the charge of the electron. The six leptons are also divided into three generations, often referred to as the electron, muon, and tau “flavors.” Each generation consists of a lepton with charge $-e$ and a neutral neutrino. The flavor of a particular neutrino is defined by the charged lepton associated with it in an interaction with a W^\pm (see Section 1.2.1).

Interactions between fermions are mediated by twelve gauge bosons (spin 1 particles). Charged particles interact via the electromagnetic force, propagated by the photon. The weak force acts on all quarks and leptons and is carried by the two charged W bosons and the neutral Z boson. There are eight gluons associated with the strong force. These mediate interactions only between the quarks and other gluons. While gauge bosons are *ipso facto* massless, the W^\pm and Z bosons have been experimentally determined to be massive. This fact led to the postulation of the Higgs mechanism, which claims that these bosons become “heavy” by interacting with a non-zero scalar field. The Higgs boson associated with this field was discovered in CERN in 2013[15][16], experimentally confirming the final fundamental particle of the Standard Model.

mass →	$\approx 2.3 \text{ MeV}/c^2$	$\approx 1.275 \text{ GeV}/c^2$	$\approx 173.07 \text{ GeV}/c^2$	0	$\approx 126 \text{ GeV}/c^2$
charge →	$2/3$	$2/3$	$2/3$	0	0
spin →	$1/2$	$1/2$	$1/2$	1	0
	u up	c charm	t top	g gluon	H Higgs boson
	d down	s strange	b bottom	γ photon	
	e electron	μ muon	τ tau	Z Z boson	
	ν_e electron neutrino	ν_μ muon neutrino	ν_τ tau neutrino	W W boson	
	$0.511 \text{ MeV}/c^2$	$105.7 \text{ MeV}/c^2$	$1.777 \text{ GeV}/c^2$	$91.2 \text{ GeV}/c^2$	$80.4 \text{ GeV}/c^2$
	-1	-1	-1	0	± 1
	$1/2$	$1/2$	$1/2$	1	1

Figure 1: A table of the 12 fermions and 13 bosons of the Standard Model[17]

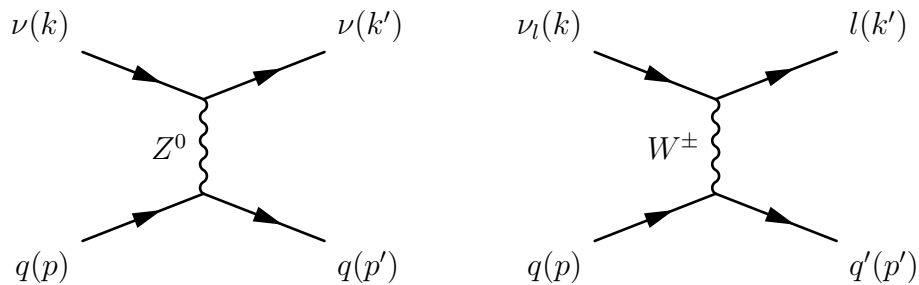


Figure 2: The neutral current (left) and charged current (right) tree level diagrams for a neutrino scattering off a free quark.

1.2.1 Weak Interactions

Since neutrinos are electrically neutral leptons, they can only interact via the weak force, which is mediated by three bosons: the W^+ , W^- , and Z bosons. Interactions involving W^\pm are *charged current (CC) interactions*, as they involve a transfer of electric charge, while those involving the Z boson are *neutral current (NC) interactions* (Figure 2). Charged current interactions cannot change a lepton from one flavor to another, but they necessarily change a lepton into its partner of the same generation.

In 1957, it was discovered that weak interactions do not conserve parity [18]. A sample of the unstable isotope ^{60}Co was aligned in a uniform magnetic field, and the directional preference for the outgoing β particle was measured. The field was then reversed and the measurement repeated. Not only was there a preferred direction for the emission of the electron, the asymmetry appeared to be maximal. The process $^{60}\text{Co} \rightarrow ^{60}\text{Ni} + e + \bar{\nu}_e$ occurred exclusively with a *right-handed* anti-neutrino ($\bar{\nu}_R$) and a *left-handed* electron (e_L)³.

To capture this behavior, the weak charged and neutral currents (for leptons) take the form

³The handed-ness of a particle describes the relative orientations of its momentum and its spin. For a right-handed particle, its intrinsic spin is aligned in its direction of motion; for a left-handed particle it is contra-aligned. While absolute left- and right-handedness only holds for massless particles, this convention is also used for massive and non-relativistic particles.

$$\begin{aligned}
J_\mu^{CC} &= \frac{g_w}{2\sqrt{2}} (\bar{\nu} \gamma_\mu (1 - \gamma^5) l) + h.c. \\
&= \bar{\nu}_L \gamma_\mu l_L + h.c.
\end{aligned}
\tag{1.1}$$

$$J_\mu^{NC} = \frac{g_w}{\sqrt{2}} \rho (\bar{l} \gamma_\mu (c_V - c_A \gamma^5) l) + h.c.
\tag{1.2}$$

where γ are the Dirac matrices, ρ is a proportionality term for the relative strengths of the neutral and charged currents, g_w is the coupling strength of the weak force, and the subscript l has been dropped from ν_l with the understanding that only leptons of the same flavor can interact via the charged current. The $(c_V - c_A \gamma^5)$ structure of the weak interaction vertex is often referred to as the *V-A* or *Vector-Axial* nature of the weak force, with c_V and c_A experimentally determined normalizations of the relative size of each component. If $c_V = c_A$, this operator also acts as a projection operator, selecting out the left-handed component of the fermion fields. In general, $c_V \neq c_A$, and the neutral current contains both right- and left-handed components. For neutrinos, these coefficients are equivalent, and the *V-A* interference is maximal.

The interaction Lagrangian is given by

$$\begin{aligned}
\mathcal{L}_{int} &= \mathcal{L}_{CC} + \mathcal{L}_{NC} \\
&= -iJ_{CC}^\mu W_\mu - iJ_{NC}^\mu Z_\mu + h.c. \\
&= -i\frac{g_w}{2\sqrt{2}} (\bar{\nu}_L \gamma^\mu l_L) W_\mu - i\frac{g_w}{\sqrt{2}} \rho (\bar{\nu}_L \gamma^\mu \nu_L) Z_\mu + h.c.
\end{aligned}
\tag{1.3}$$

For a charged-current quasi-elastic⁴ neutrino-quark interaction, the invariant amplitude is then

$$\mathcal{M} = \frac{g_w^2}{8} \left[(\bar{l}_L(k') \gamma^\mu \nu_L(k)) \frac{g_{\mu\nu}}{M_W^2 - q^2} (\bar{q}_L(p') \gamma^\nu q_L(p)) \right] \quad (1.4)$$

In the low energy regime ($q^2 \ll M^2$), weak interactions can be approximated as being point-like, and the W and Z propagators can be simplified by

$$\frac{1}{M^2 - q^2} \rightarrow \frac{1}{M^2}$$

$$\mathcal{M} \rightarrow \frac{g_w^2 g_{\mu\nu}}{8M_W^2} [(\bar{l}_L(k') \gamma^\mu \nu_L(k)) (\bar{q}_L(p') \gamma^\nu q_L(p))] \quad (1.5)$$

In the Llewellyn-Smith[19] formulation used in the T2K Monte Carlo predictions (see Section 2.4.1), the full quasi-elastic differential cross-section for a neutrino on a nuclear target is given by

$$\frac{d\sigma}{dQ^2} = \frac{G_F^2 M^2}{8\pi E_\nu^2} \left[A + \frac{s-u}{M^2} B + \frac{(s-u)^2}{M^4} C \right] \quad (1.6)$$

where M is the nucleon mass, m is the lepton mass, G_F is the Fermi coupling constant, and the momentum transfer $s - u = 4ME_\nu - Q^2 - m^2$. The terms A, B , and C are functions of the form factors of the nucleon[20]. The form factor that is of the most interest for neutrino

⁴The term *quasi-elastic* refers to the fact that there are no truly elastic scatterings in the charged-current channel since $\nu_i \neq l_f$. However, in the case that the only products of the interaction are the outgoing lepton and the transformed nucleon, this process is the nearest analog.

scattering is the axial-vector form factor, F_A . It is generally assumed to be a dipole of the form

$$F_A(Q^2) = \frac{g_A}{(1 + Q^2/M_A^2)^2} \quad (1.7)$$

where $g_A = F_A(0) = 1.2694$ is found from experiment, and M_A is the axial mass. Early deuterium experiments indicated that $M_A \approx 1.0$ GeV, but modern neutrino scattering experiments on heavier targets frequently measure higher axial mass values, sometimes as high as $M_A = 1.35$ GeV[20]. This discrepancy is of particular concern, as the axial mass affects both the shape and the overall normalization of the quasi-elastic cross-section. It is the largest physics systematic error on this analysis (Section 4.1).

1.2.2 Neutrino Interaction Modes

Neutrino interactions are often more complicated than the simplified interactions described in Section 1.2.1. In the T2K energy region, there are four main scattering modes: *charged-current quasi-elastic scattering*, *neutral current elastic-scattering*, *resonance production*, and *deep inelastic scattering*.

The simplest scattering modes are charged-current quasi-elastic (CCQE) and neutral-current elastic (NCE) interactions. For CCQE interactions, a neutrino scatters off a neutron via the transfer of a W^+ , producing a muon and a proton. In neutral current elastic (NCE) scattering, the interaction is mediated by the neutral Z^0 , leaving both the neutrino and the nucleon (N) unchanged. CCQE and NCE are the dominate interaction modes in the energy regime of this analysis (see Figure 3).

$$\nu n \rightarrow \mu^- p \quad (\text{CCQE}) \quad (1.8)$$

$$\nu N \rightarrow \nu N \quad (\text{NQE}) \quad (1.9)$$

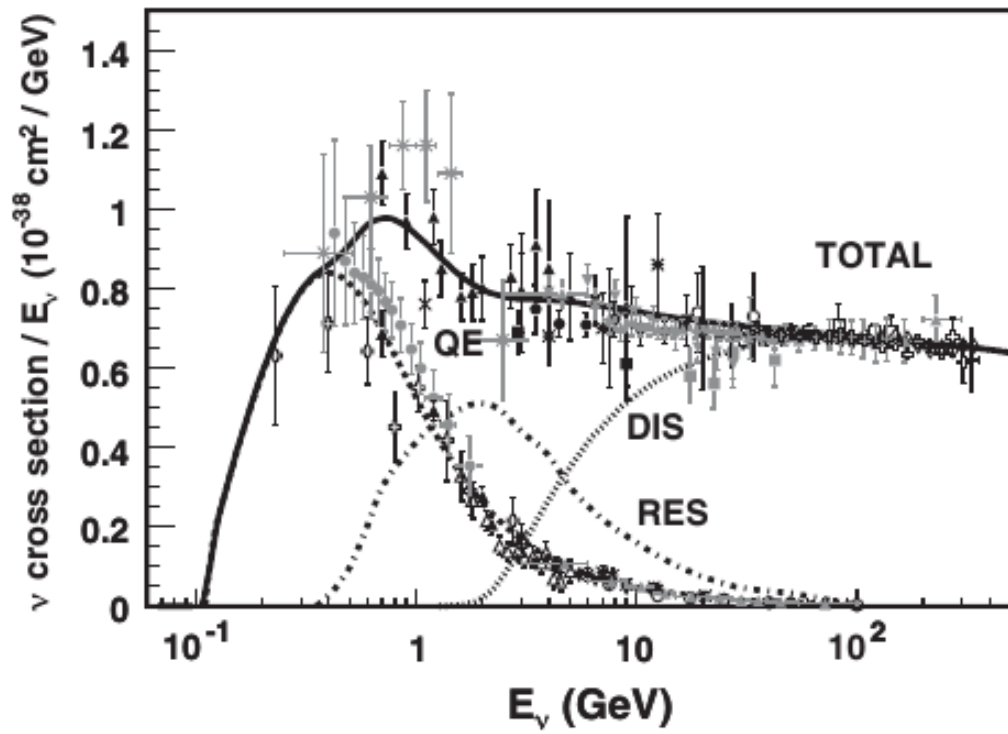


Figure 3: A compilation of measurements of the total ν_μ cross-section by E_ν , along with the contributions from each interaction mode. This plot is reprinted from [20], a global survey of the current status of neutrino experiments. A full listing of all data sources is also given.

At higher neutrino energies more complicated out-going states become possible. In particular, there are multiple avenues for pion production. Resonant interactions produce a baryon resonance that quickly decays, producing a nucleon and a single pion. These interactions can occur in both charged-current and neutral-current channels. In principle, more complicated resonant states can be produced, though single pion production is the most prevalent for T2K-relevant energies.

$$\nu N \rightarrow \mu^- N^* \rightarrow \mu^- \pi N' \quad (\text{CCRes}) \quad (1.10)$$

$$\nu N \rightarrow \nu N^* \rightarrow \nu \pi N' \quad (\text{NCRes}) \quad (1.11)$$

The incoming neutrino can also scatter coherently off the atomic nucleus (A) as a whole. These interactions are characterized by low momentum transfer, with very forward-going products. Both neutral-current and charged-current coherent interactions are possible.

$$\nu A \rightarrow \mu^- A \pi^+ \quad (\text{CC-Coherent}) \quad (1.12)$$

$$\nu A \rightarrow \nu A \pi^0 \quad (\text{NC-Coherent}) \quad (1.13)$$

At energies above ~ 1 GeV, the incoming neutrino can scatter off an individual quark inside the nucleon, producing a hadronic shower (X). This process is referred to as deep inelastic scattering (DIS), and it can occur in both the neutral-current and charged-current channels.

$$\nu N \rightarrow \mu^- X \quad (1.14)$$

$$\nu N \rightarrow \nu X \quad (1.15)$$

Table 1: A table of M_A values for neutrino scattering experiments on various nuclear targets.

[†]*A world average found from early deuterium experiments.*

Experiment	M_A (GeV)
Deuterium [†]	1.01 ± 0.01 [22]
MINOS (Fe)	1.23 ± 0.18 [23]
K2K (C)	1.14 ± 0.10 [24]
K2K (O)	1.20 ± 0.12 [25]
MiniBooNE (C)	1.35 ± 0.17 [21]

1.2.3 Current Charged-Current Quasi-Elastic Measurements

Early neutrino cross-section experiments were often performed in bubble chambers on free deuterium targets. These measurements were plagued by low statistics with large error bars on their results, though they generally found an axial mass value of $M_A \approx 1$ GeV[20].

Modern experiments use heavier targets that are bound together, complicating both the inter- and intra-nuclear effects on the cross-section. This affects the quasi-elastic cross-section in particular, and modern experiments typically report higher axial mass values, with MiniBooNe reporting a global high $M_A = 1.35 \pm 0.17$ GeV[21] (Table 1). The axial mass affects both the shape and normalization of the cross-section with a higher value leading to an increase in quasi-elastic events, and M_A is often used as a proxy for σ_{QE} .

A plot of total ν_μ quasi-elastic cross-sections from various experiments can be seen in Figure 4, along with the predicted cross-section from the NUANCE[26] generator with $M_A = 1.0$ GeV. An axial mass value close to unity works well for higher energy neutrino energies, but the excess in the lower-energy MiniBooNE data is clear. This plot highlights another issue, which is simply the relative lack of data points below ~ 1 GeV. Since the peak beam energy of T2K is ~ 0.6 GeV (Section 2.1) and the acceptance of this selection is for muons with momenta $\sim 200\text{MeV} - 600$ MeV (Section 3.2.9), this is precisely the region that this

analysis examines.

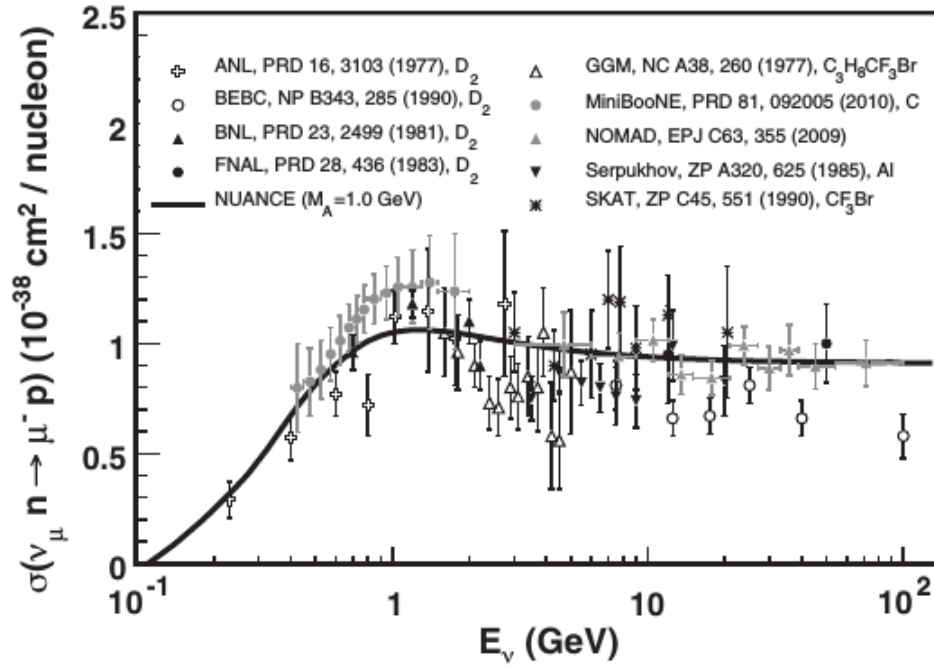


Figure 4: Existing measurements of the ν_μ quasielastic scattering cross-section as a function of neutrino energy. For more detail on how this plot was generated, see [20]

The MiniBooNE result is the first $4\text{-}\pi$ double-differential cross-section measurement of this interaction mode[21]. The peak beam energy for that experiment is ~ 788 MeV with a much broader spectrum than T2K, and the MiniBooNE target material is mineral oil (CH_2). The goal of this analysis is to present a similar measurement on water (H_2O). There is no directly comparable measurement for this result.

1.3 NEUTRINO OSCILLATIONS

The number of “active” neutrinos is well-constrained by measurements of Z^0 produced by electron/positron collisions at LEP and SLD[27]. By comparing the total width of the Z^0 with the sum of the partial widths from observable daughter products ($q\bar{q}$, $l^\pm l^\mp$), the

invisible partial width can be measured (the partial width to non-observable products). The ratio of this invisible partial width to the total width is strongly dependent on the number of neutrino species (Figure 5). These measurements do not place a constraint on the existence of “sterile” neutrinos, which are neutrinos that do not couple to any of the weak bosons (the existence of these sterile neutrinos is still an active area of research). The number of active neutrino flavors has been determined to be 2.9840 ± 0.0082 , in good agreement with the known generations of charged leptons.

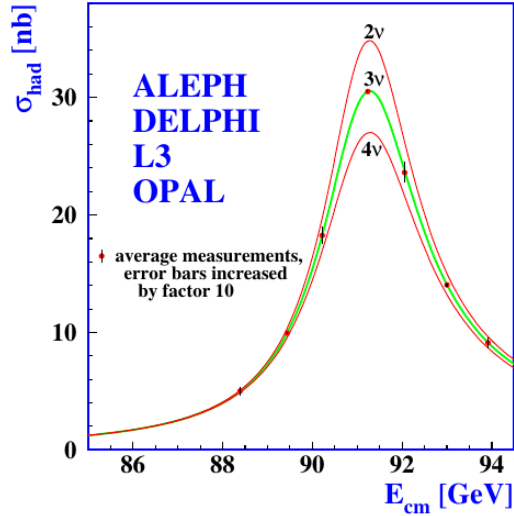


Figure 5: Measurement of the hadron production cross-section around the Z resonance, as compared to the prediction with 2, 3, and 4 active neutrino flavors^[27]

The relationship between the three neutrino flavors and the three mass states can be described as a linear transformation between two bases, governed by a 3×3 rotation matrix.

In general, an $N \times N$ unitary matrix has N^2 real parameters: $N(N - 1)/2$ mixing angles, and $N(N + 1)/2$ phases. In the case of three neutrino mass states, $\nu_{i,j,k}$, and three flavor states, $\nu_{e,\mu,\tau}$, this yields 3 distinct angles and 6 phases. Each state in both bases can be rephrased as $|\nu_\alpha\rangle \rightarrow e^{i\phi_\alpha} |\nu_\alpha\rangle$. Neutrino interactions are invariant under an overall $U(1)$ global phase translation. Five of the six phases, $e^{i\phi_\alpha}$, are independent from each other, while the sixth is constrained by this invariance and cannot be rotated away. Represented in this translated basis, there is only one physical phase in the mixing matrix.

The standard matrix parameterization for neutrino oscillations is the Pontecorvo-Maki-Nakagawa-Sakata (PMNS) matrix, named in reference to the theorists who developed the first models for neutrino mixing [8, 28] (shown in its most general form in Figure 6). The current global best-fits for each mixing angle and δ can be found in Appendix A.

$$U = \begin{pmatrix} c_{12}c_{13} & s_{12}c_{13} & s_{13}e^{-i\delta} \\ -s_{12}c_{23} - c_{12}s_{23}s_{13}e^{i\delta} & c_{12}c_{23} - s_{12}s_{23}s_{13}e^{i\delta} & s_{23}c_{13} \\ s_{12}s_{23} - c_{12}c_{23}s_{13}e^{i\delta} & -c_{12}s_{23} - s_{12}c_{23}s_{13}e^{i\delta} & c_{23}c_{13} \end{pmatrix}$$

Figure 6: The PMNS neutrino mixing matrix. The term c_{ij} (s_{ij}) stands for $\cos\theta_{ij}$ ($\sin\theta_{ij}$), where θ_{ij} is one of the three mixing angles, and δ is the CP-violating phase.

Each neutrino flavor state ($|\nu_\alpha\rangle$) can be written as a linear combination of the three mass states ($|\nu_k\rangle$)⁵:

$$|\nu_\alpha\rangle = \sum_{k=1,2,3} U_{\alpha k}^* |\nu_k\rangle \quad (\alpha = e, \mu, \tau) \quad (1.16)$$

where $U_{\alpha k}^*$ are terms in the PMNS mixing matrix. The mass states, $k = 1, 2, 3$, are eigenstates of the Hamiltonian with energy eigenvalues

$$E_k = \sqrt{p^2 + m_k^2} \quad (1.17)$$

and the time evolution of ν_k is given by the usual plane-wave description for a free particle

$$|\nu_k(t)\rangle = e^{-iE_k t} |\nu_k\rangle \quad (1.18)$$

The evolution of a particle which is originally in flavor state α at time $t = 0$ can be found

⁵This derivation of neutrino oscillation probabilities follows the approach taken in Giunti and Kim [29].

from Equations 1.16 and 1.18

$$|\nu_\alpha(t)\rangle = \sum_k U_{\alpha k}^* e^{-iE_k t} |\nu_k\rangle \quad (1.19)$$

Using the unitarity of the PMNS mixing matrix, ν_k can be described by a linear combination of the neutrino flavor states: $|\nu_k\rangle = \sum_\alpha U_{\alpha k} |\nu_\alpha\rangle$. Substituting back into Equation 1.3, we have

$$|\nu_\alpha\rangle = \sum_{\beta=e,\mu,\tau} \left(\sum_k U_{\alpha k}^* e^{-iE_k t} U_{\beta k} \right) |\nu_k\rangle \quad (1.20)$$

The amplitude for a particle ν_α to transition to ν_β after time t is then

$$A \equiv \langle \nu_\beta | \nu_\alpha(t) \rangle = \sum_k U_{\alpha k}^* U_{\beta k} e^{-iE_k t} \quad (1.21)$$

The transition probability is the square of the amplitude

$$P_{\alpha \rightarrow \beta(t)} = |A|^2 = \sum_{k,j} U_{\alpha k}^* U_{\beta k} U_{\alpha j} U_{\beta j}^* e^{-i(E_k - E_j)t} \quad (1.22)$$

Neutrino masses are $<O(1\text{eV})$ and the typical energy of a neutrino in an accelerator experiment is $\sim O(1\text{ GeV})$. Clearly, we can safely consider these to be ultra-relativistic. In this limit, Equation 1.17 can be approximated as

$$E_k \approx E + \frac{m_k^2}{2E} \quad (1.23)$$

where $E = |p|$. The energy-dependent component to the exponential in Equation. 1.21 can

then be rewritten as

$$E_k - E_j \approx \frac{\Delta m_{kj}^2}{2E} \quad (1.24)$$

where $\Delta m_{kj}^2 = m_k^2 - m_j^2$. Plugging Equation 1.24 into the transition probability, we find

$$P_{\alpha \rightarrow \beta(t)} = \sum_{k,j} U_{\alpha k}^* U_{\beta k} U_{\alpha j} U_{\beta j}^* e^{-i \frac{\Delta m_{kj}^2}{2E} t} \quad (1.25)$$

Neutrino time-of-flight measurements are an active area of research, and as of yet, no experiment has been able to distinguish neutrino velocities from c [30, 31]. This is not surprising, since neutrinos travel at approximately the speed of light at kinetic energies $\gtrsim 2$ eV, while typical oscillation experiments deal with neutrino energies ~ 1 MeV – 1 GeV⁶. Assuming that $v_\nu \approx c$, the time of flight is equivalent (in natural units) to the distance traveled ($t = L$), and Equation 1.25 can be written as

$$P_{\alpha \rightarrow \beta(t)} = \sum_{k,j} U_{\alpha k}^* U_{\beta k} U_{\alpha j} U_{\beta j}^* e^{-i \frac{\Delta m_{kj}^2 L}{2E}} \quad (1.26)$$

The oscillation probability depends only on elements of the mixing matrix, the energy of and distance traveled by the neutrino, and the difference in the squared masses of the mass states. The ν_μ survival ($\nu_\mu \rightarrow \nu_\mu$) and ν_e appearance ($\nu_\mu \rightarrow \nu_e$) probabilities used for T2K oscillation analyses are (to leading order)

⁶There is also an energy threshold in the lab frame for ν_μ and ν_τ charged current interactions of ~ 110 MeV and 3.5 GeV, respectively. It is clear that for the practical concern of determining the oscillation probabilities for a ν_μ experiment, setting $v_\nu = c$ is a reasonable assumption.

$$P_{\nu_\mu \rightarrow \nu_\mu} \simeq 1 - 4\cos^2(\theta_{13}) \sin^2(\theta_{23}) [1 - \cos^2(\theta_{13}) \sin^2(\theta_{23})] \times \sin^2\left(1.267 \frac{\Delta m^2 L}{E_\nu}\right) \quad (1.27)$$

$$P_{\nu_\mu \rightarrow \nu_e} \simeq \sin^2\theta_{23} \sin^2 2\theta_{13} \sin^2 \frac{\Delta m_{23}^2 L}{4E_\nu} \quad (1.28)$$

2.0 THE T2K EXPERIMENT

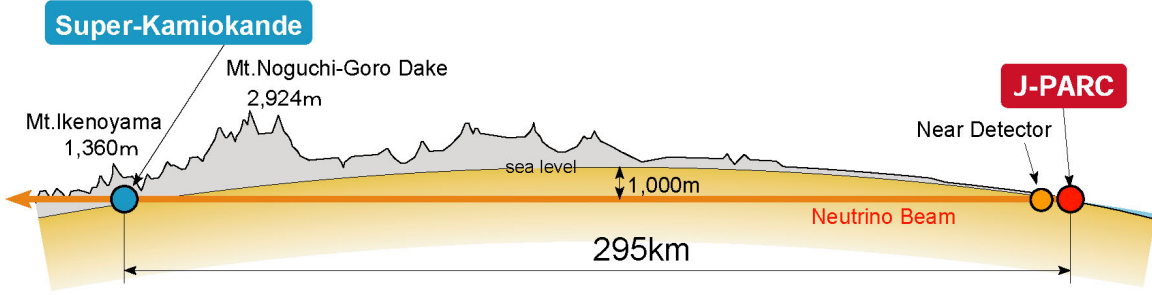


Figure 7: A schematic of the T2K experiment. A beam of ν_μ are generated at J-PARC, characterized at the ND280 detector suite, and then travel underneath the mainland of Japan to the Super-Kamiokande far-detector 295 km away.

The Tokai-to-Kamiokande (T2K) experiment is a long-baseline neutrino oscillation experiment which utilizes a ν_μ beam to study ν_μ oscillations and determine their mixing parameters. The primary physics goals of T2K are to observe a non-zero θ_{13} through ν_e appearance studies, and to achieve precision measurements of $\delta(\Delta m_{23}^2) \sim 10^{-4} eV^2$ and $\delta(\sin^2 2\theta_{23}) \sim 0.01$ through ν_μ disappearance studies.

A beam of ν_μ is generated at the Japan Proton Accelerator Research Center (J-PARC), located in Tokai on the eastern coast of Japan, and directed 2.5° off-axis from the detectors. T2K is the first experiment to use this off-axis method to generate a neutrino beam, which allows for a more monochromatic neutrino spectrum than would be possible otherwise (more details on this are in Section.2.1.3). The flux and composition of this beam are measured at a suite of near detectors located 280 m from the target (collectively referred to as ND280),

and then travel 295 km to the Super-Kamiokande (SuperK) water Cherenkov detector, 1 km beneath Mt. Ikeno in western Japan.

The accelerator complex and ND280 were completed in 2009, and data taking began in 2010. There are currently ~ 500 collaborators from 59 institutes and 11 countries active in T2K.

A summary of the accelerator, beam production, near detectors, and far detector will be provided in the following sections, as well as an explanation of various T2K-specific software. While it is necessary to give a complete overview of the T2K experiment, more detail will naturally be given to the components most pertinent to this thesis. More detailed information can be found at [32].

2.1 BEAM AND NEUTRINO PRODUCTION

The beam for T2K is produced by colliding accelerated protons into a graphite target, creating mesons which then decay into lepton/neutrino pairs. By steering the incoming protons and then focusing the resulting particles, the direction of the neutrino beam can be controlled. The beam is optimized for the production of neutrinos at the oscillation maximum, which at 295 km is ~ 600 MeV. In order to achieve this, T2K is the first neutrino oscillation experiment to use an off-axis design for its beam.

The off-axis design allows for a relatively monochromatic energy spectrum as compared to an on-axis beam. The reason for this can be easily seen by looking at the kinematics of the charged pion decay. From the conservation of four-momentum, $P_\pi^\lambda \rightarrow P_\mu^\lambda + P_\nu^\lambda$, we can derive a relationship between the energy of the pion produced at the target with the energy of the outgoing neutrino.

$$E_{\nu_\mu} = \frac{1}{2} \frac{m_\pi^2 - m_\mu^2}{E_\pi - \sqrt{E_\pi^2 - m_\pi^2} \cos\theta} \quad (2.1)$$

where θ is the angle between the pion and the out-going neutrino. Figure 8 shows this relationship for four different angles. For a given off-axis angle, there is a maximum possible E_ν regardless of the energy of the parent pion. Since the pions themselves have some spread around the direction of the original proton beam, neutrino energies > 1 GeV are seen in T2K, but the bulk of the spectrum is located around 600 MeV.

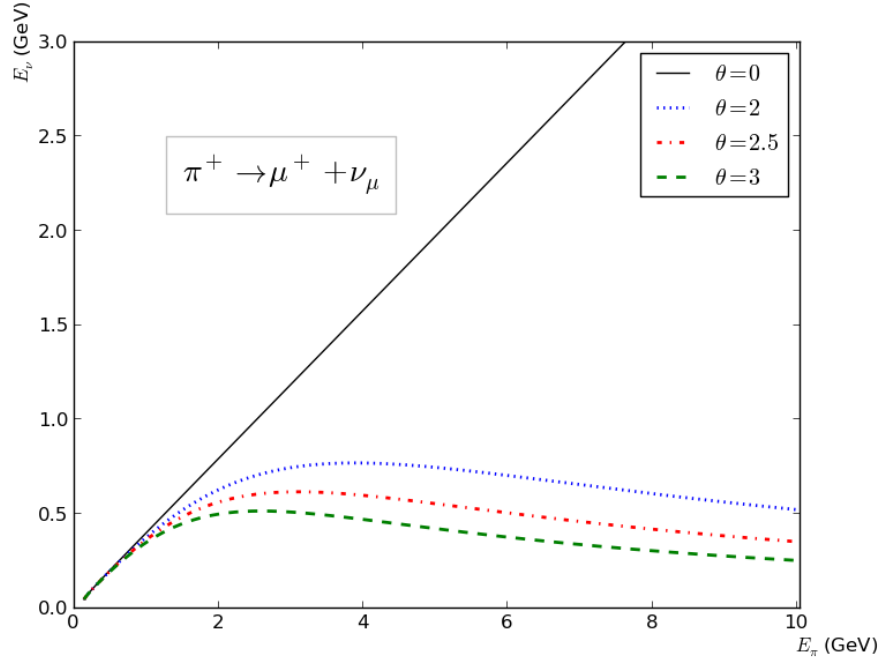


Figure 8: E_ν as a function of E_π for different angles between the original pion direction and the out-going neutrino direction.

In the following sections, an overview of the accelerator, beam production, and beam monitoring components of T2K is given. A more detailed description can be found in [33].

2.1.1 J-PARC

J-PARC is comprised of three separate accelerators[32]: a liner accelerator (LINAC), a rapid-cycling synchrotron (RCS) and the main ring (MR). The LINAC accelerates an H^- beam up to 400 MeV¹, which then traverses a charge-stripping foil, converting it to an H^+

¹This is the designed beam energy after all upgrades, which were completed in early 2014. At the time of commissioning, the beam energy was 181 MeV.

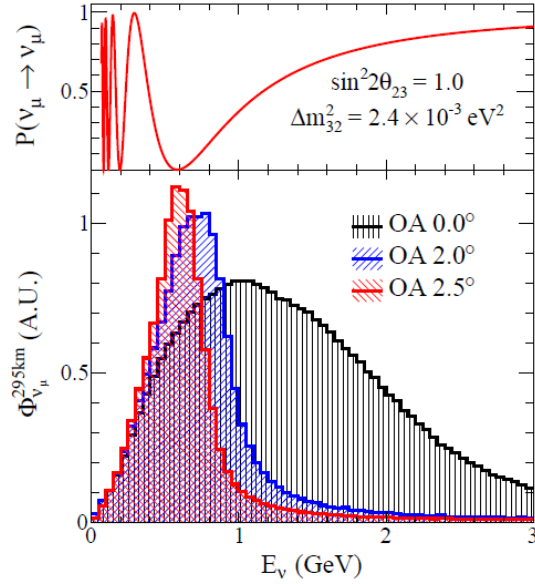


Figure 9: The muon neutrino survival probability and estimated flux for three different beam angles at SuperK[33].

beam, as it is injected into the RCS. The RCS accelerates the proton beam to 3 GeV. The majority of the beam is diverted here to the Material and Life Science Facility, and the rest is further accelerated to 30 GeV and injected into the MR. The beam circulates the MR in bunches of eight (six before June 2010), which are then passed to the T2K neutrino beamline by a set of kicker magnets.

2.1.2 T2K Neutrino Beamline

The neutrino beamline converts the beam spill (a set of eight proton bunches) into a physics-ready neutrino beam. It is composed of two sections: a primary beamline, which steers the beam in the desired direction, and a secondary beamline, which transforms the proton bunches into a focused neutrino beam. An overview of the beamline is shown in Figure 10.

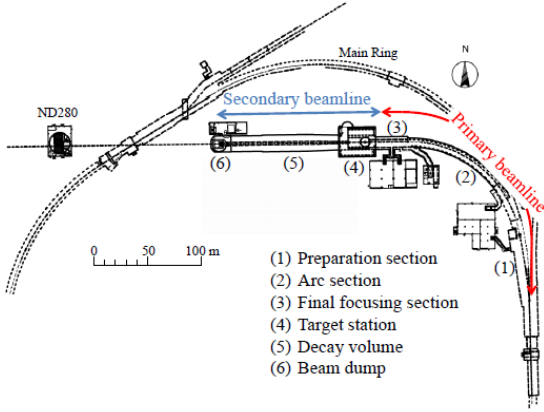


Figure 10: An overview of the T2K neutrino beamline

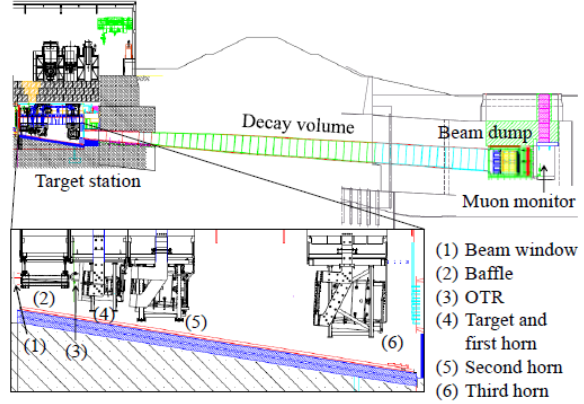


Figure 11: A side-section of the secondary beamline

2.1.2.1 Primary Beamline The primary beamline consists of three components: the preparation section, the arc section, and the final focusing section. The extracted proton beam first enters the preparation section, where the incoming beam is tuned with a series of 11 normal conducting magnets before entering the arc section. The arc section then uses an array of 14 super-conducting combined function magnets to direct the beam 80.7° towards the Super-Kamiokande far detector. The final focusing section uses a series of ten normal conducting magnets to focus the beam onto the target and to direct it a further 3.64° downwards with respect to the horizontal.

2.1.2.2 Secondary Beamline The secondary beamline, which consists of a target station, a decay “house”, and a beam dump (Figure 11), generates the neutrino beam. The interaction of the proton beam with the graphite target creates a beam of (primarily) charged pions and kaons, which are focused and then decay to form the desired ν_μ beam.

The target station itself consists of a baffle, an optical transition radiation (OTR) monitor, a graphite target, and three magnetic horns. The baffle is a collimator which protects the horns, and the OTR monitor samples the profile of the incoming beam immediately prior to the target.

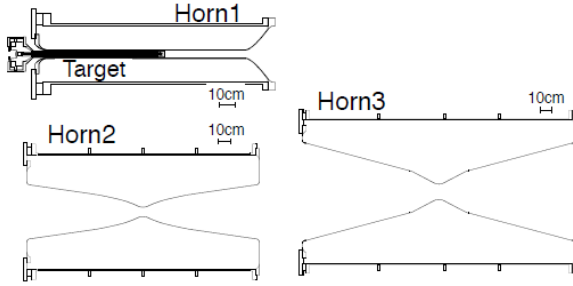
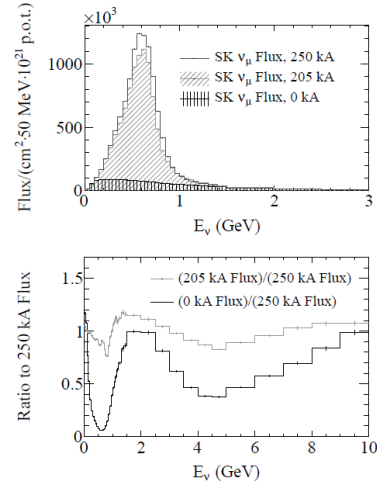


Figure 12: A cross-section of the three magnetic horns[33]. The target assembly is cantilevered in the upstream end of the first horn.



c

Figure 13: The predicted ν_μ flux at SuperK for different horn currents[33]. At the operating current of 250 kA, the flux increases by a factor of ~ 16 .

The target core is a graphite rod 2.6 cm in diameter and 91.4 cm long (1.9 interaction lengths). The core is surrounded by a 2 mm graphite tube, which is sealed in a 0.3 mm thick titanium case. Helium gas flows through the gaps between both the core and the tube, and between the tube and the case to cool the target. This assembly is cantilevered inside the first of the three magnetic horns (Figure 12).

Each of the horns is composed of two coaxial conductors which generate a toroidal field inside the enclosed volume, and a pulsed 250 kA current magnetizes the horn. The first horn collects the mesons produced in the target (predominately π^+ , with a small fraction of K^+), while the second and third horns focus the beam. The current to the horns can be reversed, in which case the horns now select out π^- , creating an $\bar{\nu}_\mu$ beam. When operating at 250 kA, the horns increase the ν_μ flux at SuperK by a factor of ~ 16 .

The focused mesons then travel through the decay house, a 96 m helium-filled steel tunnel. A beam dump constructed from graphite and lead is located at the downstream end of the decay volume, stopping all hadrons and any muons <5 GeV. Those muons that do

pass through are observed by the muon monitor. The muon monitor is an array of ionization chambers and silicon PIN photodiodes which measure the direction of these high energy muons (and, by proxy, the neutrino beam direction) and their intensity on a bunch by bunch basis. Immediately downstream of the muon monitor is an emulsion tracker which measures the absolute muon flux.

2.1.3 Neutrino Flux Prediction

Accurate prediction and modeling of the neutrino flux is crucial for an oscillation experiment. The beam simulation in T2K is a three step process (see Figure 14). First, the hadronic interactions of the primary proton beam with the target station are simulated, and the daughter products are propagated through the target. These particles are then passed to a model of the focusing horns and decay volume, where they are propagated until they interact or decay. By saving the kinematic information from the full interaction chain, the beam profile and hadronic interaction simulations can be updated. This is accomplished by reweighting the beam simulation to match data from measurements from the beam monitors, the horn magnetic fields, and data from the NA61/SHINE[34] experiment at CERN.

2.2 NEAR DETECTORS

The unoscillated beam flux and composition are characterized by measuring the neutrino energy spectrum and interaction rates at the near detector complex located 280 m from the neutrino beam target. The complex is housed in a pit 37 m deep with a diameter of 17.5 m, newly constructed for T2K, and is composed of the on-axis Interactive Neutrino Grid (INGRID) and an off-axis magnetized tracking detector (ND280; see Figure 15). The off-axis detector itself consists of several sub-detectors (Figure 16). The two primary components are the Pi-zero Detector (P \emptyset D), optimized to measure neutral current π^0 production on water, and the Tracker, designed for high-resolution momentum measurements and particle

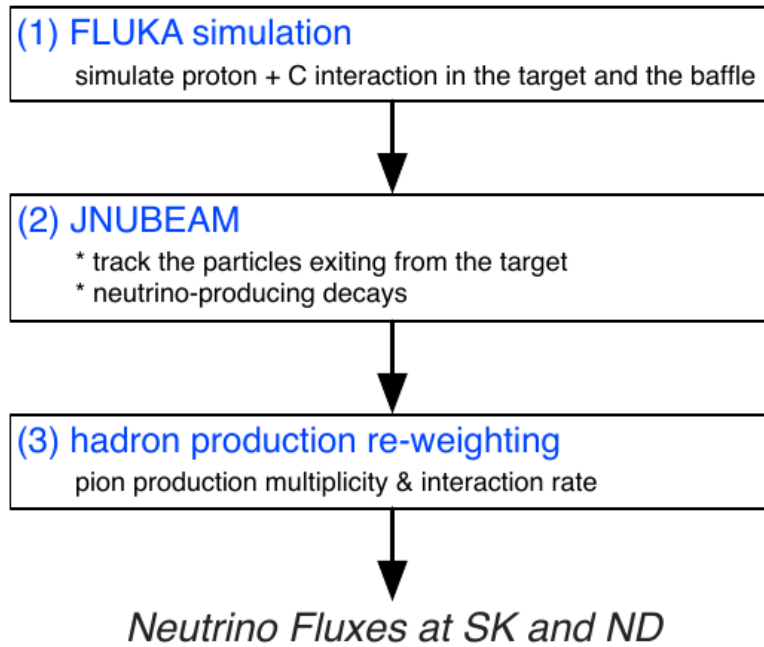


Figure 14: The flux prediction flow diagram[33]

identification. These are surrounded on all sides by electromagnetic calorimeters (ECals), and housed inside the repurposed UA1 magnet. The yokes of the magnet are instrumented to construct the side-muon range detector (SMRD), which serves the dual purpose of detecting muons exiting the detector as well as external backgrounds entering it.

2.2.1 INGRID

The INGRID on-axis detector is designed to monitor the beam direction and intensity directly and with sufficient statistics to provide daily measurements of the neutrino beam at the near detector site. The detector is composed of 14 identical modules arranged in a horizontal and vertical array, each approximately 10 m long and crossed at the beam center (Figure 17). Two additional modules are located just above the horizontal array and to either side of the vertical one to measure the axial asymmetry of the beam. The detector

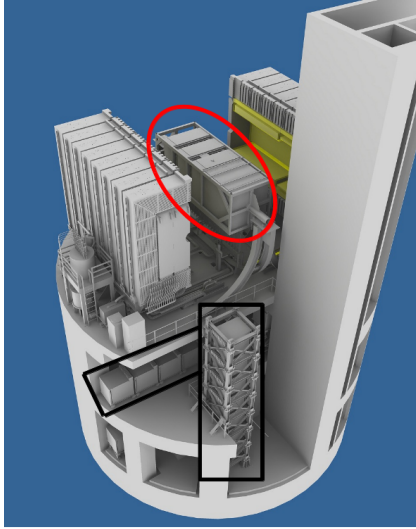


Figure 15: The ND280 complex. The off-axis detector with magnet open is on the upper level (circled in red), with the horizontal and vertical INGRID modules below (outlined in black).

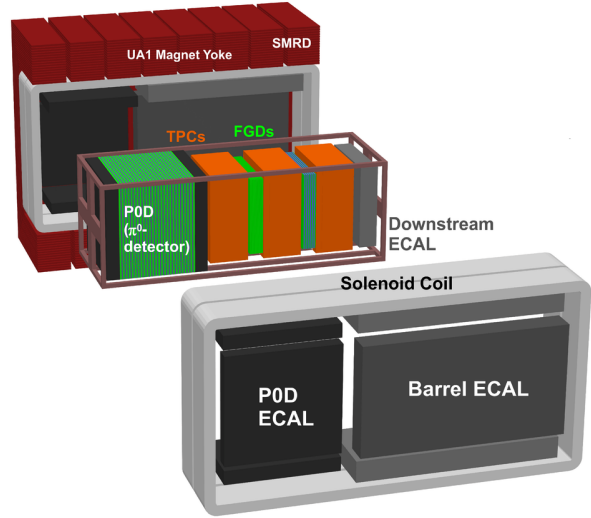


Figure 16: An exploded view of the off-axis detector. During operation, the magnet is closed, entirely surrounding the “basket” containing the P0D, the tracker, and ECALs. The beam direction is from left to right.

was installed with a positional accuracy of 2 mm in the plane perpendicular to the neutrino beam. The beam center is measured by INGRID to a precision of 10 cm (corresponding to 0.4 mrad at ND280), which is better than the required 1 mrad precision.

Each module consists of a sandwich structure of 9 iron target plates and 11 scintillator planes, surrounded by veto scintillator planes (Figure 18). The dimensions of the iron planes are $124 \times 124 \text{ cm}^2$ in the plane perpendicular to the beam and 6.5 cm along the beam, with a total mass of 7.1 t. Each tracking plane consists of 9 layers of 11 horizontal and 11 vertical scintillator bars, with a total of 9592 channels. More information on the INGRID detector can be found in [35].

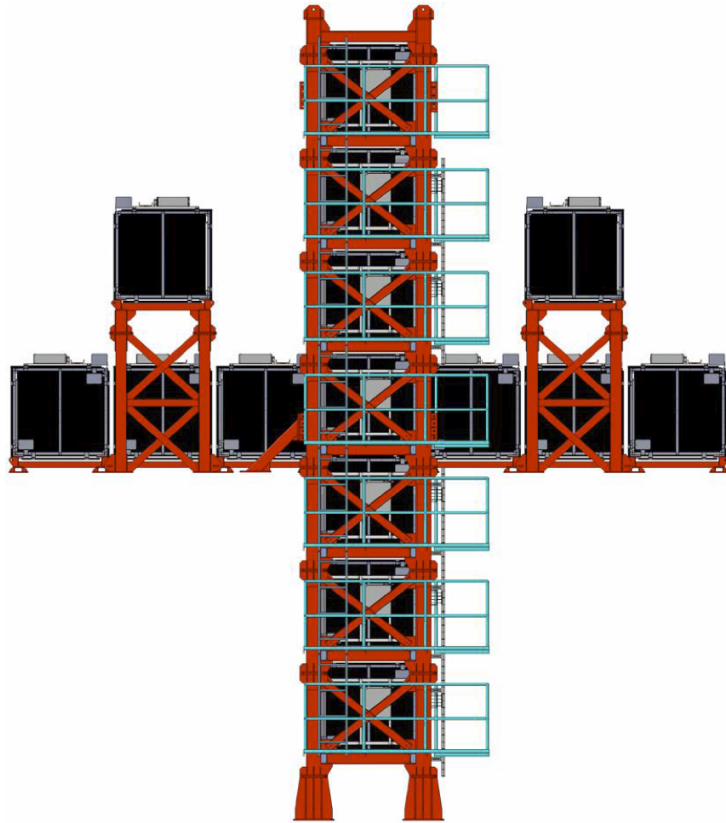


Figure 17: The INGRID detector, from the perspective of the incoming beam. The detector is centered at the beam axis, with two arrays of 7 modules spanning ± 5 m from the beam center. Two additional modules measure the asymmetry of the beam.

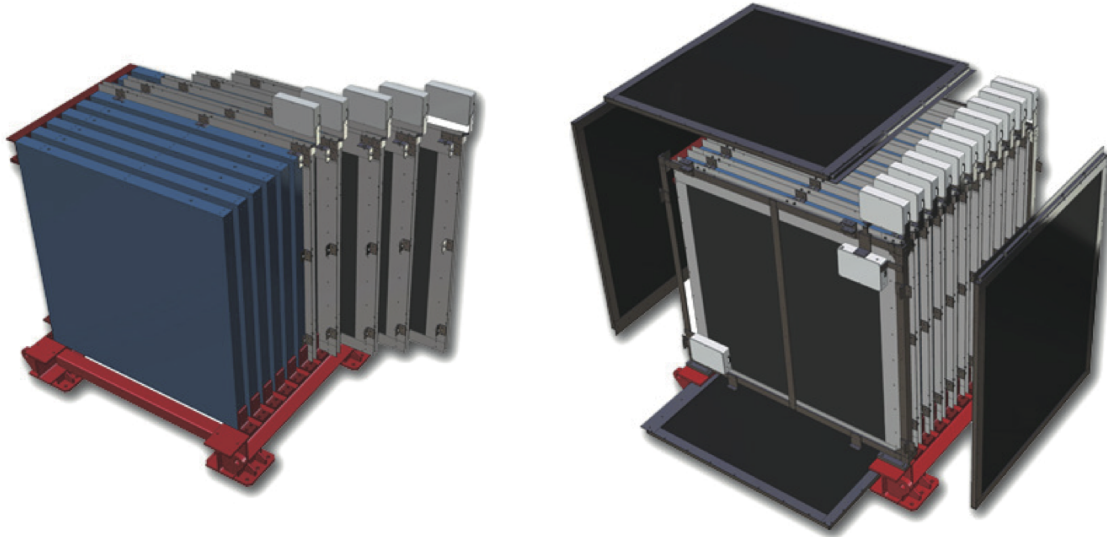


Figure 18: An exploded view of an INGRID module. The figure on the left shows the lead plates (in blue) sandwiched between layers of scintillator. On the right are the surrounding veto planes in black.

2.2.2 The P \emptyset D

The primary physics goal of the P \emptyset D is to constrain backgrounds at SuperK by measuring the neutral current π^0 production rate on water. The P \emptyset D must therefore contain a substantial water mass while also being capable of accurately reconstructing and identifying π^0 s. To achieve this, the P \emptyset D was designed with alternating layers of active scintillator and water target bags. Data can be taken with these bags either filled or drained, and neutrino cross-sections on water can be determined by comparing the interaction rates between these configurations. This analysis uses this feature to measure the ν_μ CC- 0π cross-section on water in the P \emptyset D.

The main building block of the P \emptyset D is a P \emptyset Dule[36], which provides both an active tracking region and structural support. Each P \emptyset Dule consists of scintillator bars in two perpendicular arrays, the more upstream one oriented vertically (134 bars) and the other horizontally (126 bars). The scintillators are triangular in shape, with a base of 33 mm and a height of 17 mm, and the horizontal (vertical) bars are 2340 mm (2200 mm) long. Each bar

has a 2.6 mm hole to allow for a 1 mm wave-length shifting (WLS) fiber running the length of the bar. The fibers are mirrored on one end, and connected to an MPPC on the other (more on the PØD electronics below). There are 260 bars in each PØDule and 40 PØDules in total, giving 10,400 active channels in the PØD.

There are four “Super-PØDules” formed from the combination of individual PØDules (Figure 19). Two ECal Super-PØDules (the upstream and central ECals) are each constructed from alternating seven PØDules with seven layers of stainless steel covered lead sheets. There are two water target Super-PØDules, the upstream and central water targets². The upstream (central) water target Super-PØDule consists of alternating 13 PØDules with 13 (12) water bag layers and 13 (12) brass sheets. Each water bag layer has two water bags with a vertical high-density polyethylene center strut to minimize deformation of the water bags and adjacent scintillator. The mass of the detector with and without water is 16.1 t and 13.3 t, respectively.

Each water bag has two thin PVC pipes mounted inside with four independent water sensors: two depth sensors that provide mm level depth readings, and two off-set binary wet/dry sensors for backup and calibration purposes. These sensors are used to ensure that the full fiducial volume of the PØD is filled and that the bags are not leaking. Each water bag layer is sealed, so in the event of a leak, water drains out of the PØD without seeping into the adjacent layers.

The PØD Electronics Each scintillator bar has a coaxial hole with a WLS fiber running through it that is read out by a multi-pixel photon counter (MPPC). The MPPCs have 667 pixels which independently generate a Geiger avalanche when a photoelectron (pe) is detected. The signal from the readout is then the sum of the number of pixels fired, and does not depend on the amplitudes of the current produced at each pixel, with strong resolution of individual photons up to 7 pe (Figure 20).

The MPPCs are read out to Trip-t front-end boards (TFBs) originally developed at

²A note on nomenclature. There is another water target and another ECal located in the tracker, so while the central ECAL and water target are at the most downstream end of the PØD, they are central in the context of ND280 as a whole.

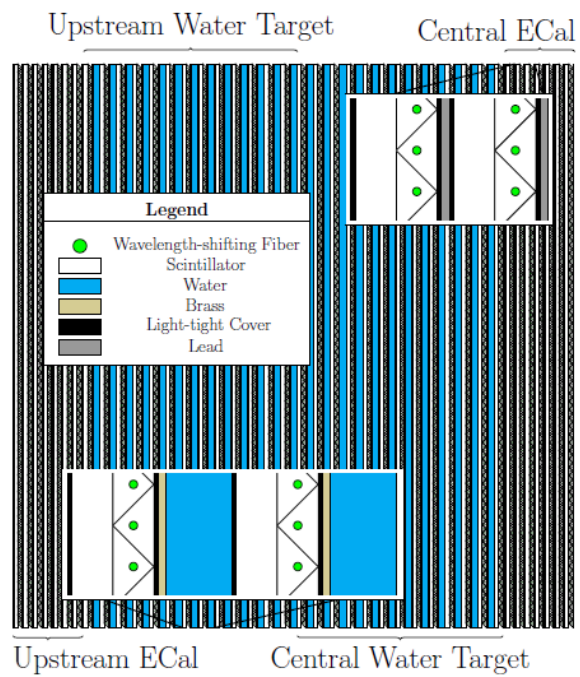


Figure 19: A layer-by-layer schematic of the P0D. The beam direction is from left to right.

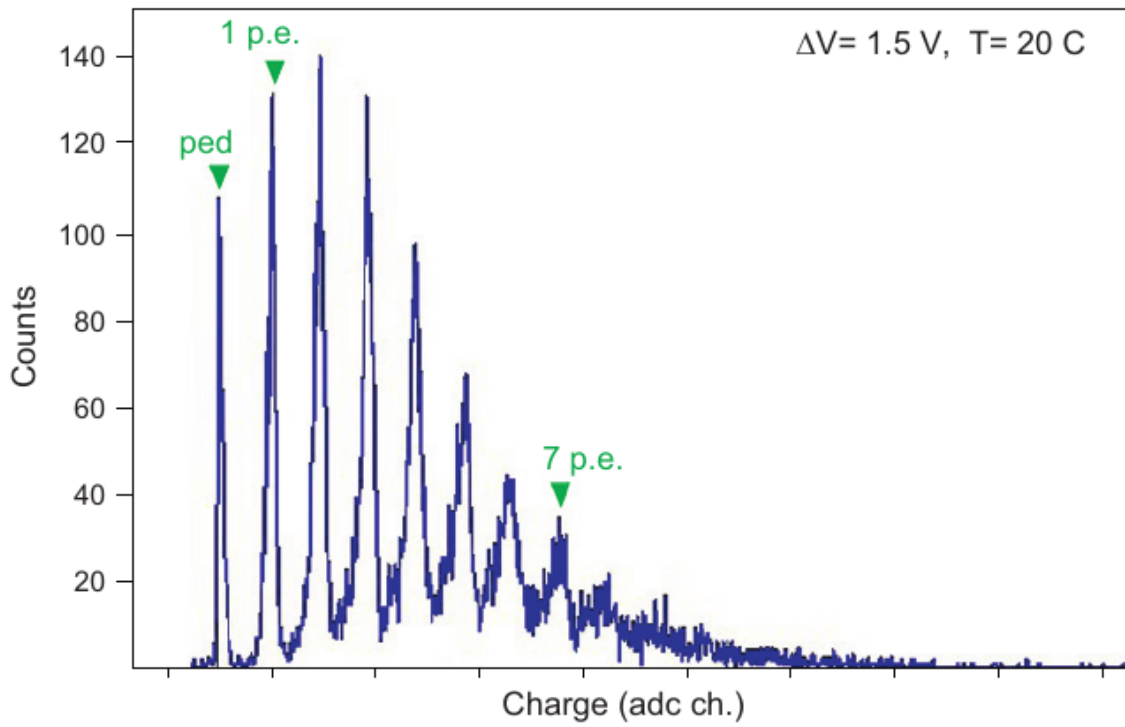


Figure 20: The response spectrum of a MPPC from an LED source. The first peak corresponds to the noise pedestal. Individual photon peaks can be seen until ~ 7 pe^[37].

Fermilab for the D \emptyset experiment. Each TFB can accept up to 64 MPPCs, and there are 174 TFBs in total: 29 for each ECal Super-P \emptyset Dule and 58 for each water target Super-P \emptyset Dule. The Trip-t chips integrate charge in 23 consecutive integration cycles, synchronized to the accelerator so that each beam bunch (~ 580 ns apart) is in a separate cycle. The length of integration cycle and reset period are programmed to 480 ns and 100 ns, respectively. While this allows for full coverage of any neutrino interactions within a spill, there is some dead-time for out-of-spill events, such as Michel electrons from muon decays.

2.2.3 The Tracker

Immediately downstream of the P \emptyset D is the tracker, which consists of two fine-grained detectors (FGDs) sandwiched between three time-projection chambers (TPCs). The primary design goal of the tracker is to achieve high-resolution detection and measurement of charged current interactions in ND280.

Each TPC consists of an inner box filled with an argon-based drift gas and an outer box of insulating CO₂. The panels of the inner box were machined to form a copper strip pattern that produces (in conjunction with a central cathode panel) a uniform electric field in the active volume of the TPC (Figure 21). Charged particles passing through the detector produce ionization electrons in the argon, which then drift to micromega readout planes. The drift time is used to reconstruct the third spatial dimension of particles in the TPCs.

The FGDs are composed of layers of scintillator bars, 9.16 mm on each side and 1864.3 mm long, oriented in the vertical and horizontal directions perpendicular to the beam. The first FGD consists of 30 layers of 192 bars each in alternating x and y directions. The second FGD has seven XY modules (one set of alternating x and y layers of scintillator bars) alternating with six layers of water. The detectors have identical geometries, apart from the water layers in the second FGD, allowing on-water neutrino cross-section measurements to be performed by comparing interaction rates between the two.

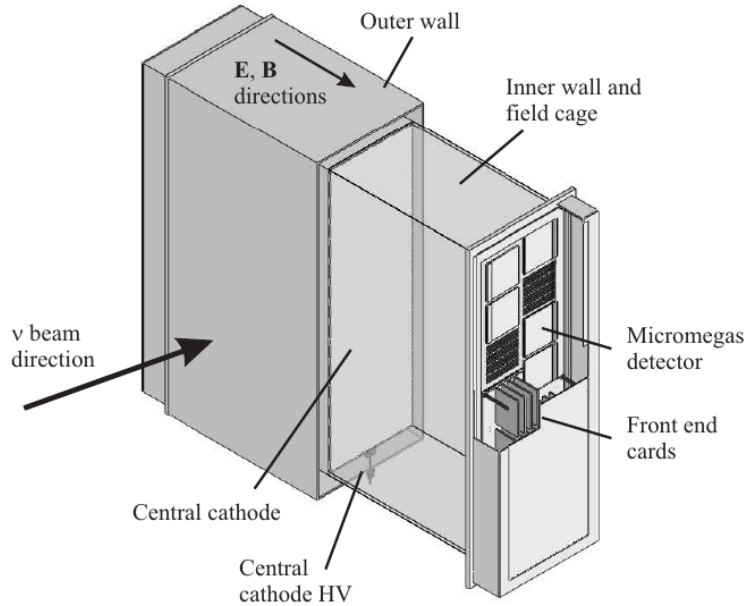


Figure 21: A diagram of a TPC. Note that the direction of the TPC's electric field is oriented the same as the near detector magnetic field to minimize the effect of the Lorentz force on the drifting electrons.

2.2.4 The Electromagnetic Calorimeters

The ND280 ECals are 13 independent modules that surround the P \emptyset D and tracker, designed to aide event reconstruction by detecting and measuring the energy and direction of photons which exited the inner detectors. Six modules surround the tracker (the Barrel ECals) and six surround the P \emptyset D (the P \emptyset DECals), while the remaining module is located at the downstream end of the tracker (the Downstream ECal). Each module is constructed of layers of scintillator bars glued to sheets of lead. All ECal modules can provide 3D reconstruction, except for the P \emptyset DECals, which can only measure position in the directions perpendicular to the beam. The ECals use the same MPPCs and electronics described in Section 2.2.2.

2.2.5 The Side Muon Range Detector

The SMRD was constructed by placing scintillator modules in the air gaps between the UA1 flux return yokes (8 pairs in total), and has a total of 4,016 channels. The five most upstream yokes contain 3 layers of instrumentation, yoke 6 has 4 layers, and yokes 7 and 8 have 6 layers. The SMRD uses the same MPPCs and electronics described in Section 2.2.2.

2.3 SUPER KAMIOKANDE

The far detector for T2K is the well-known Super Kamiokande water Cherenkov detector[38]. SuperK is a cylindrical structure filled with 50 ktons of purified water. The interior geometry is divided into two optically isolated regions divided by a stainless steel scaffold 50 cm thick. The outer detector (OD) is a cylinder ~ 2 m radially inward from the walls of SuperK, instrumented with 1,885 outward-facing photomultiplier tubes (PMTs). While unable to provide detailed event reconstruction, the OD can provide a veto on incoming backgrounds with nearly 100% efficiency.

The inner detector (ID) is instrumented with 11,129 PMTs, which provide $\sim 40\%$ surface coverage of the interior walls. When a charged particle above a certain energy threshold is produced inside the ID, Cherenkov radiation is emitted in a cone in the direction of the particle's motion. This cone of photons can be used to reconstruct information such as the event vertex and the particle's momentum. Particle identification can also be made by analyzing the ring produced by the Cherenkov radiation. Electrons scatter easily in the detector, and frequently produce electromagnetic showers, leading to a “fuzzy” ring pattern on the walls of the ID. Muons, on the other hand, are comparatively heavy, and are less prone to deviations in their trajectory. This leads to a much sharper and well defined ring of photons (see Figure 23 for examples of each). SuperK has been running since 1996, and the behavior of the detector is very well understood, with detector systematics on the 1% level.

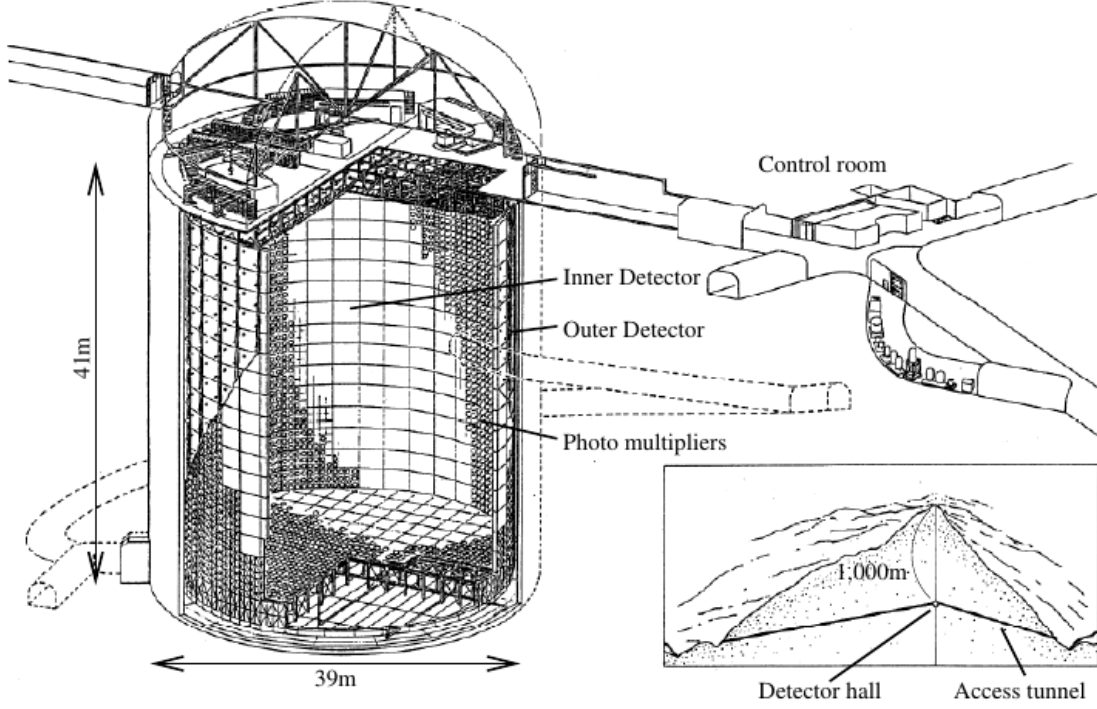
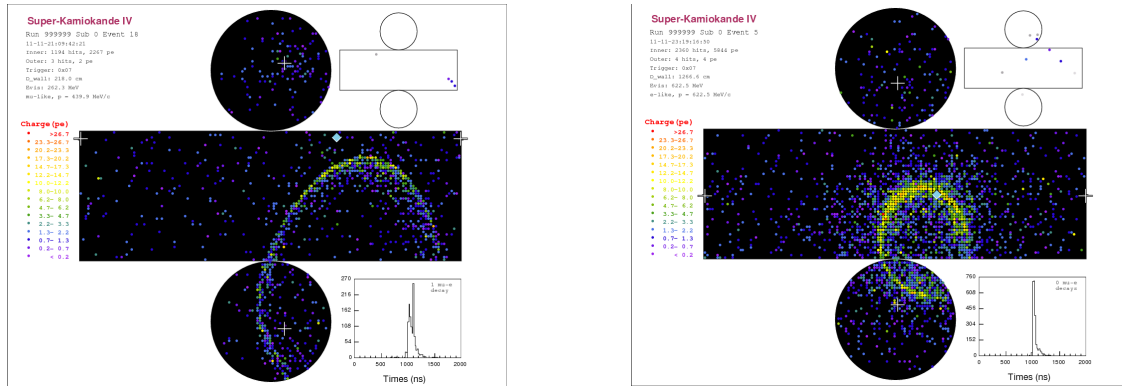


Figure 22: A diagram of SuperK. The inner and outer detectors are separated by a stainless steel scaffold, and the entire volume is filled with purified water[38].



(a) A muon produced from a CC ν_μ event

(b) An electron produced from a CC ν_e event

Figure 23: Two examples of single-ring events at SuperK. The muon (left) produces a much sharper and well-defined ring than the electron (right). These events were selected from T2K beam Monte Carlo[32]

2.4 T2K SOFTWARE

T2K utilizes a variety of different software packages, some well established throughout the particle physics community (such as ROOT, which forms the basic framework for data collection and analysis in T2K[39]), others developed internally. These packages can be roughly organized into three categories: data collection, reconstruction, and analysis. A full overview of the T2K software structure can be found in [32], but the pertinent components will be briefly described in the following sections.

2.4.1 Data Collection

When the experiment is running and actively taking data, there is very little software dependence in the actual collection process. Due to the low-statistics nature of neutrino research, there is no trigger for when data is retrieved from ND280 other than the timing of the beam. The signal from the active regions of the detector are read out and recorded in full for each bunch in every spill. If a particular subdetector is not operating at full capacity, a flag is attached to that run period, but the output from the detector is still recorded. The raw output is saved at KEK³, which allows for the full dataset to be reprocessed when the reconstruction software is updated.

Quite a lot of programming is necessary to compare this real-world information to existing models. Creating a simulation of T2K requires a full representation of the detector, as well as a means to generate the physics events themselves.

The ND280 detector geometry is modeled using GEANT4[40], which also simulates the energy deposits from particles passing through the detector. The response of the active regions of the detector (such as scintillator bars and electronics) is simulated in elecSim, a custom software package

³KEK refers both to the High Energy Accelerator Research Organization, which oversees high-energy particle physics research nation-wide, as well the National Laboratory for High Energy Physics located in Tsukuba, Japan. Further information on both can be found at <https://www.kek.jp/en/>.

T2K uses two separate Monte Carlo (MC) event generators to model neutrino interactions: NEUT and GENIE. The beam group provides neutrino flux estimates from beam MC, which is then combined with the detector geometries described above. This information is passed to the generators, which use relevant neutrino cross sections to generate interactions appropriate to the materials and energies present.

NEUT was initially developed to study atmospheric neutrino interactions and nucleon decay in Kamiokande[41], but has since been expanded and updated for use in experiments such as SuperK, K2K, SciBoone, and T2K. Since it has been primarily developed for use in water Cherenkov detectors, NEUT is the de facto event generator for T2K oscillation analyses.

For each event, NEUT generates a primary neutrino-nucleon interaction which produces a number of particles, which then undergo secondary interactions as they exit the nucleus. These secondary interactions are modeled using a particle cascade routine. A particle is propagated through the nucleus in steps of a predetermined unit length. After each step, NEUT determines whether or not the particle has re-interacted based on the interaction probability. If it has, a cascade is started for the new particle. This process is repeated until all product particles have exited the nucleus.

For charged-current quasi elastic events (those most relevant for this thesis), NEUT uses the Llewellyn-Smith[19] model for neutrino nucleon interactions. The momentum distribution of nucleons in the target nuclei are calculated using a nucleon spectral function model by Benhar and Fabrocini[42]. All interactions occur between a neutrino and a single nucleon.

NEUT also incorporates *meson exchange currents*⁴ (MEC) into the interaction models. Nucleon-nucleon correlations are modeled by the exchange of pions, and neutrinos are allowed to interact with these mesons as well as with individual nucleons. These short-range nucleon-nucleon effects are of particular concern to quasi-elastic measurements, as the detectable by-products are often indistinguishable from a CCQE event[43].

⁴This interaction mode is often referred to as 2p2h: 2 protons - 2 'holes', where the 'holes' are those left in the nucleus from the ejected protons. This is to emphasize that MEC is an extension on the 1p1h mode, which is the conventional CCQE interaction.

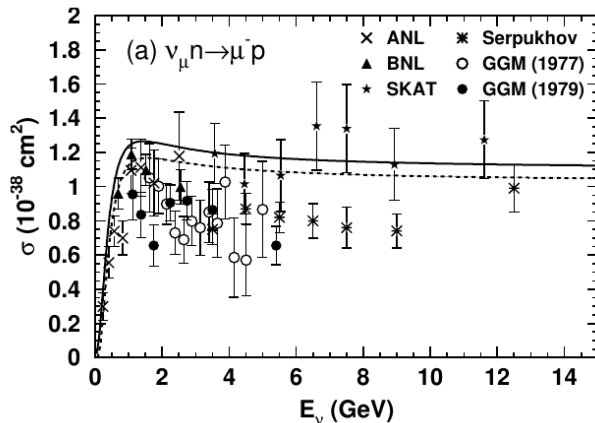


Figure 24: A comparison of cross-sections for CCQE scattering. The solid line is the NEUT calculated cross-section for free nucleons; the dashed line is that for protons in oxygen[41]. The T2K peak beam energy is $E_\nu \approx 0.6$ GeV

GENIE was created with the goal of establishing a “canonical” neutrino generator[44], covering all nuclear targets and all neutrino flavors with energies ranging from the MeV to PeV scales.

GENIE uses a relativistic Fermi gas (RFG) model to simulate the nuclear targets. Unlike NEUT, this model incorporates nucleon-nucleon correlations[45]. There are also substantial differences in the implementation of the cascade propagation of product particles. The interaction probability of hadrons is significantly reduced immediately after they are produced. The reason for this is that the quarks need time to fully coalesce as a hadron. To implement this, the first step in the cascade is a “free step” in which the re-interaction probability is set to zero. GENIE also uses the Llewellyn-Smith model of CCQE interactions.

2.4.2 Reconstruction

Each subdetector has its own stand-alone reconstruction software package, which convert the physical input from the detectors into analyzable information. While the output is designed to feed into a single, unifying reconstruction package (globalRecon, or more simply,

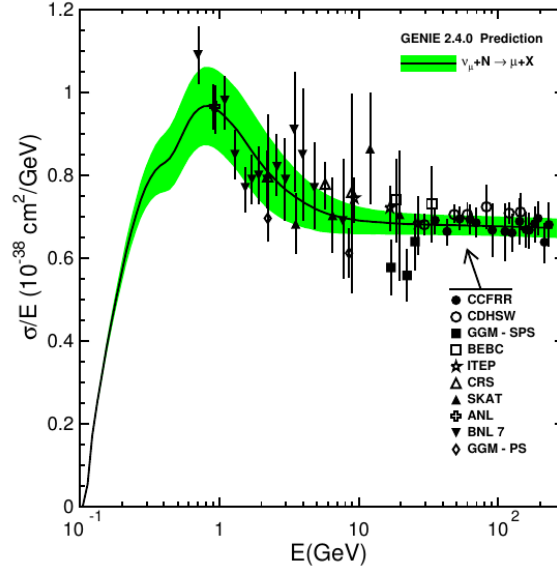


Figure 25: A comparison of cross-sections for CCQE scattering. The solid line is the default GENIE cross-section on an isoscalar target[44].

global), these packages are fully complete, and their results are physics-ready without being passed on to global. This analysis uses only the results of the P \emptyset D reconstruction and globalRecon objects that depend on that output. The relevant components of the ND280 reconstruction are described in the following section.

2.4.2.1 P \emptyset D Reconstruction The P \emptyset D Reconstruction software (p \emptyset dRecon) converts the photoelectrons collected by the MPPCs into a collection of final particles. There are four separate stages: hit preparation, track reconstruction, shower reconstruction, and Michel electron tagging (see Figure 26). The track and shower reconstructions are separate algorithms performed sequentially, with the track path first. Anything that does not pass the tracking reconstruction, or is determined to be electron-like ('EM') is sent the shower reconstruction. Because of this, the shower reconstruction is not relevant to this analysis.

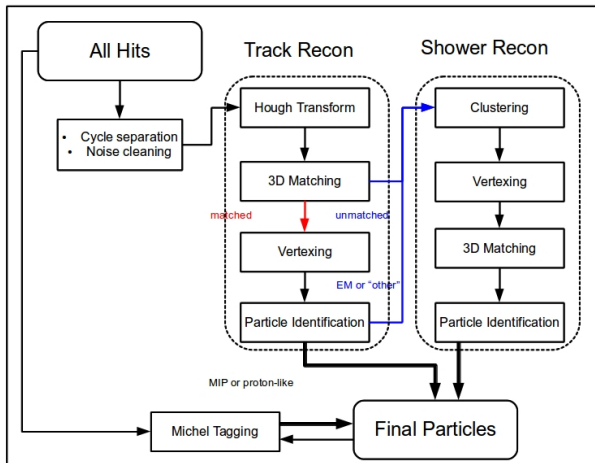


Figure 26: A flow diagram of the P \emptyset D reconstruction software. All clean hits are passed through the track reconstruction, with any objects that fail the 3D matching or are identified as non-MIP are sent through the shower reconstruction.

2.4.2.2 Hit Preparation The input into p \emptyset dRecon is a collection of hits, which can come from either: calibrated data hits with a good time stamp, or from elecSim (see Section 2.4.1). For a hit to have a valid time stamp, it must meet a certain charge threshold imposed by the readout hardware (~ 25 ADC). The time stamps are then used to sort the hits into the 23 cycles defined by the TFBs.

Once the hits have been divided into their cycles, they are passed to a noise cleaning algorithm. Noise hits are spurious signals sent from the readout electronics that are uncorrelated to the signal from the neutrino interactions in the detector. To minimize the effect of these, a hit must pass one of three criteria in order to be saved.

- It has charge $Q > 15$ pe
- It has charge $Q > 7$ pe with a neighbor in the same view (XZ or YZ plane) within 30 ns and 10 cm
- It has a neighbor within 30 ns and 3.5 mm

Hits failing each of these criteria are not used further in the reconstruction. Only cycles

with five or more 'clean' hits are passed to the tracking reconstruction.

2.4.2.3 Tracking Reconstruction The first step of the tracking reconstruction is to use the cleaned hits to produce any number of 2D tracks in both the xz and yz views. This is achieved by utilizing a Hough transform to create a track 'seed,' and then a road following algorithm to connect all matching hits.

A Hough transform is a technique to identify the line connecting multiple points. A number of straight lines with varying slopes are constructed through each hit individually, and then the perpendicular distance from those lines to the (arbitrary) origin is calculated. Each line can then be characterized by two numbers (i.e. a point): the distance to the origin, and the angle created by the perpendicular line with the origin. A curve is then generated for each hit. For hits in a straight line, there is a point of intersection for the curves created by the Hough transform, and this point characterizes the line through them. For the $P\emptyset D$ reconstruction, a minimum of four hits must be matched in this way.

This 'seed' is then extended layer-by-layer using a road following algorithm. At each layer upstream or downstream, this algorithm adds hits within 60 mm of the track seed with angular tolerance of 1.5 radians. This is continued in either direction until no additional hits can be added.

Once this is completed, the 2D tracks from each view are matched with each 2D track in the other. The intent is to create every possible pairing of tracks and then determine the best possible pairings. This helps to resolve tracks which are overlapping in one view but distinct in another. Any objects that do not have a successful 3D match are sent to the shower reconstruction. Matched 3D tracks have a Kalman filter applied, which starts at the most downstream end of the track, progresses to the most upstream end, and then back down. When this fit is complete, each scintillation layer is assigned a 'node,' which stores the position, time, charge, and direction information for all the hits in that layer. All tracks are defined as moving downstream by default in $p\emptyset d$ Recon. Identifying tracks traveling upstream must be done at the analysis level (more details on this process will be

given in Section 3.2.7).

The full set of all 2D and 3D tracks are then passed to the vertexing algorithm. This process projects all of the tracks back to a point of closest approach, with a positional variance that depends on the positional and directional uncertainty of the tracks. The potential vertices are rejected if the tracks are inconsistent in time (> 40 ns apart), or if the uncertainty in the x , y , or z position is > 50 cm. The candidate vertices are then paired with each other, so long as they are within 40 ns of each other and no more than 20 cm apart. The best matching pair is then clustered together and reintroduced as a single vertex, and this process is repeated until no more track combinations are possible.

Each 3D track undergoes a particle identification (PID). P0DRecon uses a likelihood based PID which uses several parameters: the charge asymmetry between adjacent layers, the charge asymmetry between adjacent P0Dules, the number of layers with no hits, and the fraction of charge in the last 5 layers of the track. No variables that depend on the overall energy scale are used to avoid charge differences between data and MC. There are four possible IDs: a light track (muon/pion-like), a heavy track (proton-like), EM-like (electrons and photons), and other. Light and heavy tracks are passed to the final particle container; EM and other tracks are passed to the shower reconstruction.

2.4.2.4 Michel Tagging The final stage of the reconstruction is the Michel tagger. Muons are unstable particles that decay into electrons with a lifetime of $\tau = 2.2 \mu s$. These electrons have a maximum energy of 53 MeV. Since Michel electrons are a delayed, low-energy event, this is done independent of the tracking reconstruction and prior to the hit cleaning algorithm.

There are two taggers in p0dRecon, TP0DTagMuonDecay and TP0DMuonDecayTag (the latter developed by the author). They both operate on a similar principle; find clusters of delayed hits in proximity with a final reconstructed particle. The primary difference is that TP0DMuonDecayTag only allows hits within 30 cm of either end of the track, while TP0DTagMuonDecay searches for clusters at any point along the particle. Candidate Michel

electrons clusters must be > 100 ns after the particle, and must have a total charge < 500 p.e., which corresponds to ~ 55 MeV.

2.4.3 Analysis Software

There are two primary software packages used for ND280 analyses: Highland2 and xsTool. These tools common framework to develop, validate, and replicate physics results across research groups. Highland2 is used for developing selections and propagating detector systematics, while xsTool handles physics systematics, truth unfolding, and cross-section measurements. This thesis is the first P θ D-only analysis developed in this framework. The considerable work of implementing and validating p θ dRecon into Highland2 was performed by the author, with significant help from Zoya Vallari⁵ and Anselmo Cervera⁶.

Highland2 is essentially a collection of software classes designed to make the machinery of accessing the T2K data and propagating systematics uniform. Detector corrections (such as data quality flags or event pile-up rates) are handled here, as are the actual selection criteria for an analysis. Detector systematics are applied on an event-by-event basis and saved to a covariance matrix. Each systematic can be thrown independently or in conjunction with others. Physics and flux systematics are handled in xsTool.

Systematics can be implemented as either a weight or a variation. Weights are used for systematics that only affect the overall event normalization, or that otherwise do not alter the event kinematics themselves (such as the detector mass or the Michel electron efficiency). These systematics weights are applied only once to an event. Systematics that alter some continuous variable within the event (such as the momentum resolution or length reconstruction) are varied repeatedly within an event to determine its affect on the selection.

For Gaussian distributed systematics (as all of the ones used in this analysis are, to a good approximation), Highland2 is passed the mean offset and variance obtained from an independent control sample. The uncertainty is varied from -2σ to $+2\sigma$, as determined

⁵Graduate student at the State Univeristy of New York at Stony Brook.

⁶Faculty at Instituto de Física Corpuscular, Valencia, Spain.

by random throws of a normally-distributed parameter. The number of throws can also be varied; for this analysis, each event has 100 throws. The unvaried parameters are passed to the final selection, along with the variance calculated by these throws.

The output of Highland2 is an array of the relevant kinematics for the event, the true vertices from MC associated with the event, and a covariance matrix of the detector systematics. This output can be easily ported in xsTool.

The xsTool utility is used by T2K to calculate cross-section measurements on any target in ND280. In order to do this, xsTool imports two other packages, T2KReWeight and RooUnfold. T2KReWeight is a T2K specific tool that performs the flux reweighting and propagates the relevant “physics” systematics, such as cross-section uncertainties and final state interactions (FSI). These parameters are continuously updated to reflect the most accurate and up-to-date neutrino-nuclear interaction measurements. RooUnfold is an external package that performs the Bayesian unfolding between the true and reconstructed event kinematics. xsTool then uses these errors and the unfolded truth information to extract the cross-section measurement. More details on this process can be found in Section 4.

3.0 THE P \emptyset D-CONTAINED ν_μ CC-0 π ANALYSIS

Neutrino cross-sections have historically been reported in terms of the relevant interaction mode, and this analysis would have been reported as a ν_μ CCQE measurement[46][21][47]. As modern neutrino experiments have expanded to heavier nuclear targets, the relationship between the true interaction products and what is seen in a detector have become more and more entangled, especially for the “simple” charged current interaction[20].

One consequence of this interconnection is that it is very difficult to do an “apples-to-apples” comparison between separate experiments and between a particular experiment and theory. Increasingly neutrino cross-section measurements are being reported in terms of their “topology,” that is, the particles that are directly measurable in the experimental setup. In a ν_μ CC-1 π^+ event, for example, a μ^- , only one π^+ , and any number of hadrons are present in the detector. A CC-0 π event contains a muon and no pions, with any number of hadrons.

The T2K cross-section group has adopted this standard for all current analyses, and the analysis in this paper follows the guidelines outlined by the collaboration. The goal of this analysis is a cross-section measurement of ν_μ CC-0 π interactions on water for events contained within the P \emptyset D.

3.1 ANALYSIS STRATEGY

The goal of this analysis is to produce the ν_μ -H²O double-differential cross-section in bins of the kinematics of the out-going muon, p_μ and $\cos(\theta_\mu)$, immediately after the interaction¹. The angle θ is defined relative to the axis of motion of the incoming neutrino (Figure 27). Due to the proximity of ND280 to the beam target, the beam cannot be treated as a point source, and this angle is calculated based on the position of the interaction vertex in the detector².

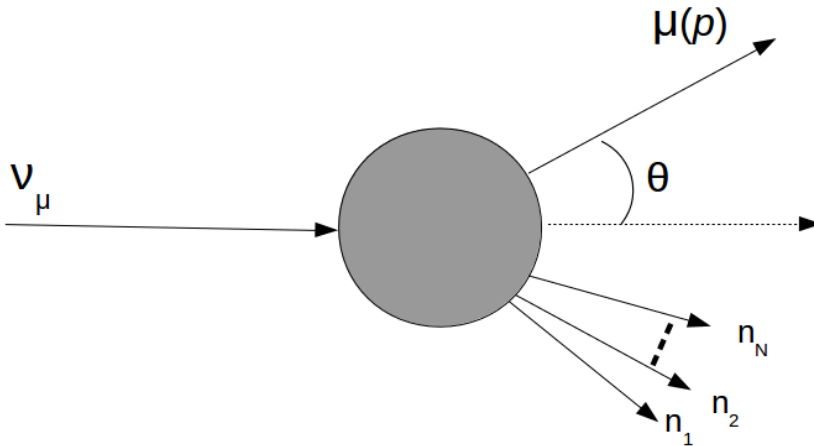


Figure 27: Diagram of the muon kinematics used in this analysis, with an arbitrary number of out-going nucleons. The angle θ is defined relative to the direction of the in-coming neutrino.

In order to calculate the cross-section on water, the CC-0 π interaction rate is measured for both water-in and water-out running modes. The true muon kinematics are found by “unfolding” the reconstructed distributions using the D’Agostini Bayesian unfolding scheme

¹For CCQE interactions, the incoming ν_μ interacts with a neutron to produce a μ -p pair. The cross-section on water is, to a reasonable approximation, a cross-section on oxygen. Throughout this section, the indices for on-water variables will reflect this.

²Obviously, it is impossible to know the exact direction of the incident neutrino for data. Instead, the average beam direction is used. Due to the proximity of ND280 to the beamline production, this average direction changes slightly for different parts of the detector (that is to say, the neutrino beam cannot be treated as a point-source for ND280, and incoming neutrino trajectories are not parallel across the detector.) The position of the reconstructed vertex determines the neutrino beam direction used.

in RooUnfold [48, 49]. This step is performed independently for each sample. The true unfolded water-out spectrum is then subtracted from the unfolded water-in one to reproduce the water-only muon kinematics. The expected water-only rate is given by

$$N_{obs}^O = \frac{N_{unf}^w}{\epsilon_w} - \frac{N_{unf}^a}{\epsilon_a} \quad (3.1)$$

where N_{unf}^w (N_{unf}^a) and ϵ_w (ϵ_a) are the unfolded event rates and efficiencies for water-in (water-out, or “on-air,” hence the label a), normalized by p.o.t. This equation holds both for the overall event rate as well as the event rate for any given bin in the muon kinematics.

The majority of CC-0 π events will have only a muon in the final state, since the much heavier protons have a significant energy threshold to overcome before being reconstructed in the P \emptyset D. This analysis is also the first to attempt to determine the directionality of particles in the P \emptyset D, which needs further study before being extrapolated to multi-track events. With these considerations in mind, this thesis limits its scope to one track events. Due to the relative interaction rates and the neutrino energy scales involved, the majority of these one track events will be charged-current interactions. While the particle ID in p \emptyset dRecon does attempt to distinguish between protons and muons, it has limited success in doing so. A data-driven PID developed for the P \emptyset D neutral-current elastic analysis is used here in addition to the standard p \emptyset dRecon ones.

There are two main reasons to focus on events entirely contained within the P \emptyset D: to expand the T2K cross-section group’s accessible phase-space, and to accurately reconstruct the muon momentum. This constraint ensures that the selected sample is independent from on-going T2K results (see below) and has a negligible effect on the acceptance of backward-going muons. The acceptance for high-angle muons is quite low, though³ (The selection efficiency as a function of muon angle can be found below in Figure 37 and Figure 38; Section 3.2.9) .

³This is a combination of the reconstruction criteria of > 4 X/Y layers and the geometry of the P \emptyset D (see Sections 2.2.2, 2.4.2. The reconstruction efficiency of the P \emptyset D goes to 0 as the angle approaches 90° with respect to the Z-axis.

There is an existing CC- 0π measurement on the P \emptyset D water target which includes events exiting the downstream end of the P \emptyset D and then entering the Tracker. This selection has excellent momentum reconstruction ($\sim 3\%$) without an acceptance limit on the magnitude momentum of the muon. Therefore, there is no loss of information to T2K by not accepting muons that exit out the downstream end of the P \emptyset D in this analysis. The angular acceptance of this existing measurement, however, is quite limited ($\lesssim 30^\circ$ with respect to the neutrino beam direction), and a study which includes backward-going muons greatly expands the angular phase-space.

The constraint that each event must be contained within the P \emptyset D also allows for accurate momentum reconstruction. Without the aid of the TPC chambers in the tracker, momentum must be reconstructed from range, which is only possible when the full path of the particle is known. Without robust tracking capabilities in either the P \emptyset D-ECal or the SMRD, accurate momentum reconstruction for particles exiting the sides of the P \emptyset D is problematic, and those topologies are not included in this analysis.

3.2 SELECTION CRITERIA

There are seven successive cuts for this selection:

1. Event Quality
2. One and only one P \emptyset D track
3. No other GlobalRecon objects
4. Track is fully contained
5. Direction Criteria Applied
6. Vertex is in the P \emptyset D fiducial volume
7. Proton/Muon PID

Table 2: Event rate by cut for cuts 4-7 for the forward-going (in white) and backward-going (in gray) selections for Runs 2-4 in Water-in mode. There is a significant excess in data in the backward selection.

Cut	Data	NEUT	Data/NEUT
Track is Contained	14394	12916	1.11
Track Direction	11902	11061	1.08
	2492	1855	1.34
Fiducial Volume	4170	4064	1.03
	967	774	1.25
Muon PID	2755	2694	1.02
	562	443	1.27

Cuts 1-3 are considered a “preselection,” meaning that the ND280 data and MC files are scanned to check for events which have either a true event in the P \emptyset D or the relevant reconstructed objects. Table 2 details the effect cuts 4 through 7 have on the selected event rate. The forward-going and backward-going muon samples are listed separately after the direction criteria is applied. The backward selection shows a clear excess in data that is not present in the forward selection.

3.2.1 Event Quality

While beam is being delivered, the ND280 subdetectors are monitored to maintain good data quality (see Section 2.4.1). This cut simply checks that there are no flags from the DAQ. Since this analysis relies only on the P \emptyset D, only flags from that subdetector are relevant, which yields a higher DAQ efficiency than the ND280 as a whole (Table 3). Fewer than 4% of events fail to pass this step.

Table 3: The DAQ efficiency rates for the P \emptyset D and the ND280 for Runs 2,3, & 4.

Run #	P \emptyset D DAQ Efficiency (%)			ND280 DAQ (%)
	Water-In	Water-Out	Combined	All Detectors
2	96.33	96.99	96.87	70.39
3	N/A	99.05	99.05	98.64
4	98.71	99.08	99.05	95.91

3.2.2 One and Only One P \emptyset D Track

The next selection criteria checks that there is only one P \emptyset D track present in the event. Any showering objects or reconstructed objects that did not pass the tracking reconstruction are excluded, and misidentification of a muon as an EM object is negligible ($< 0.1\%$ from cosmic and particle gun studies). No consideration of whether the track is contained or not is made at this point.

3.2.3 No Other GlobaRecon Objects

The set of final GlobalRecon objects is checked to determine any activity in the rest of ND280. If a global track is found (other than the one in the P \emptyset D), the event is excluded. If the global track found in the P \emptyset D contains any segments outside of the P \emptyset D, the event is excluded.

3.2.4 Track is Fully Contained

After there is a single P \emptyset D-only particle selected, the most upstream and most downstream ends of the track are found by looping over the positions of each node in the track. Each end is then required to be no less than 10 mm from the active edges of the detector,

and no less than 20 mm from the upstream and downstream ends. This corresponds to 2-3 scintillator bars on the sides of the P \emptyset D, and 1 P \emptyset Dule on the upstream and downstream ends. The tracking efficiency of the scintillator bars in the P \emptyset D is $> 99\%$ [36], which allows for such a narrow veto area around the edges of the active region.

Once a track has been identified as being contained, the direction criteria is applied. As detailed in Section 2.4.2, the P \emptyset D reconstruction software assumes that all tracks are forward-going, therefore the directionality of the particle must be determined by the analyzer. Details on the direction criteria are below (Section 3.2.7).

3.2.5 Vertex in the Fiducial Volume

The fiducial volume (FV) used in this analysis is standard for P \emptyset D analyses on water. It is defined as a span of 1600 mm in X, 1740 mm in Y, and 1705 mm in Z, centered around the geometric center of the P \emptyset D. The edge of the FV is approximately 25 cm from the edge of the active material in both X and Y, and runs from the center of the most upstream water bag to the center of the most downstream one. This definition ensures that the FV is fully contained within the filled volume of the P \emptyset D when running in water-in mode.

After the selected track passes the containment requirement, the direction of the particle is determined, and the beginning of the track is assigned to be the reconstructed interaction vertex. If this vertex is not within the FV boundaries, the event is excluded. Accurate directional determination is important not only for an accurate reconstruction of the muon phase-space, but also for the accurate inclusion and exclusion of events originating in the P \emptyset D FV (see Figure 28).

3.2.6 Momentum Reconstruction

Two different methods for reconstructing the muon momentum are used in this analysis. The first (developed by the author) uses a simple linear extrapolation from the reconstructed

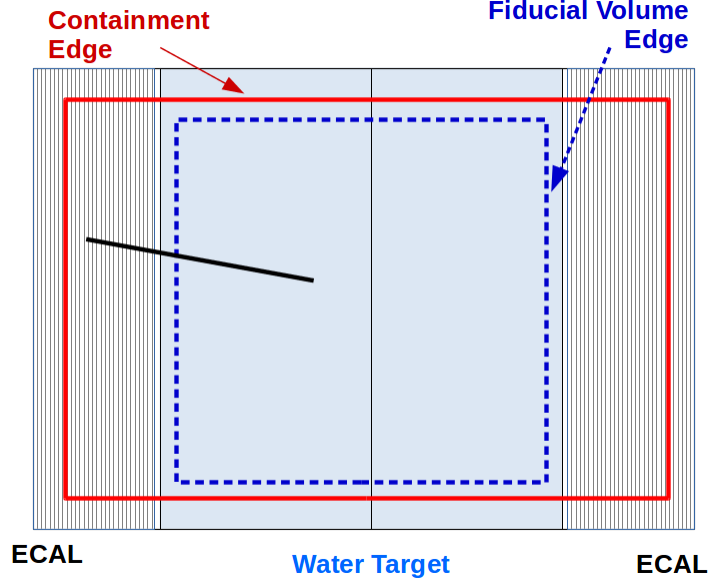


Figure 28: A diagram of the containment volume (solid red) and fiducial volume (dashed blue). The muon track here can either be reconstructed as inside or outside the FV depending on the determined direction.

track length using a MC fit. The second method (developed for a neutral current elastic study, and modified by the author for this analysis) uses the Bethe formula (Equation 3.2) to calculate the momentum loss from the geometry of the P \emptyset D that the track passes through.

$$-\frac{dE}{dx} = \left(\frac{ze^2}{4\pi c^2 \epsilon_0} \right)^2 \frac{4\pi Z\rho N_A}{Am\beta^2} \left[\ln \left(\frac{2mc^2\beta^2}{I(1-\beta^2)} \right) - \beta^2 \right] \quad (3.2)$$

In this equation, Z , A , and ρ are defined by the stopping material of the detector, I is the mean ionization energy of an atom in the medium, and $\beta = v/c$ [50]. Muons with momenta between ~ 100 MeV - 10 GeV have a near constant energy loss⁴, which encompasses the majority of the momentum phase space for this analysis (Figure 29).

The algorithm takes small steps with a constant areal density, 0.05 g cm^{-2} , from the

⁴Particles in this region of the Bethe formula are often referred to as *minimally ionizing particles*, or MIPs, since their energy loss in the medium is at a minimum. The fact that the majority of muons produced in T2K are MIPs helps justify why momentum reconstruction from a linear fit is feasible for muons in the P \emptyset D.

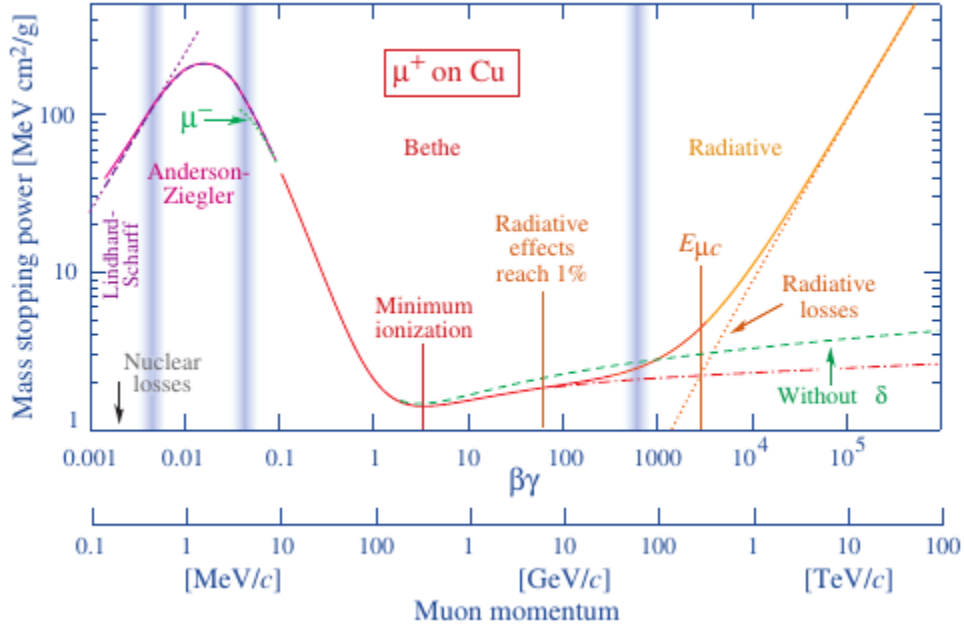


Figure 29: The Bethe-Bloch formula for the energy loss of μ^+ on copper[51].

most downstream to the most upstream end of the track. For each material the track travels through, the atomic information and areal density are updated using the values in Table 4. The material density of the P \emptyset D is detailed in [52].

For water-out running, the linear fit method is more accurate, while the Bethe method is more effective in water-in mode. Since the systematic uncertainties are uncorrelated between water-in and water-out for a given method, there is no issue with using one method for one mode and the other for the other. For this analysis, the linear fit method is used for momentum reconstruction in water-out mode, while the Bethe method is used for water-in.

Ideally, both momentum reconstruction methods would be compared to data using a control sample which uses the TPC momentum to verify momentum loss in the P \emptyset D. However, there are several problems with this approach. The two best options for an independent muon sample in the P \emptyset D are a sand muon sample (muons created from neutrino beam interactions in the sand upstream of ND280) and a cosmic ray sample. The issue with using the sand muon sample is that the muons need to pass completely through the P \emptyset D to reach

Table 4: The material density of the P \emptyset D components and their uncertainties.[52]

P \emptyset D region	Material	Areal Density (g cm ⁻²)
P \emptyset Dule skin	Polystyrene	0.144 (0.024)
Brass Radiator	Copper	1.088 (0.032)
Glue	Epoxy	0.034 (0.0072)
Water Target Boundary	HDPE	0.597 (0.048)
Water Bags	HDPE	0.00323 (0.00003)
ECal Steel	Iron	0.36 (0.042)
ECal Pb Radiator	Lead	3.924 (0.058)
Water Target	Water	2.733 (0.023)
Scintillator	Polystyrene	1.72 (0.003)

the TPCs. It is impossible to correlate a particular TPC momentum to a particular track length.

The main roadblock with using the cosmic ray sample is statistics. In order to perform a meaningful comparison between data and MC, a selection of muons that pass through the TPC and then stop in the P \emptyset D is needed. For both data and MC, this sample is extremely small (~ 100 s of events). This sample is also necessarily constrained in the kinematic range accessible, with most events limited to the Downstream water-target and the Central ECal. For these reasons, the momentum resolution studies here were done using a generated MC sample only. Similar studies have been done using the cosmic ray sample for the P \emptyset D \rightarrow Tracker analysis, since that analysis has a similarly constrained phase space[53].

Two particle gun samples were created, one for water-in mode and one for water-out. Both were generated using the same version of NEUT as the beam MC and then processed with the Production 6B ND280 reconstruction software. The muons were generated uniformly through the P \emptyset D with an isotropic angular distribution and a momentum spectrum ranging from 150 MeV to 750 MeV. This ensures complete coverage over the full phase-space

and detector geometry for the contained selection.

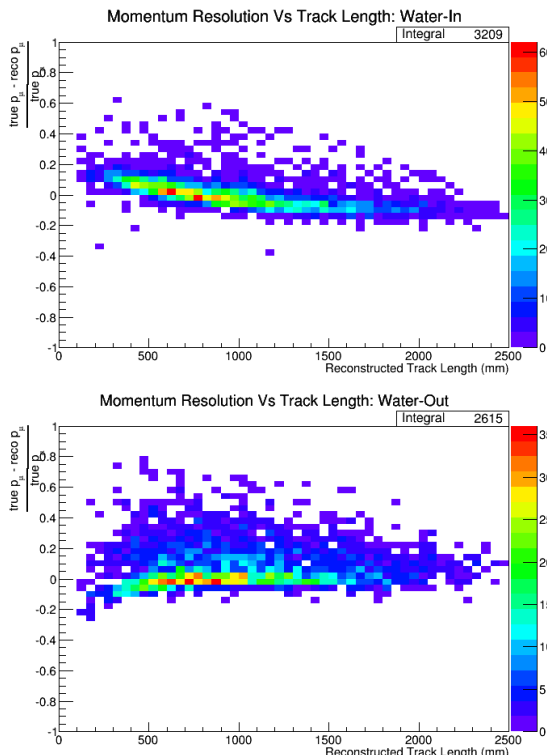


Figure 30: Momentum resolution vs length for water-in (top) and water-out (bottom) particle gun samples.

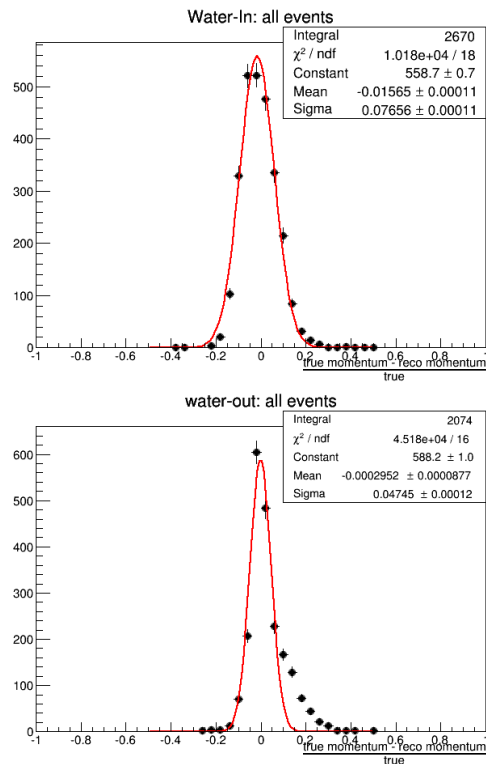


Figure 31: Momentum uncertainty for water-in (top) and water-out (bottom) particle gun samples.

The momentum reconstruction resolution from these studies are $\sigma_p = 0.0766$ (0.0531) for water-in (water-out). These values are consistent with with the $P\emptyset D \rightarrow \text{Tracker}$.

3.2.7 Direction Criteria

Three variables were developed by the author and studied for their directional discriminating power: the relative timing between the upstream and downstream ends of the track (Δ_{time}), the bend in the track due to the magnetic field (β), and the difference in the distance of the Michel electron (when present) from either end of the track (Δ_{Michel}). A comparison of the relative effectiveness of each variable is given in Table 5.

The relative timing variable, $\Delta_{time} = t_{us} - t_{ds}$, is a simple subtraction of the time at the most downstream node of the track (t_{ds}) from the time at the most upstream one (t_{us}). If $\Delta_{time} > 0$, that is, if the upstream node is timed to have occurred after the downstream one, then the track is determined to be traveling upstream. This calculation was not possible until the Production 6 release of the ND280 software, which lowered the timing resolution to ~ 1 ns.

The Michel distance variable is another simple subtraction, $\Delta_{Michel} = d_{US} - d_{DS}$. The distance from both ends of the track to the Michel electron are calculated (d_{US} & d_{DS}), and then subtracted from each other. If $\Delta_{Michel} < 0$ the track is determined to be traveling upstream.

In terms of selecting out backward-going muons, the Michel distance variable performs the most effectively. However, this criteria can only be applied to events in which a Michel electron is present. Due to a combination of the timing of the TripT electronics and capture of the μ^- in the detector, a stopped muon decays into a detectable electron $\sim 55\%$ of the time. Requiring a Michel electron to be present, then, cuts the available statistics roughly in half as compared to either Δ_{time} or β .

The tool for measuring the bend due to the magnetic field in the P \emptyset D was originally developed to determine the charge of a forward-going (anti) muon. However, if that assumption is changed to assume the particle is in fact a μ^- then the bend can be used to determine direction. This assumption holds since the $\bar{\nu}_\mu$ contamination of the beam is $\sim 1\%$, while a contained selection of muons in the P \emptyset D will be $\sim 20\%$ backward-going.

The bend is defined as $\beta = \Sigma(\Theta_n - \Theta_{n-1})$, where Θ_n is the angle off the Z-axis in the YZ-plane at node n . Node $n = 0$ is taken to be the most upstream node, and the summation progresses downstream until the end of the track is reached. Scattering of the through-going muon is on the same order as the bending due to the magnetic field, which limits the effectiveness of this calculation, and β has no discriminating power below ≈ 500 mm. The backward-going muon momentum distribution peaks between 250-300 MeV, which corresponds to a track length of ≈ 700 mm (900 mm) for water-in (water-out). This explains

per 10^{20} pot	Water-In		Water-Out		
Variable	# of Events	% Backward	# of Events	% Backward	$\frac{Water-In}{Water-Out}$
None	6788	0.19	3704	0.24	1.83
Δ_{Michel}	750	0.52	464	0.60	1.62
Δ_{time}	1712	0.47	913	0.64	1.88
β	2724	0.27	1841	0.31	1.48
$\beta + \Delta_{time}$	711	0.71	604	0.70	1.18
$\Delta_{Michel} + \Delta_{time}$	423	0.75	317	0.74	1.33
All	265	0.74	233	0.75	1.14

Table 5: A comparison of Δ_{time} , Δ_{Michel} , and β . These studies were conducted on a selection of Production 6B NEUT beam MC files independent from those used for the cross-section study

why β performs so poorly as compared to Δ_{time} or Δ_{Michel} .

In the final analysis, only Δ_{time} is used for determining the direction of the selected tracks. While a combination of β and Δ_{time} does produce a selection with a higher “purity” of backward-going tracks than Δ_{time} alone, it does so at the cost of excluding backward-going muons with low momenta. The joint use of Δ_{time} and Δ_{Michel} likewise increases the purity, but suffers a drop in statistics of almost 75%.

It is worth noting too that the ratio of water-in to water-out event rates with no directional criteria and the ratio with Δ_{time} applied are very similar. This gives confidence that Δ_{time} affects the acceptance in both the water-in and water-out samples in a similar manner, which is helpful for the water subtraction measurement.

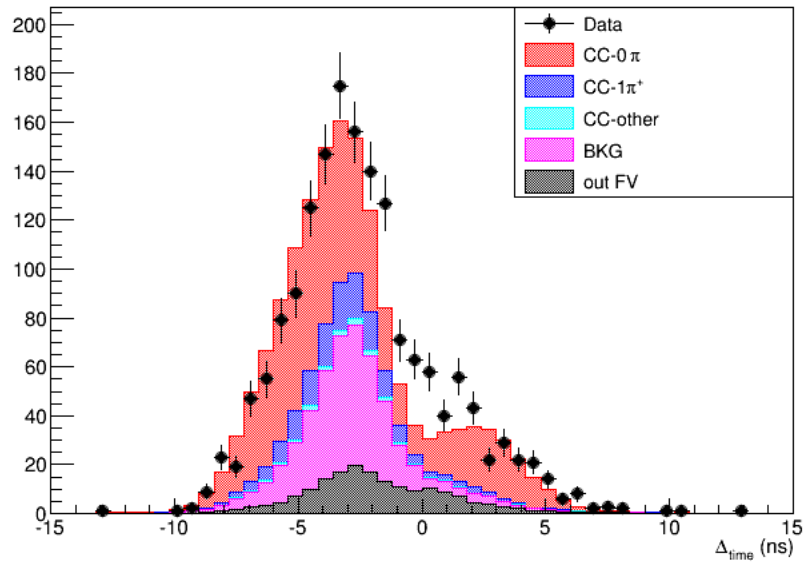
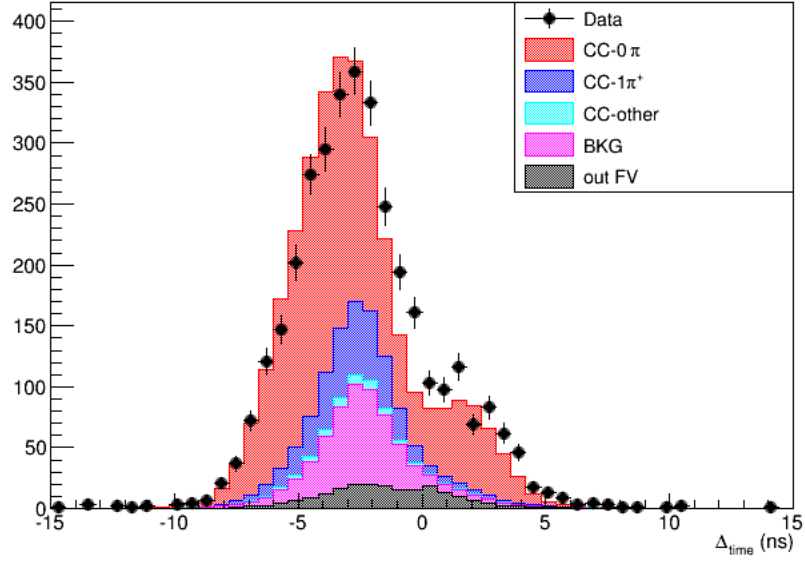


Figure 32: Δ_{time} for Genie fake data and NEUT MC for water-in (top) and water-out (bottom).

3.2.8 Proton/Muon Particle Identification

The internal p0dRecon particle ID (PID) was optimized to identify electrons and π^0 's. It is quite capable of selecting out these “showering” events from track-like ones, but it is less successful at distinguishing heavy charged particles from each other. This is especially true for the contained sample, as whether or not the track exits the P0D is one of the factors used to tag a particle as a muon.

Due to the difference in mass, the expected energy loss in the P0D differs between protons and muons. For a given momentum, $\beta\gamma$ for the heavier protons is lower than that for muons, which means the energy loss is greater (see Figure 29). Whereas the energy deposited in the P0D by a muon is approximately constant until the last several nodes, protons contained in the detector are never in the MIP region.

Sand muons were used to generate a charge-deposited profile in both data and MC. Neutrino interactions in the sand surrounding the pit that houses ND280 create particles that enter the upstream end of the P0D; primarily a mix of electrons, protons, and muons. Removing all particles that travel less than 1 m generates a high-purity sample of muons.

The energy deposited as a function of distance from the end of the track is shown in Figure 33. The width of the distance bins is the distance between P0Dules in the water-target (67.1 mm). There is a clear signature for a stopping muon in the P0D that is consistent in both data (Figure 33a) and MC (Figure 33b). To generate the parameters used for the PID, the most probable values (MPV) and variance for the energy deposited are extracted for the last six bins (which corresponds to a track length of 410 mm).

The PID is calculated as a “pull” from the expected muon distribution, meaning that a muon should return a PID value of 0, while protons are “pulled” to values greater than 0. This pull is calculated for each bin, and then summed together, by the following formula:

$$Pull = \sum_{node,n=0}^{node,n=N} \frac{Q_{meas} - \hat{Q}_{exp,n}}{\sigma_{exp,n}} \quad (3.3)$$

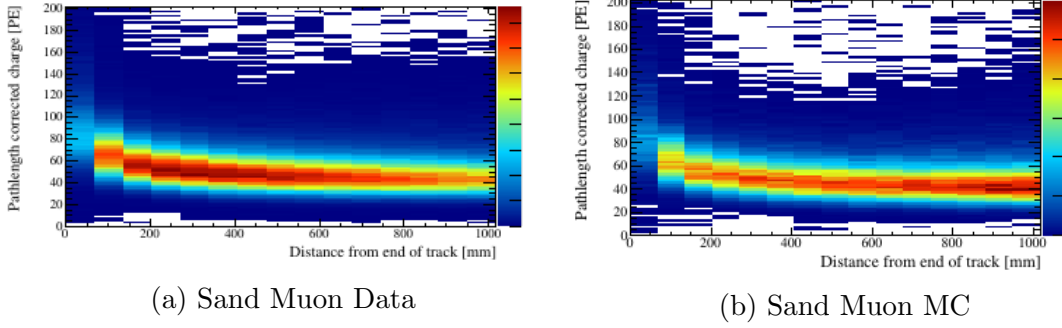


Figure 33: The expected charge deposited for a stopping-muon was determined from sand muon MC and data.[54]

where $\hat{Q}_{exp,n}$ and $\sigma_{exp,n}$ are the MPV and uncertainty extracted from data in bin n , and $n = 0$ corresponds to the last node of the track. This calculation can be performed on either end of the track, which allows the pull to be accurately determined based on the selected direction of the muon.

Histograms of the Pull PID for beam MC can be seen in Figure 34. The muon peak is slightly offset from 0 for the water-out sample. This is due to a difference between the sand muon data and MC parameters, and is easily addressed in systematics (Section 4.2.5).

3.2.9 Selection Kinematics

The reconstructed muon kinematics for events passing all selection cuts can be seen in Figure 35 and Figure 36. The NEUT MC is shown by event topology, and the black markers are GENIE fake data. While there is good general agreement between the two generators, there are some discrepancies between them, especially in the lower momentum bins. This behavior is expected, given some of the more significant differences between NEUT and Genie are in the implementation of nucleon emissions, final state interactions, and high momentum transfer interactions; all of which have a larger effect on less energetic events.

Selection efficiency as a function of the reconstructed muon kinematics are shown in

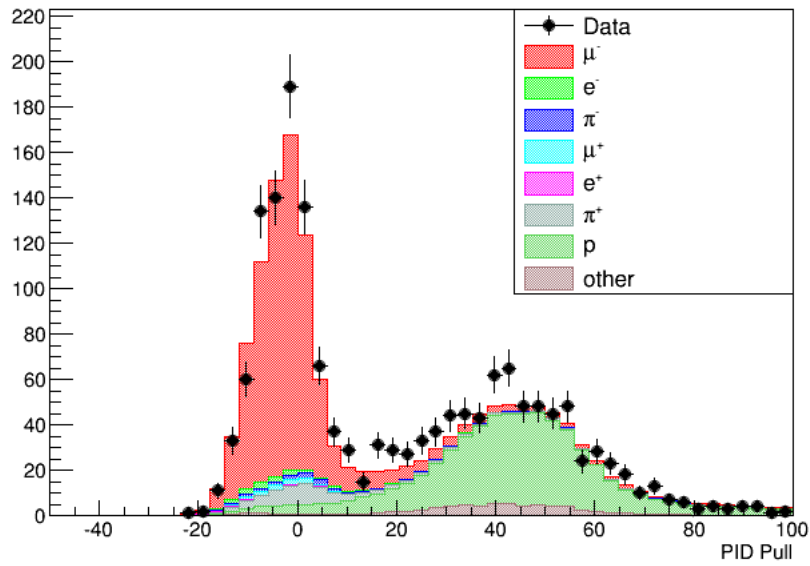
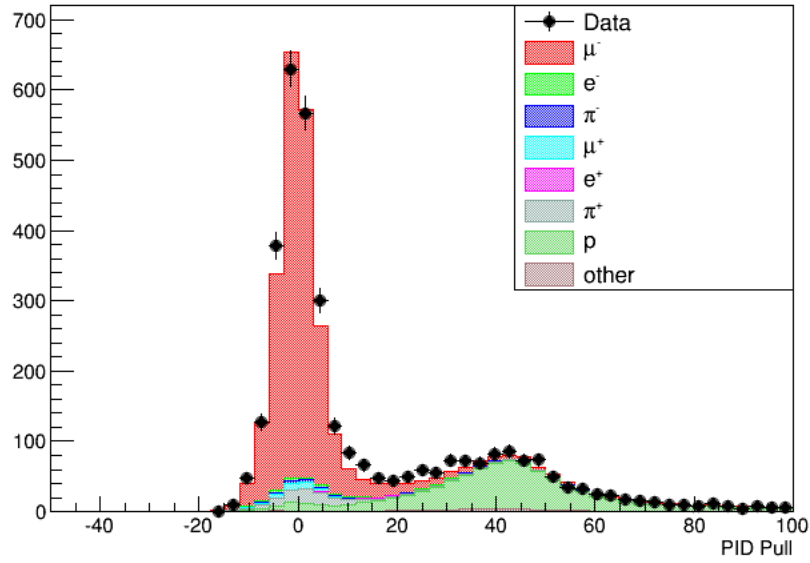


Figure 34: Histogram of the Pull PID for water-in (top) and water-out (bottom) for data and beam MC.

Figure 37 and Figure 38 for both NEUT and Genie. In general, both generators show similar behavior. The low efficiency for momentum bins above 700 MeV (600 MeV) for water-in (water-out) and for $\cos(\theta)$ bins between -0.3 and 0.3 are due to the geometry of the P \emptyset D. These regions are at the very edge of what can reliably reconstruct and are scarcely populated.

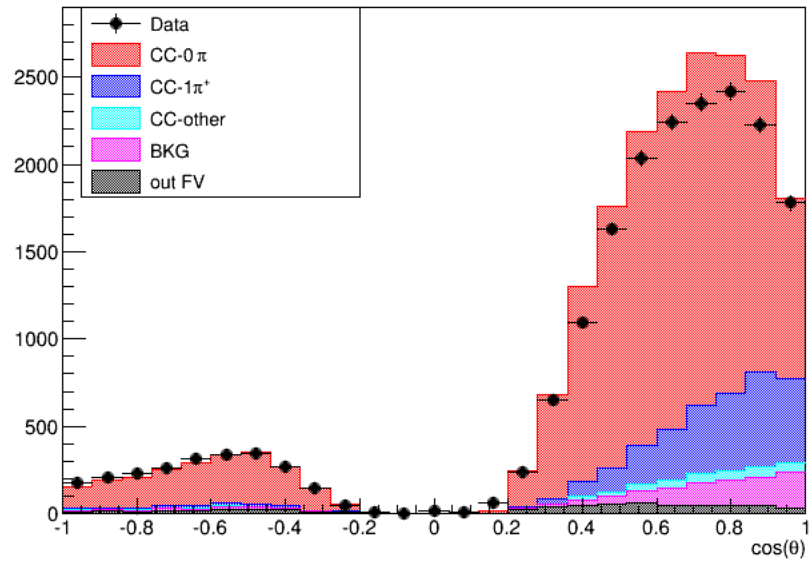
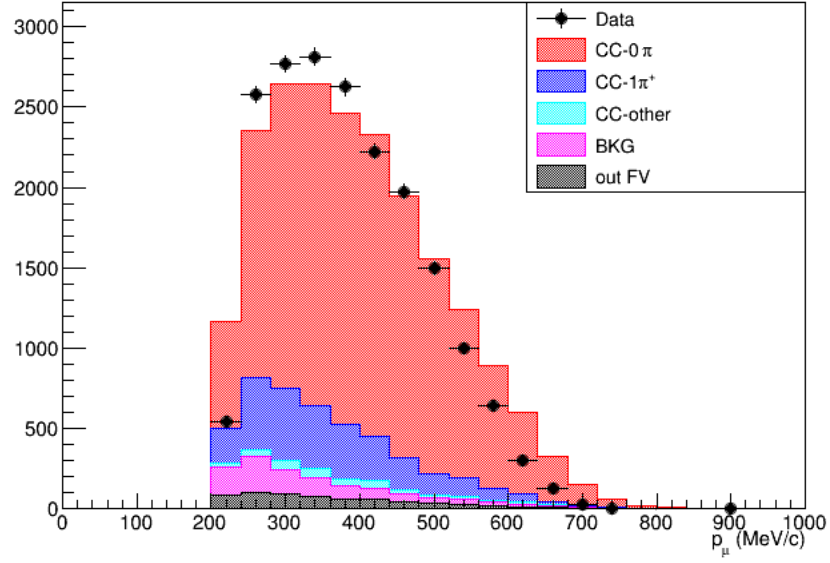


Figure 35: Water-in reconstructed muon kinematics: muon momentum p_μ (top) and $\cos(\theta)$ (bottom).

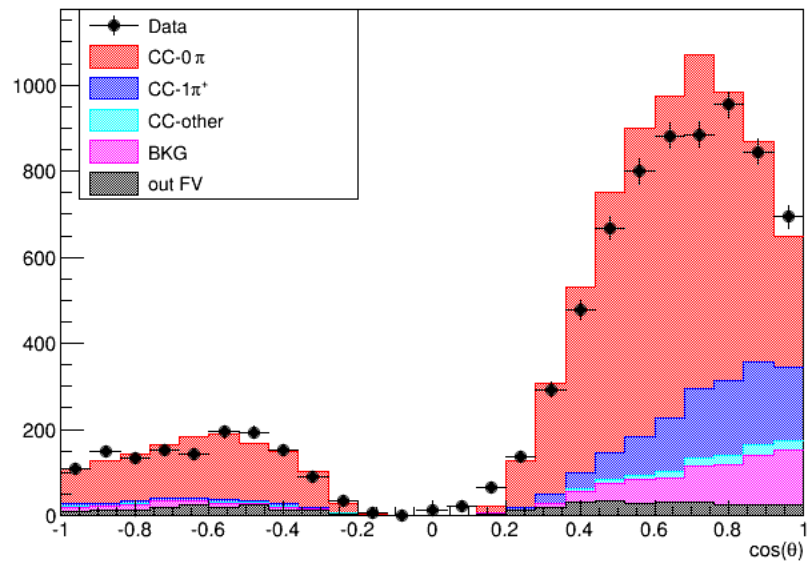
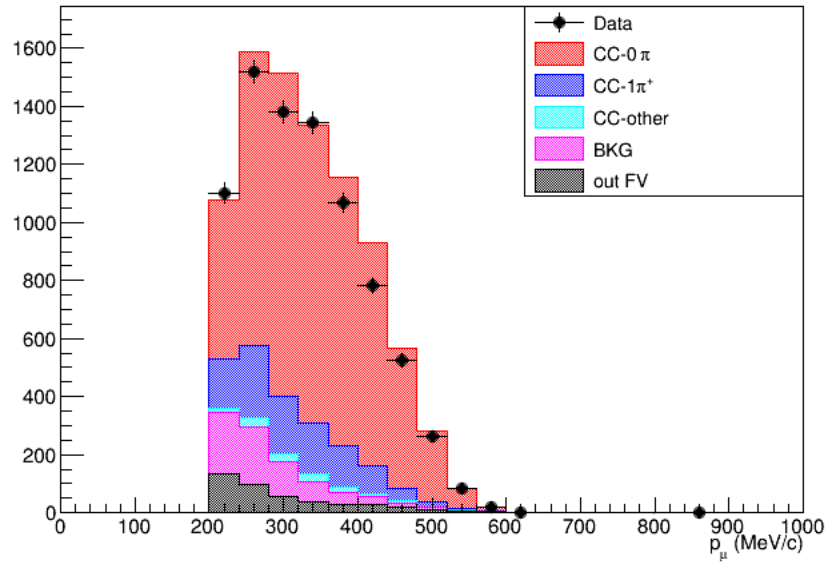


Figure 36: Water-out reconstructed muon kinematics: muon momentum p_μ (top) and $\cos(\theta)$ (bottom).

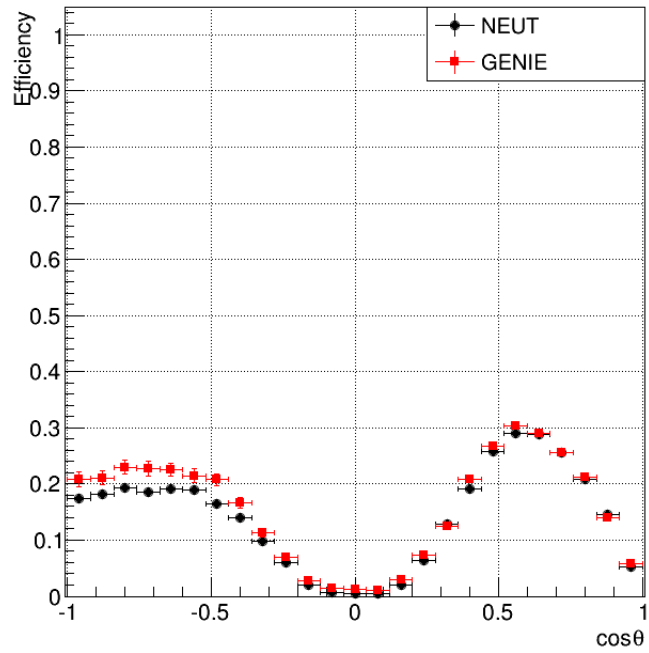
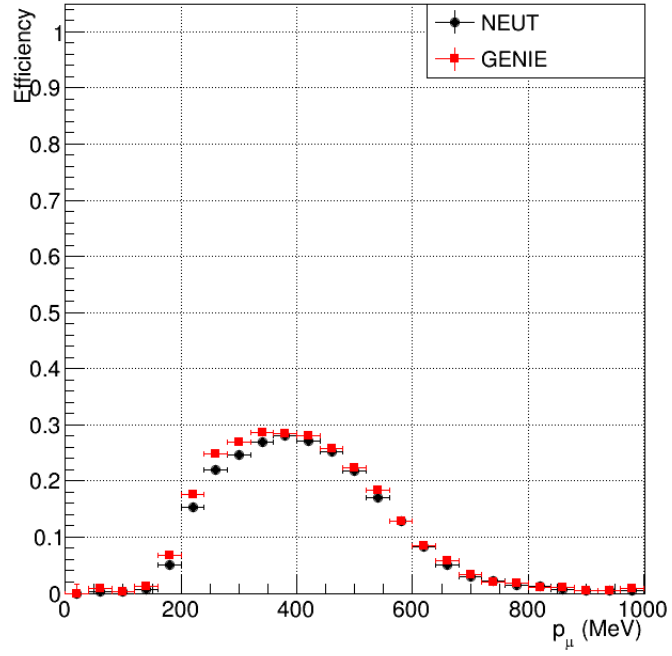


Figure 37: Water-in selection efficiency as a function of reconstructed muon momentum (top) and $\cos\theta$ (bottom). Efficiencies for both NEUT and Genie are shown.

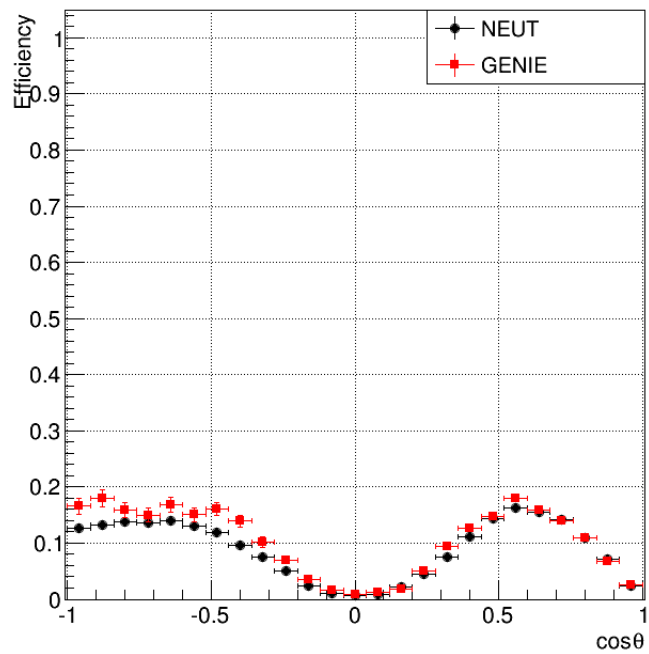
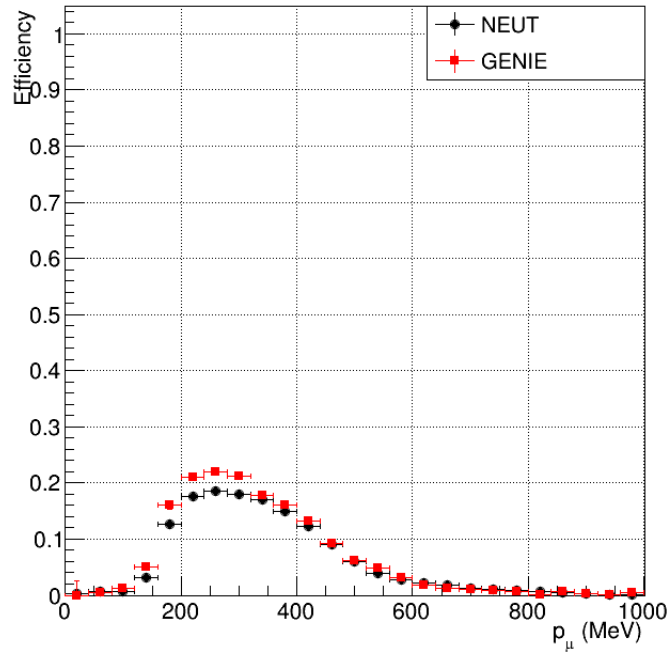


Figure 38: Water-out selection efficiency as a function of reconstructed muon momentum (top) and $\cos\theta$ (bottom). Efficiencies for both NEUT and Genie are shown.

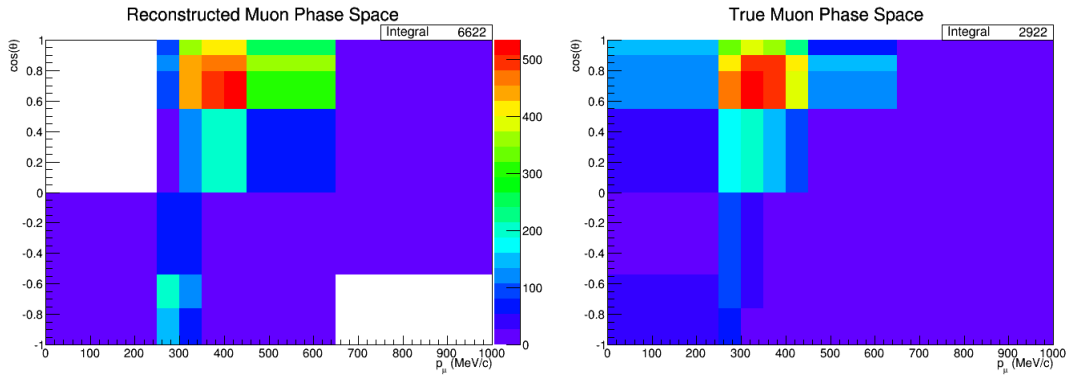


Figure 39: Water-In reconstructed (left) and true (right) muon phase space.

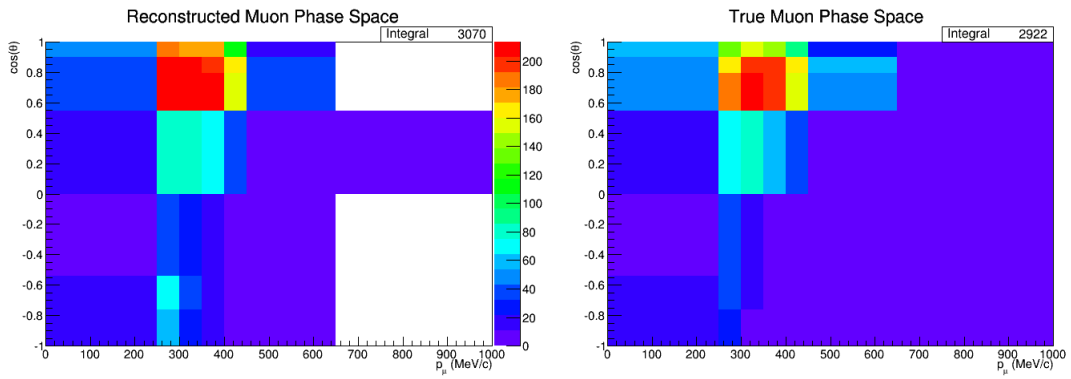


Figure 40: Water-Out reconstructed (left) and true (right) muon phase space.

Table 6: A breakdown of the event topologies in the final selection by percentage of the total number of selected events. Any event that originates outside the P \emptyset D fiducial volume is considered OOFV, regardless of its topology.

Topology	Water-In	Water-Out
CC-0 π	75.2	69.9
CC-1 π	13.5	12.5
CC-Other	1.8	1.7
NC	5.9	9.5
OOFV	3.7	6.5

A breakdown of the selection purity and backgrounds is given in Table 6. Events originating in the P \emptyset D FV are listed by true topology, while any event with an interaction vertex outside the FV is considered "out-of-fiducial volume" (OOFV), regardless of topology.

Both water-in and water-out samples have a high CC-0 π purity ($\gtrsim 70\%$). The single largest background are CC-1 π events in which the pion is not reconstructed, and this rate is similar between the two samples. The CC-other background are events with any other charged-current topology aside from CC-0 π or CC-1 π .

There is a significant increase in both the neutral current and OOFV backgrounds for the water-out sample, which is expected. When the water is drained from the P \emptyset D, fewer muons are contained within the detector due to the reduced energy loss. At the same time, more protons are able to be reconstructed. Both factors together lead to a higher percentage of neutral current events. The OOFV background is examined in more detail in Section 4.2.2.

3.3 WATER SUBTRACTION METHOD

The calculation for the ν_μ cross-section on water in bin i is given by

$$\sigma_i = \frac{N_{obs}^O}{\Phi N_n \Omega_i} \quad (3.4)$$

where Φ is the beam flux, Ω_i is “solid angle” of the phase space of bin i , N_n is the number of neutrons in the fiducial volume, and N_{obs}^O is described in Equation 3.1. The flux can vary from run to run, so it is more accurate to use the p.o.t. normalized fluxes for water-in (Φ^w) and water-out (Φ^a) separately. We can rewrite Equation 3.1 and 3.3 as follows:

$$\sigma_i = \frac{N_{obs}^O}{\Phi^w N_n \Omega_i} \quad (3.5)$$

$$N_{obs}^O = \frac{N_{unf}^w}{\epsilon_w} - F \frac{N_{unf}^a}{\epsilon_a} \quad (3.6)$$

where $F = \Phi^w / \Phi^a$ is the ratio of the integrated water-in to water-out fluxes, normalized by p.o.t.

Calculating σ_i is straight-forward once N_{obs}^O has been found. This step requires untangling the detector effects that smear the measured data for both water-in and water-out selections.

3.3.1 Bayesian Unfolding

This analysis uses the D’Agostini Bayesian unfolding method to extract the true muon kinematics from the measured data[48, 49]. Each bin of the true kinematics is considered a “cause,” while each reconstructed bin is considered a separate “effect.” The problem is then converted from attempting to find the spectrum that best fits the data to calculating

the probability that a given effect was produced by a given cause. This approach can be formulated by the usual Bayesian relation below:

$$P(C_i|E_j) \propto P(E_j|C_i)P(C_i) \quad (3.7)$$

This can be read the following way: the probability that an observed event E_j was due to cause C_i is proportional to the probability for C_i to cause E_j times the probability for C_i to occur. In the usual Bayesian terminology, $P(C_i|E_j)$ is the *posterior*, $P(C_i)$ is the *prior*, and $P(E_j|C_i)$ is the *likelihood*. The likelihood is calculated from MC.

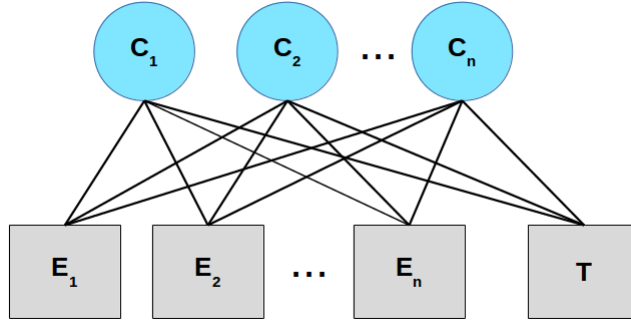


Figure 41: A diagram of the D'Agostini unfolding binning. Each cause (a bin in MC truth) is probabilistically related to each effect (a bin in measured muon kinematics), as well as an additional inefficiency bin, T [49].

This process is an iterative one, and acceptable unfolding results can be obtained when using a flat *prior*. The probability of each cause can be updated from the unfolded *posterior* by the following relationships:

$$\hat{P}(C_i) \equiv P(C_i|n(E)) = \frac{\hat{n}(C_i)}{\hat{N}_{true}} \quad (3.8)$$

$$\hat{N}_{true} = \sum_{i=1}^{n_C} \hat{n}(C_i) \quad (3.9)$$

where $n(C_i)$ and $n(E)$ are the number of causes and effects, respectively, and the “hat” ($\hat{}$) denotes an unfolded quantity. However, each iteration increases the statistical uncertainty of the results, and the unfolded results are dominated by the *likelihood*, not the updated *priors*, which encourage a “less is more” approach. The current practice for T2K cross-section analyses is to use a *prior* obtained from MC truth information and to perform a single iteration.

The *likelihood* is implemented as a response matrix, which is populated by the number of events in each true and reconstructed MC bin⁵. The response matrix is combined with the probabilities of the causes to generate the unsmearing matrix, \mathbf{S} (i.e. the *posterior* in Equation 3.3.1), which is normalized and combined with the acceptance efficiency in each bin to calculate the unfolding matrix \mathbf{U} .

The measured effects are transformed by \mathbf{U} . Since the response matrix is generated from a particular, finite MC sample, there is no unique matrix \mathbf{U} for any given selection, and the unfolding process can only be expected to *exactly* reproduce the true spectrum when given the sample used to generate the matrix in the first place. This is a good way to check that the unfolding machinery is in fact working. The results of this check can be seen in Figure 42, where the unfolded cross-section for arbitrary binning agrees exactly with the MC truth.

With the unfolding matrix constructed, the translation from the measured data from MC or data to the “expected” signal is simply

$$N_i^{exp} = \sum_{j=0}^{n_j} U_{ij} N_j^{meas} \quad (3.10)$$

The binning used for this process was chosen to minimize the effect of statistical fluctuations. Areas of low selection efficiency were excluded, and only regions of the phase space with acceptance in both water-out and water-in modes are used. Muons with $p_\mu < 250$

⁵This matrix need not be (and usually isn't) symmetric or even invertable. In fact, there is no requirement that the same binning is used for both the truth and reconstructed, although it is for this analysis. In the absence of infinite statistics and exact knowledge of background effects, the unfolding process is stochastic in nature, whereas matrix inversion is inherently deterministic, which is why unfolding avoids many of the pathologies that plague inversion methods[48, 49]

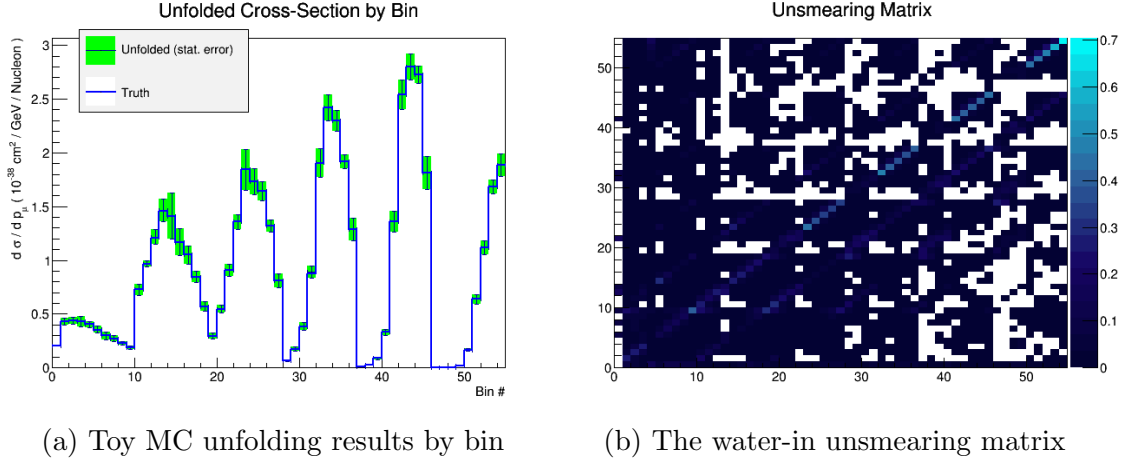


Figure 42: To test the unfolding method, the same water-in MC sample was used as both the measured and true “data.” The unfolding process exactly recreates the true cross-section

MeV or $p_\mu > 650$ MeV are not used in the water-subtraction calculation (see the selection efficiency as a function of reconstructed momentum, Figures 37 and 38). In order to properly account for correlations between the forward-going and backward-going samples, the full angular phase space is used. However, the high angle regions of low efficiency and low statistics are merged into bins with higher selection efficiency.

To effectively display the unfolding results, bins in two dimensions are translated into one-dimensional plots by bin number. A schematic of this is shown in Figure 43 for an arbitrary result. The zero-ith bin is background.

3.3.1.1 Background Backgrounds are easily incorporated into this method through one of two ways: subtracting the expected background off the measured data, or via a purity correction. Both of these approaches can be done with or without a sideband sample. The relationship of the background to the cross-section is (roughly)

$$\sigma \propto N_S = N_T - B \quad (3.11)$$

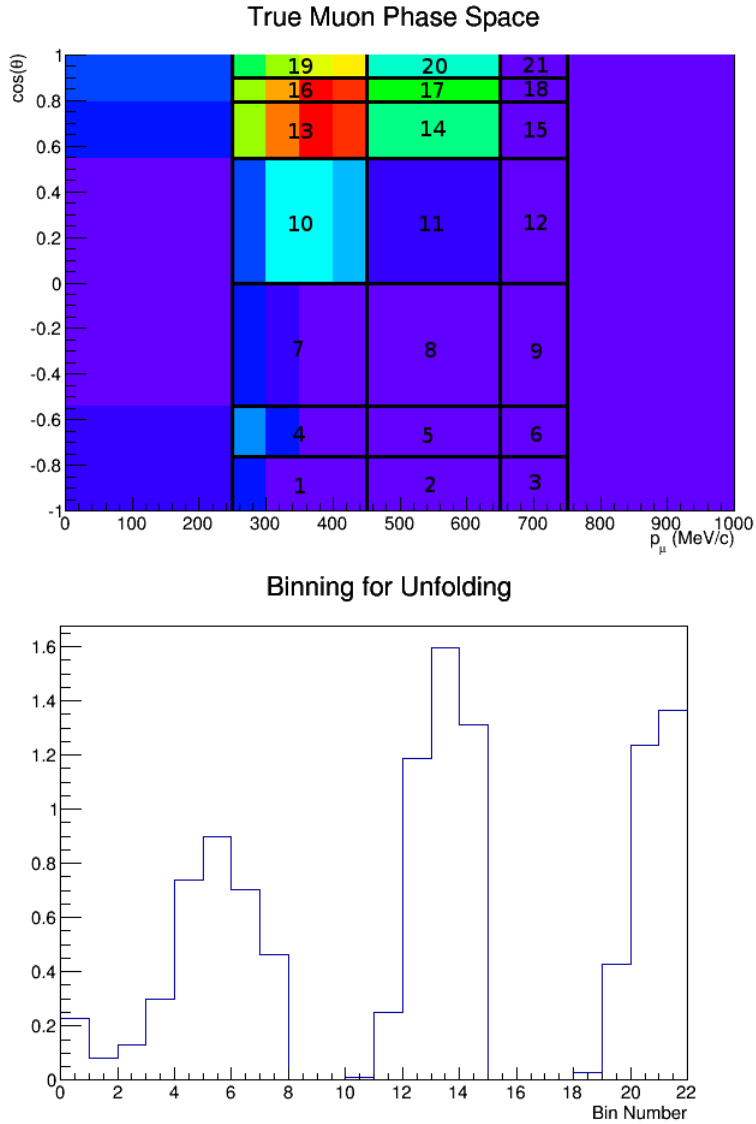


Figure 43: Schematic of the binning scheme. Each bin is a region of the two-dimensional phase space (top). The unfolded results for each bin are translated into 1-D histogram (bottom). The bins in the 650 - 750 MeV range are used for unfolding studies, but are not included in the subtraction result.

If B could be clearly distinguished from N_S , then the background subtraction would be simple: just remove those events from the selection in the first place. For the irreducible background that is present in N_T , B must be obtained from MC, which gives

$$N_S^{Obs} \simeq N_T^{Obs} - B^{mc} \quad (3.12)$$

This relation shows that for the background subtraction method, the full model dependence of the result is coming from the modeling of the background. To diminish this dependence, the background ratio can be constrained by data using a sideband sample that is mutually exclusive with the final sample. The ratio of total sideband events between MC and data can be used to normalize the total number of expected background events by the relation

$$N_S^{Obs} \propto N_T^{Obs} - (R \cdot B^{mc}) \quad (3.13)$$

where $R = S^{Obs}/S^{mc}$. The assumption here is that the physics processes generating the sideband events are the same as those in the selection background, in which case the event rates should scale equivalently for the sideband and the background. The amount of true signal events in the sideband needs to be as small as possible, to minimize correlations between R and N_S , and, by extension, with N_T ; otherwise this assumption fails.

A potential hazard with this method is clearly evident from Equation 3.3.1.1. If the MC predicts a background rate in a given bin that is higher than the number of observed events, then N_S^{obs} will be less than 0. This is a particular risk for low-statistics bins, and in the event that $R > 1$. Clearly, negative values for the cross-section are unphysical, but they must be suppressed on an *ad hoc* basis.

Purity correction uses the MC to predict the expected signal in each bin relative to the total number of events. This expectation is then applied to the measured event rate in each bin to determine the number of signal events.

$$\sigma \propto N_S^{Obs} = \rho N_T^{Obs} \quad (3.14)$$

$$\begin{aligned} \rho &= \frac{N_S}{N_T} = \frac{N_T - B}{N_T} \\ &= 1 - \frac{B}{N_T} \end{aligned} \quad (3.15)$$

where the MC labels have been dropped from ρ . In contrast to the background subtraction method, here the model dependence is introduced through the ratio of the signal to background events in the MC.

Since altering the background rate affects the overall MC event rate, both B and N_T need to be adjusted when using a sideband

$$B^{MC} \rightarrow B^{MC} \frac{S^{Obs}}{S^{MC}} \quad (3.16)$$

$$N_T^{MC} \rightarrow N_T^{MC} - \left(1 - \frac{S^{Obs}}{S^{MC}}\right) B^{MC} \quad (3.17)$$

The single largest background for this analysis is charged-current single pion production (CC-1 π , see Section 5). These are typically events in which the pion did not travel far enough through the detector to be reconstructed separately from the muon. It is possible to identify these events through the decay process $\pi^+ \rightarrow \mu^+ \bar{\nu}_\mu \rightarrow e^+ \bar{\nu}_e$, by tagging the emitted electron. However, neither Michel electron algorithm was designed to effectively detect two decays in a single event. To create a CC-1 π sideband, we are limited to selecting events with a single Michel electron

There are two major issues with this approach. The first is that a contained one track selection with a Michel electron is still predominately CC- 0π . For a sideband to be effective, the amount of signal events in the sideband must be minimal. Otherwise S^{Obs}/S^{MC} is effectively a measurement of the signal, and that measurement is then used to constrain uncertainties on the signal!

The second issue is simply statistics. Selecting out events that contain a Michel electron cut the event rate by half (see the discussion on direction criteria in Section 3.2.7). The model uncertainty of the CC-resonance cross-section normalization is $\sim 25\%$ (Table 7), and the overall uncertainty due to all interaction parameters is $\sim 5\%$ (Section 5). Reducing the signal sample size by 50% to minimize an uncertainty of 5% is not productive. For these two reasons, the selection background is addressed in the unfolding process using a purity correction without a sideband.

3.3.2 Fake Data Studies

A comparison of 1, 2, 4, and 8 iterations for the Run 2 water-in and water-out differential cross-sections and their associated errors can be found in Figure 44 and Figure 45. NEUT Run2 MC was used to develop the response matrices, with separate NEUT MC files used for fake data. The fake data has been scaled to the total water-in and water-out p.o.t for Runs 2-4. There is no improvement of any significance across all bins, while the error on the integrated cross-section nearly doubles after a single iteration.

The same plots are shown for the unfolding of Genie fake data (Figure 46 and Figure 47, again scaled to the Runs 2-4 data p.o.t.). Unsurprisingly, there is more movement from one iteration to the next for these results, since there are greater differences in the true cross-section values as well as the selected kinematics between NEUT and GENIE than there are between any two given NEUT samples. A single iteration still best recreates the true GENIE spectrum.

Bayesian unfolding with a single iteration has been the approved approach for recent

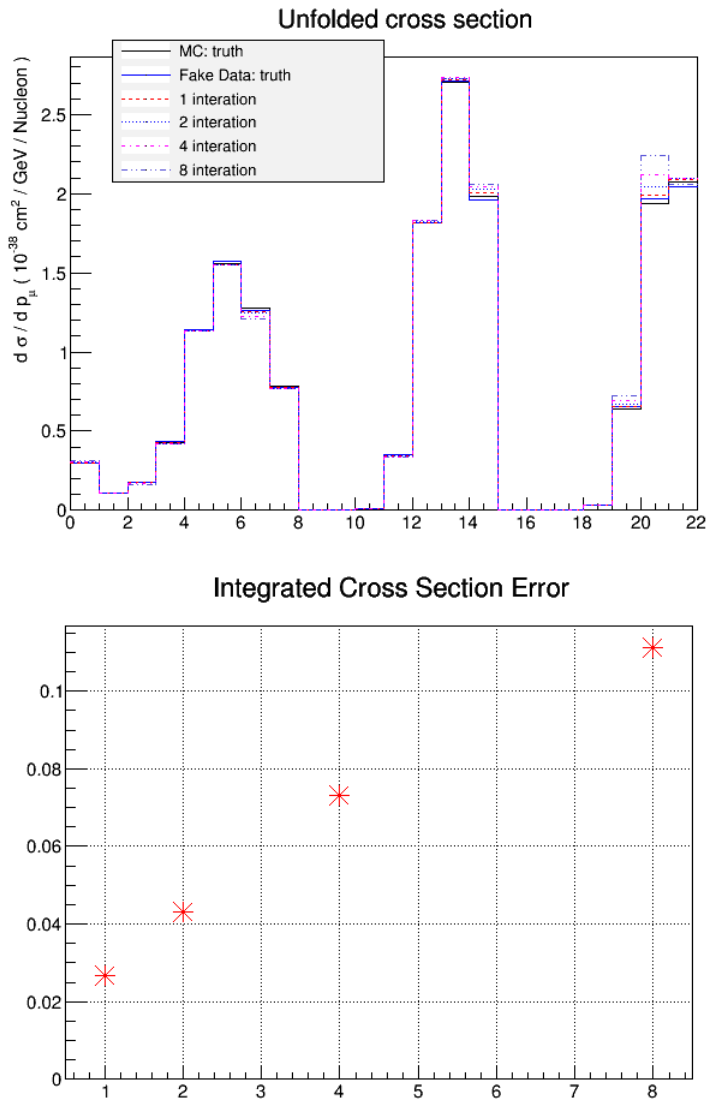


Figure 44: NEUT fake data, water-in differential cross-section by bin for 1, 2, 4, and 8 iterations (top) and the error on the total cross section (bottom). Errors are statistical.

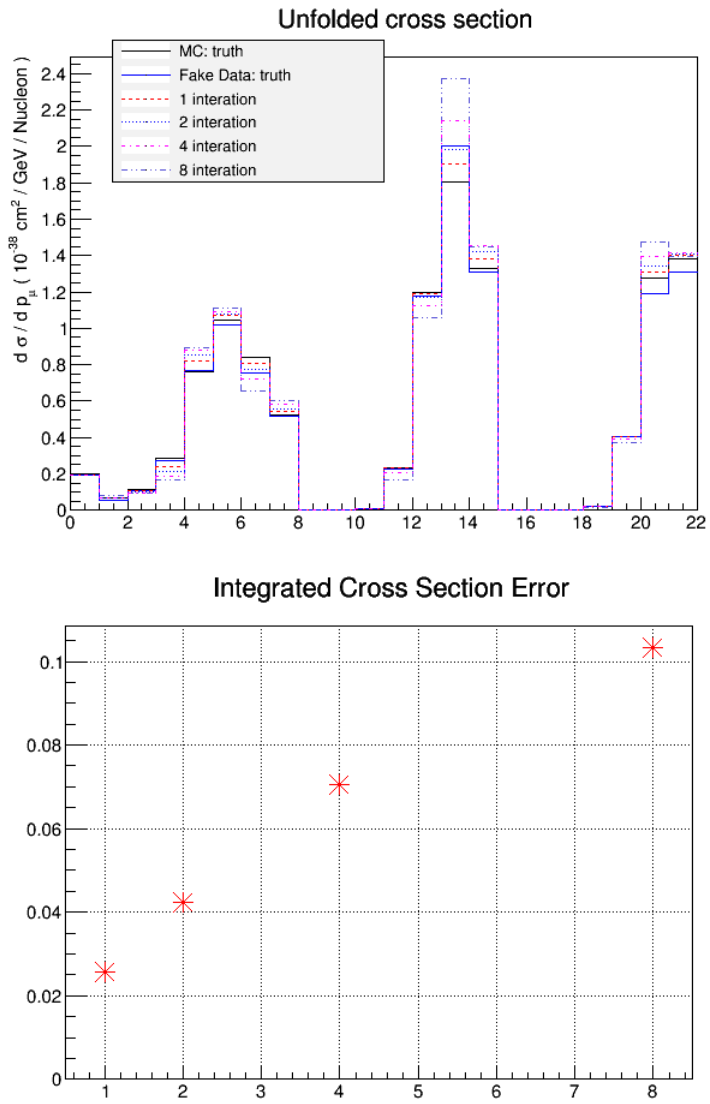


Figure 45: NEUT fake data, water-out differential cross-section by bin for 1, 2, 4, and 8 iterations (top) and the error on the total cross section (bottom). Errors are statistical.

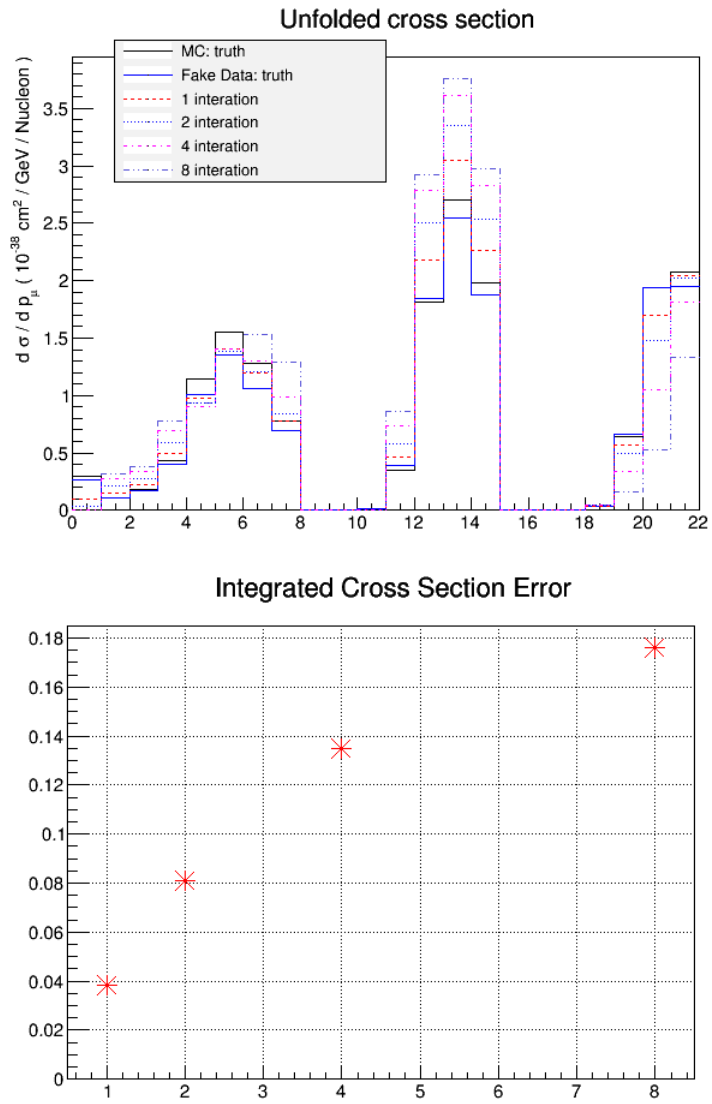


Figure 46: Genie fake data, water-in differential cross-section by bin for 1, 2, 4, and 8 iterations (top) and the error on the total cross section (bottom). Errors are statistical.

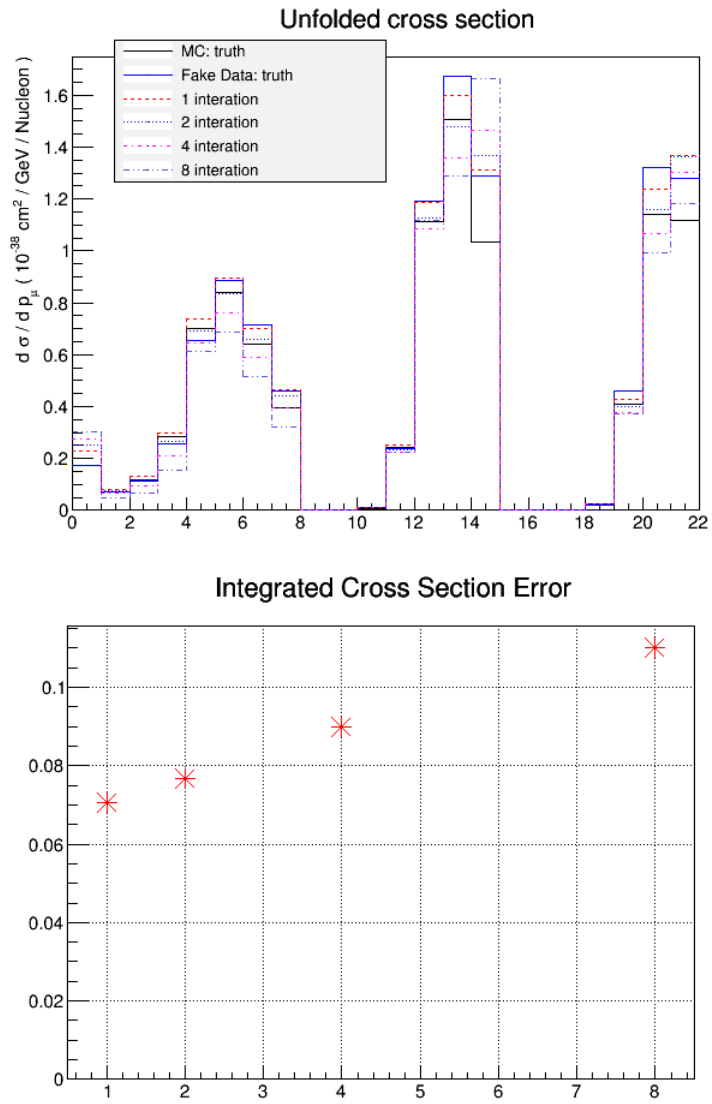


Figure 47: Genie fake data, water-out differential cross-section by bin for 1, 2, 4, and 8 iterations (top) and the error on the total cross section (bottom). Errors are statistical.

ND280 cross-section results, but there has been a growing concern over issues of convergence and bias with this method. This can be seen in the effect increasing iterations has on the GENIE fake data. While the first iteration does reproduce the GENIE truth values well, subsequent iterations drag the unfolded results further from their nominal values. Essentially, the unfolding process becomes a feedback loop where each iteration fits to the bias in the initial sample.

This behavior can be more clearly seen in a histogram of the fractional bias in each bin. The fractional bias (B) is defined as the difference between the unfolded result and the true fake data cross section

$$B^i = \frac{\sigma_{unf}^i - \sigma_{true}^i}{\sigma_{true}^i} \quad (3.18)$$

for each bin i . These plots are shown for both NEUT (Figure 48) and GENIE (Figure 49) fake data. In the NEUT plots, there is no uniform minimization of the fractional bias, but there is also no uniform increase of it either. Subsequent iterations “oscillate” around the optimum value in a given bin without a general trend of increasing or decreasing bias across all bins.

In contrast, the GENIE fake data plots do show an increase in the fractional bias with each iteration. For the few bins that do have a slight decrease in the fractional bias from 1 iteration to 2, subsequent iterations do not “oscillate” around an optimum value; they simply pull the unfolded results further away from the truth.

To test the bias from the MC generated prior, the unfolding process was studied using reweighted fake data samples. Three different reweighting schemes are used: the dominant background (CC resonance) is scaled by 50%, the CCQE production parameter (M_A^{CCQE}) is scaled by 50%, and the entire event selection is reweighted by an arbitrary formula⁶. The same sample is also used to generate the response matrix. As explained above, when the

⁶The fake data is reweighted using the MC generator interaction mode and not the final topology. CC-resonance interactions are most directly responsible for the CC-1 π background, while CCQE events generate the bulk of the CC-0 π signal, though the correspondence is not 1-to-1 and each parameter will affect both the signal and the background.

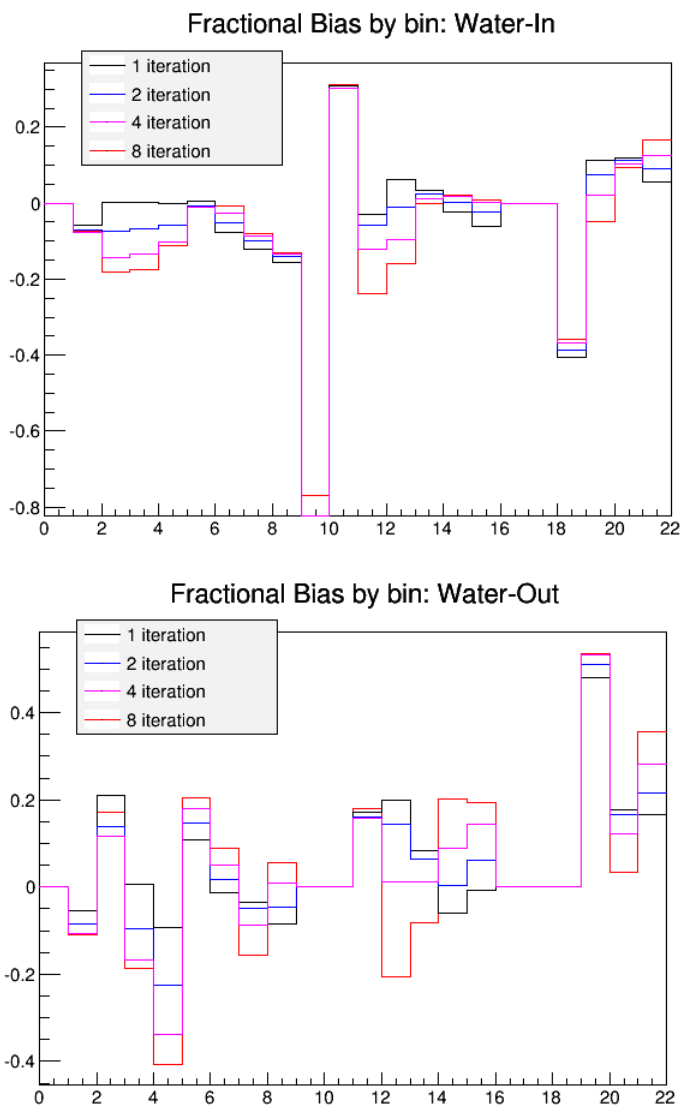


Figure 48: The NEUT fake data fractional bias by bin for 1, 2, 4, and 8 iterations. Water-in is shown on the top; water-out on the bottom.

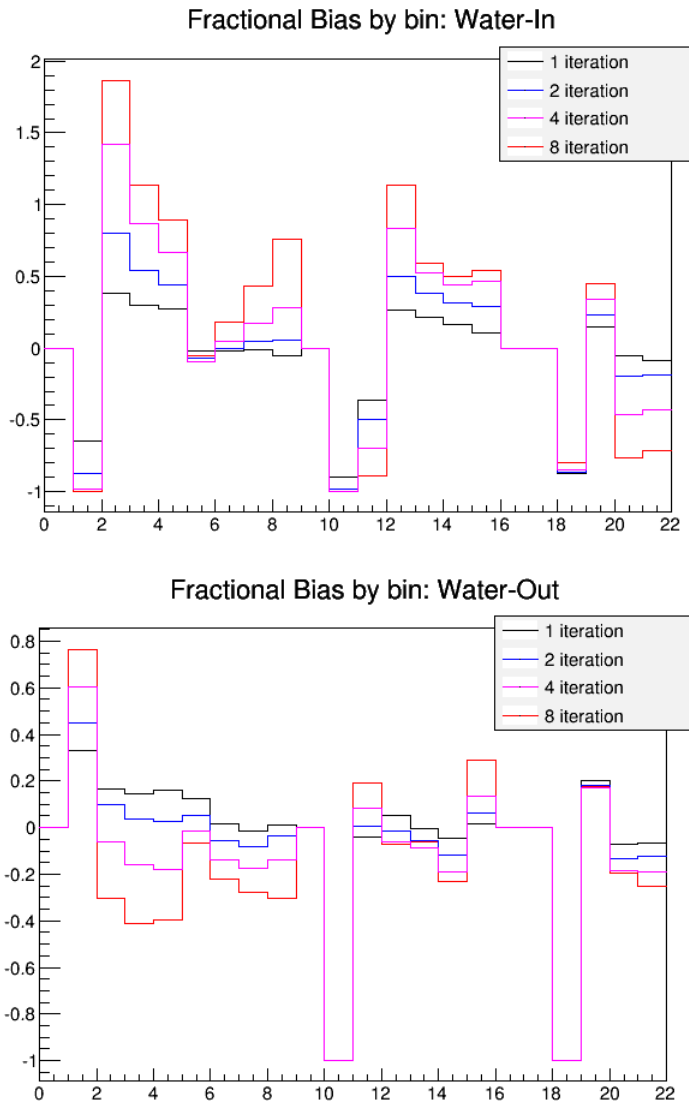


Figure 49: The GENIE fake data fractional bias by bin for 1, 2, 4, and 8 iterations. Water-in is shown on the top; water-out on the bottom

unfolding engine is passed the same sample for both the MC and fake data, the unfolded results exactly reproduce the MC truth. This approach allows for the most direct comparisons between the unweighted and weighted results.

To scale the charged-current background, any event in the fake data selection that was a true CC resonance event was reweighted by $\pm 50\%$. The CC resonance parameters are not wholly independent of the CC- 0π signal, so the true signal is shifted slightly by this reweighting (Figure 50 and Figure 51). Again there is no uniform convergence with repeated iterations and a single iteration is the preferred option.

The absolute bias by bin (the numerator from Equation 3.18) for the single iteration unfolded result is shown in Figure 52. The bias is calculated relative to both the nominal MC truth and the reweighted fake data truth. If the unfolding process was completely determined by the MC prior, it would simply recreate the nominal MC regardless of the input of the reweighted data, and the absolute bias relative to the nominal MC would be zero. Conversely, if the unfolded result did not depend on the MC prior at all, it would create the reweighted truth exactly (since it depended only on that input), and the absolute bias relative to the fake data truth would then be zero. Realistically the unfolding engine will display some intermediate behavior. While the unfolding does not reproduce the fake data truth exactly, the absolute bias relative to the fake data truth is closer to zero than that relative to the nominal MC across all bins, indicating that the unfolded result is pulled preferentially in that direction.

When the fake data is reweighted by the M_A^{CCQE} parameter, the signal is altered more substantially due to the close relationship between CCQE interactions and the CC- 0π topology detected. The unfolded results for 1, 2, 3, and 4 iterations, as well as the nominal and reweighted true values are shown for a 50% reduction (Figure 53) and for a 50% increase (Figure 54) of this parameter. The signal is raised or lowered across all regions of the phase space, though not uniformly, as M_A^{CCQE} affects the shape as well as the normalization of the CCQE cross-section.

The absolute bias for the M_A^{CCQE} reweighted fake data is shown in Figure 55. The sign

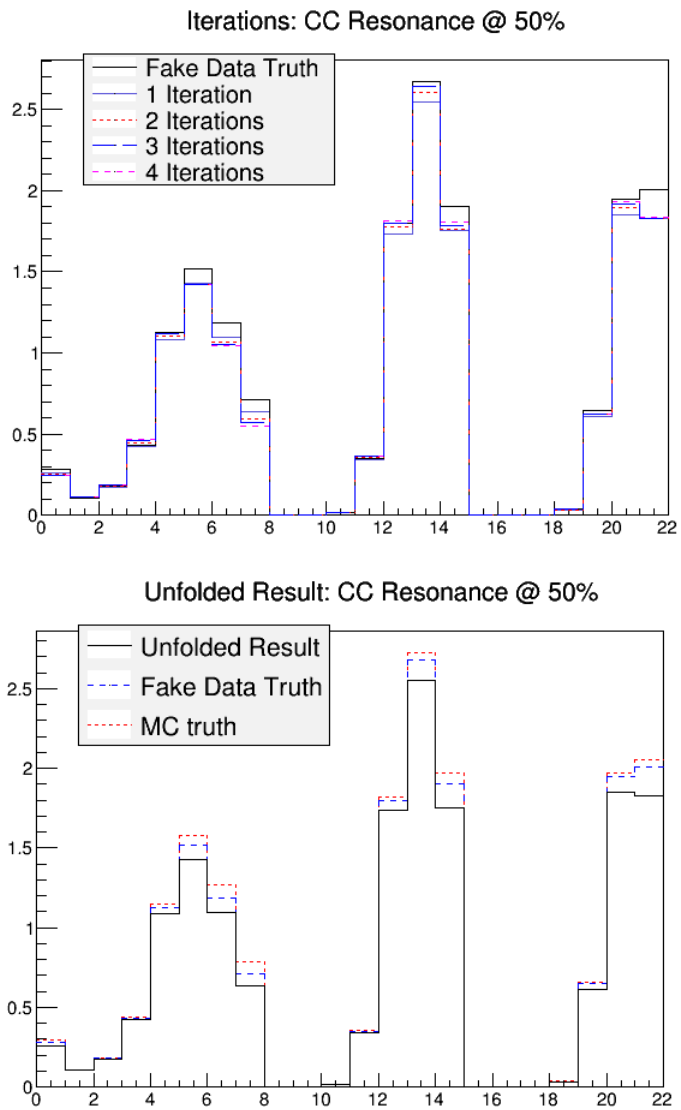


Figure 50: The unfolded cross-section for fake data with the CC-Resonance background decreased by 50% for 1, 2, 3, & 4 iterations (top) and a single iteration with the MC and fake data truth (bottom).

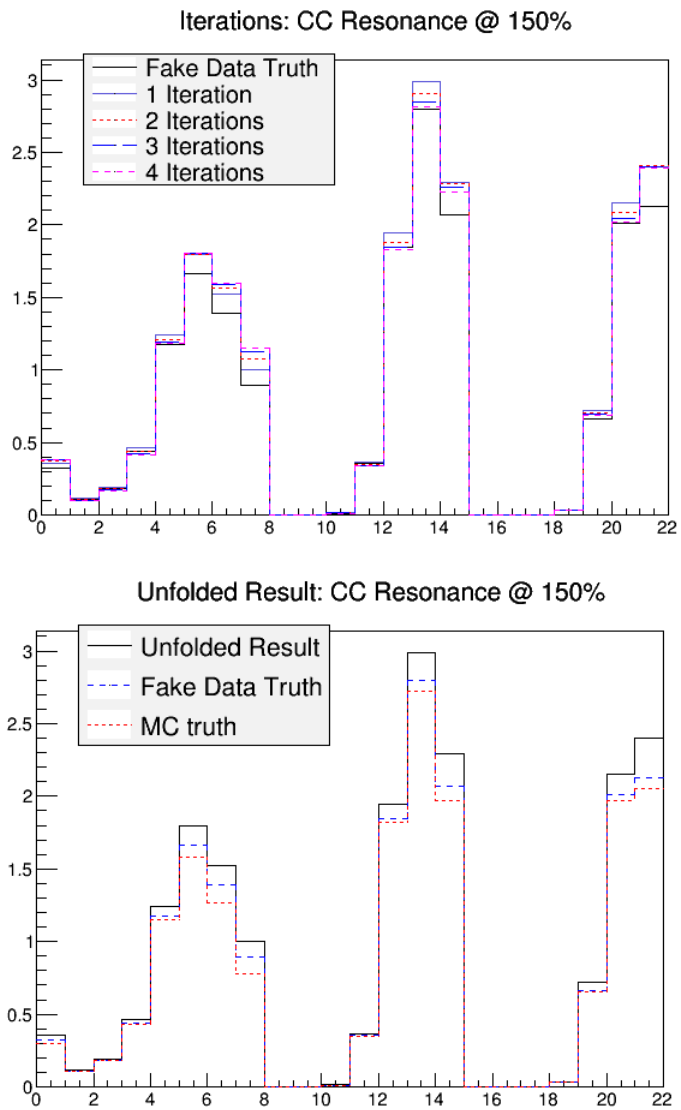


Figure 51: The unfolded cross-section for fake data with the CC-Resonance background increased by 50% for 1, 2, 3, & 4 iterations (top) and a single iteration with the MC and fake data truth (bottom).

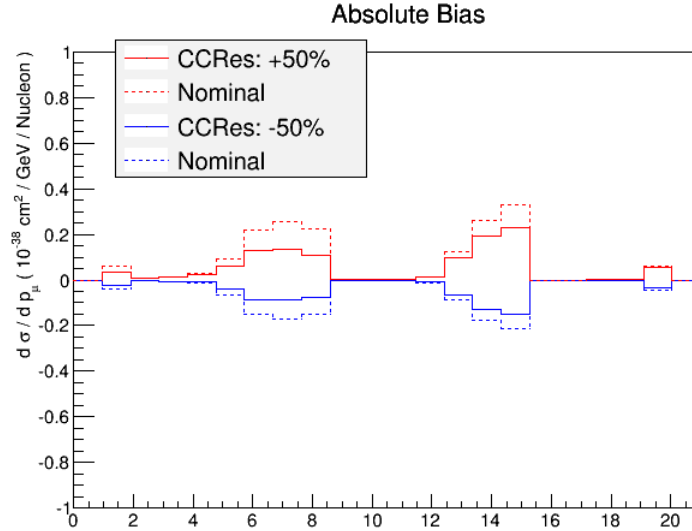


Figure 52: The absolute bias for the CC resonance reweighted fake data. The solid lines are the bias relative to the reweighted fake data truth, while the dashed lines are relative to the nominal MC.

changes between the reweighted and nominal biases, since the unfolded result lays between the nominal MC and reweighted truth. Clearly, the unfolding process is pulling the results away from the MC priors to the true signal. The absolute bias relative to the reweighted truth is also closer to zero, indicating that, while the unfolded result lays between the two, the true signal is preferred over the MC prior.

The fake data was also reweighted in a non-uniform fashion by two arbitrary formulas which scaled down the low-momentum (< 400 MeV) event rate while scaling the high-momentum rate up, and then *vice versa*. This reweighting was chosen to alter the shape of the fake data in a non-trivial way, since the unfolding process is unaffected by a uniform scaling, except for an overall normalization factor⁷. The unfolded results after 1 iteration are shown with the nominal and reweighted truth in Figure 56.

The absolute bias is shown in Figure 57. Again the unfolded result lays between the

⁷The unfolding matrix is determined by the relative event rates in bins of reconstructed and true muon kinematics. If those factors are simply scaled, the response matrix is the same but the overall event rate is changed. The unfolding process will exactly reproduce the reweighted fake data, which is the same shape as the nominal result but with a different total event rate.

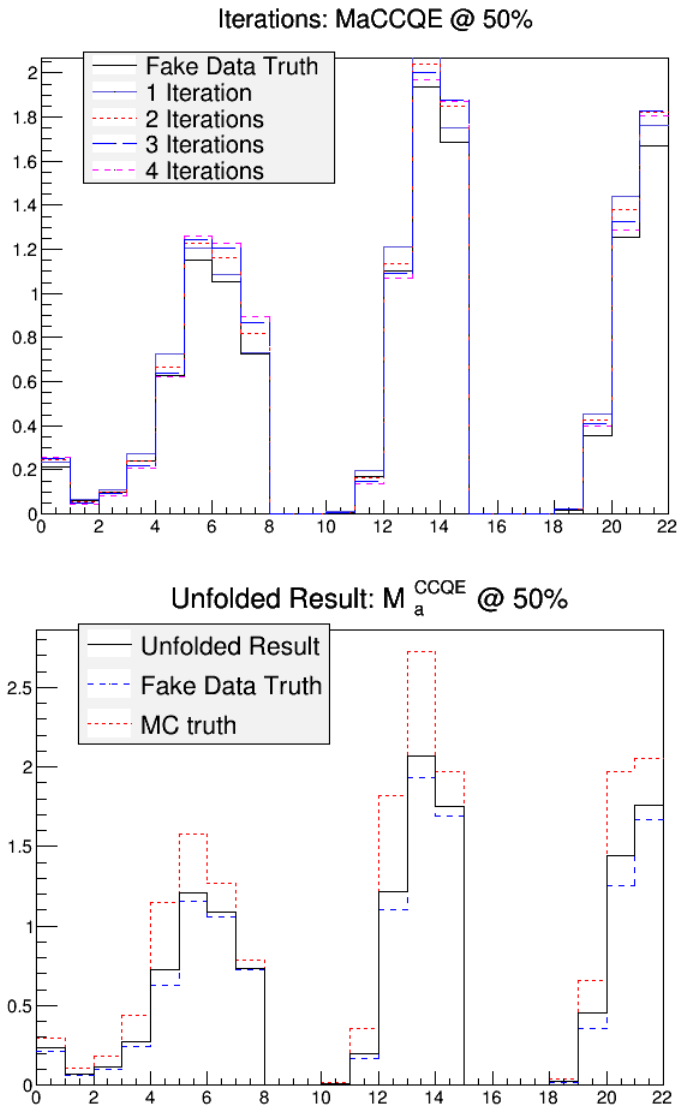


Figure 53: The unfolded cross-section for fake data with the M_A^{CCQE} parameter decreased by 50% for 1, 2, 3, & 4 iterations (top) and a single iteration with the MC and fake data truth (bottom).

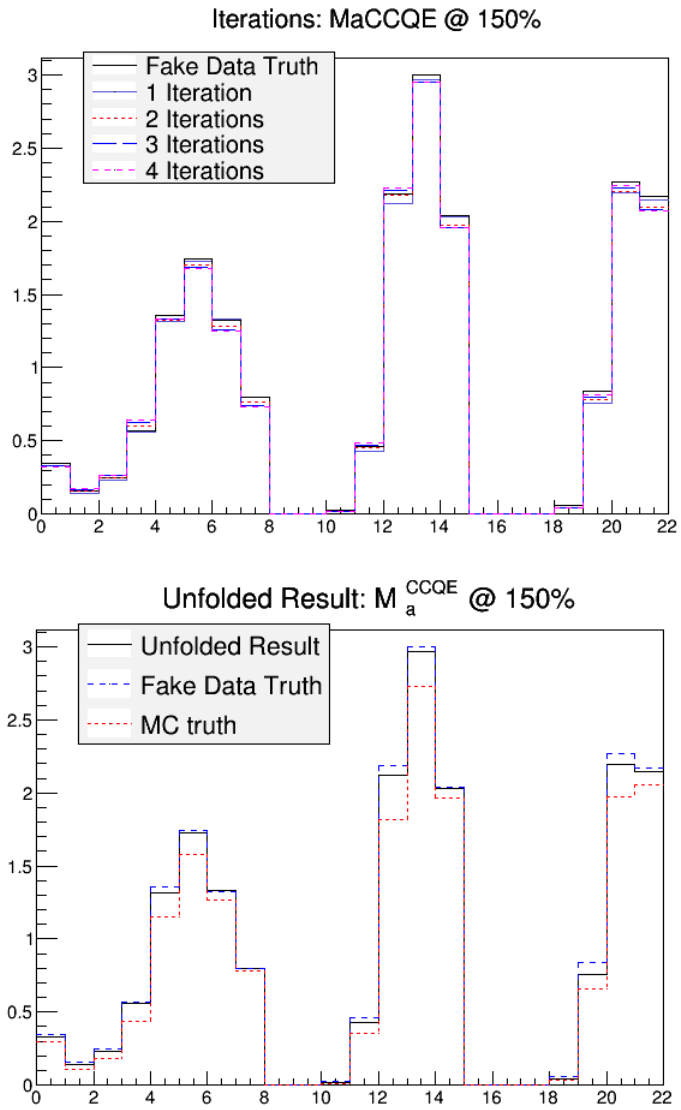


Figure 54: The unfolded cross-section for fake data with the M_A^{CCQE} parameter increased by 50% for 1, 2, 3, & 4 iterations (top) and a single iteration with the MC and fake data truth (bottom).

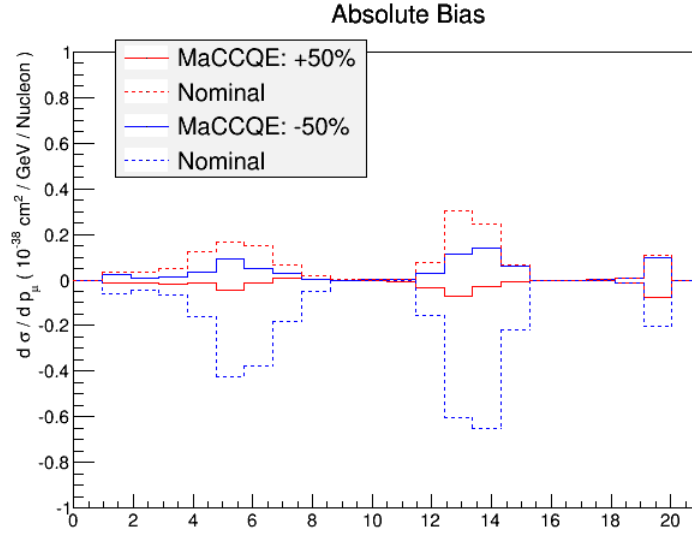


Figure 55: The absolute bias for the M_A^{CCQE} reweighted fake data. The solid lines are the bias relative to the reweighted fake data truth, while the dashed lines are relative to the nominal MC.

nominal MC and the reweighted truth. While the bias is not less for the reweighted truth across all bins, it is so for the majority of them, particularly the bins with the largest discrepancy between the nominal and reweighted MC.

Since the main goal for this analysis is to extend the accessible phase-space of the existing CC- 0π measurements on the P θ D, the decision was made to proceed with the single iteration method used for that analysis. This allows for consistency checks to be performed in areas of overlapping phase space. There are currently several possible alternatives being developed within the cross-section group, including binned-likelihood fits and improvements to the Bayesian unfolding procedure itself, but none of these approaches have been validated as of yet.

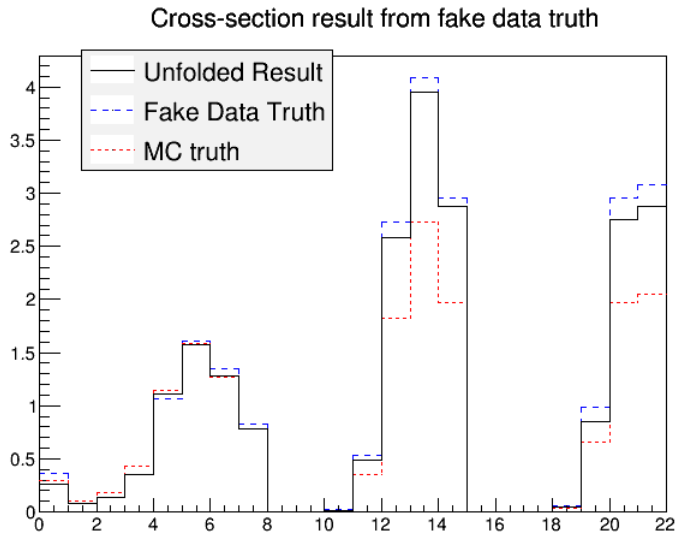
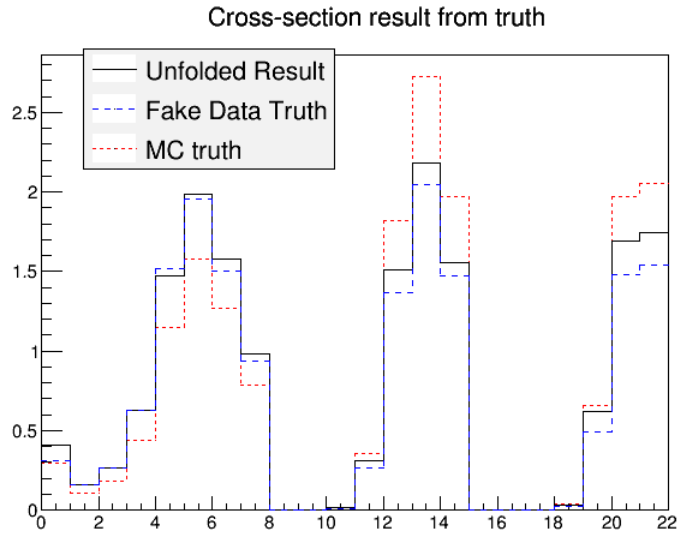


Figure 56: The unfolded cross-section for fake data reweighted by two arbitrary formulas.

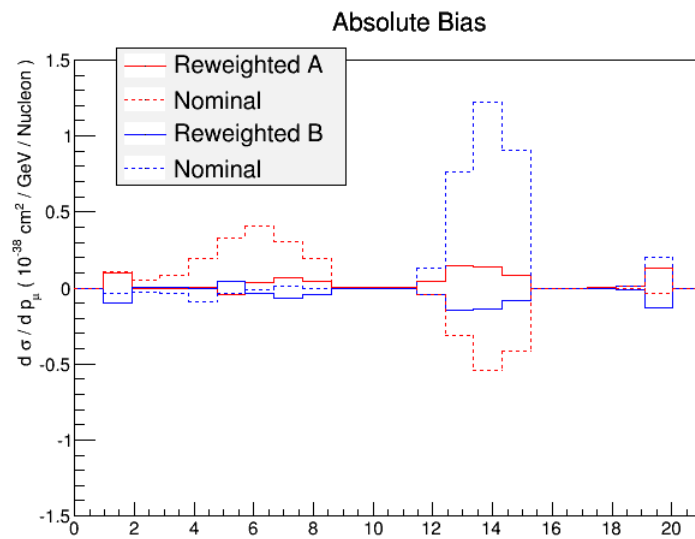


Figure 57: The absolute bias for the fake data reweighted by formula. The solid lines are the bias relative to the reweighted fake data truth, while the dashed lines are relative to the nominal MC.

4.0 SYSTEMATIC ERRORS

As described in Section 2.4.3, systematic uncertainties are propagated on an event-by-event basis, either by altering the kinematics of an event or by re-weighting the event. Weighted systematics in the Highland2 framework have two components: a systematic calculated by varying a given uncertainty, and a correction which shifts the weight of all events by some amount. There are systematics associated with each stage in the MC production process, from the beam and neutrino flux production, to neutrino-nuclear interactions, and ending with the simulation of the P \emptyset D detector response.

4.1 FLUX & INTERACTION SYSTEMATICS

There are fifty separate dials used for re-weighting: 25 for flux, 6 for FSI, 15 for cross-section parameters, and 4 for the RFG + RPA re-tuning. Each event is thrown 250 variations of each of these parameters¹, and then assigned an overall weight from the average of all throws. The parameters within each group (flux, FSI, and cross-section) are treated as correlated, while each group is uncorrelated with the others.

The flux prediction is subject to large ($O(15\%)$) uncertainties. The beam group provides updated JnuBeam files to the collaboration as new beamline/hadronic production measure-

¹Not including the RFG + RPA tuning, since these parameters are a correction to the nuclear target model rather than a physical uncertainty. As such, they are binary and the uncertainty is determined from a simple “on-off” comparison

ments further constrain these uncertainties (see Section 2.1). These files are the official predictions for the ν_μ , ν_e , $\bar{\nu}_\mu$, and $\bar{\nu}_e$ energy spectra for T2K. Differences in the neutrino spectra affect the expected p.o.t. normalized event rate, and the MC is reweighted to reflect the updated prediction. This process is done internally to T2KReWeight, and it is not altered for any individual analyses. The flux parameters used in this analysis were updated in 2015.

Interaction systematics can be split into two sources: scattering uncertainties and final state interactions (FSI). The neutrino-nucleon scattering probabilities used by NEUT depend on the integrated cross-section on each target material as well as the relative likelihood of the various interaction modes. The Neutrino Interaction Working Group (NIWG) for T2K quantifies these uncertainties using the most current theory and data, both with and without ND280 data (referred to as “postfit” and “prefit”, respectively: the postfit parameters are used for oscillation analyses, while the prefit values are used for ND280 cross-section measurements). Due to the similarities in the relevant neutrino energies and the range of acceptance, MiniBooNE is the main source for T2K’s external data fits[55].

Two NC-elastic parameters are varied in addition to the uncertainties provided by the NIWG: one that determines the shape of the NCE cross-section as a function of E_ν , and one that determines the overall normalization of NCE events. The NIWG is primarily focused on reducing uncertainties that affect the T2K oscillation results, which are predominately charged-current and pion-producing interaction modes. Single proton events are negligible for these analyses, and no neutral current elastic uncertainties are included.

The effect of these two parameters are calculated independently of the other cross-section uncertainties. A MC fake-data study is thrown $\pm 1\sigma$ variations around the NEUT nominal value for both the shape and normalization. The uncertainty on the selection generated from this study is then included with the other cross-section uncertainties in the unfolding engine.

Six final state interaction parameters in NEUT govern the interaction rates of pions as they traverse the interaction nucleon. The nominal values used were determined by fitting 24 sets of these parameters against external π -C scattering data (mostly from MiniBooNE).

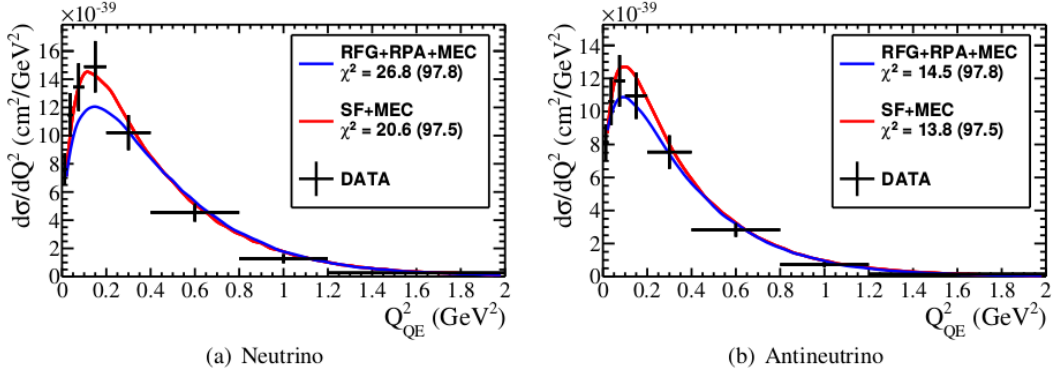


Figure 58: Comparison of the spectral function and RFG + RPA models for neutrino and anti-neutrino QE events[56]

The variances were extracted from 16 points on the 6 dimensional $1\text{-}\sigma$ space. Re-running the NEUT simulation with these parameters altered is too computationally intensive to be practical on an ad-hoc basis. Instead, a sample of reprocessed NEUT files were generated by the NIWG, and the ratio of the new to nominal cross-sections are used to weight the MC.

In addition to these uncertainties, the NIWG recommends re-tuning the NEUT MC nuclear target model. As detailed in Section 2.4.1, the momentum of the target nuclei is obtained from a derived spectral function, which is known to be incomplete. An alternative model treats the nuclei as a relativistic Fermi gas (RFG) with a random phase approximation (RPA), which accounts for inter-nucleon correlations. While the spectral function supplies a more accurate model for the intra-nucleus target momenta, there is currently no model which combines it with the RPA. Both models are incomplete, and there are significant differences between the CCQE axial masses found when fitting data using each[56]. The discrepancy between these two models is then treated as an additional uncertainty in T2KReWeight.

MINER ν A recently published a measurement identifying two separate nuclear effects in ν_μ -O interactions; a low-energy long-range nuclear screening effect, and an excess in the quasielastic- $\Delta(1232)$ resonance region associated with MEC events [57]. However, this MEC measurement is not anticipated to substantially affect these results. The MINER ν A beam energy peaks at 3.5 GeV and only muons with $E_\mu > 1.5$ GeV are accepted for this

study. Both factors are firmly outside of the kinematic region of interest. The authors of the MINER ν A paper point out that this MEC signal occurs in the region between the quasielastic and $\Delta(1232)$ regions of the E_ν spectrum, while this analysis is focused on a region that is dominated by the QE mode. This can be clearly seen in the topology breakdown of the final selection in Table 6.

The T2K cross-section analysis group’s approach to MEC systematics is to assign at 100% uncertainty on the MEC models used in the MC generators, and this analysis follows that approach. While MEC effects are not expected to be significant for the reasons given above, this is still a very new and active area of research, and a conservative approach is best.

Whereas the other parameters listed are solely dependent on the particular target nuclei, meson exchange currents are possible between oxygen and carbon atoms, and a correlation term is included.

The cross-section parameters most pertinent to this analysis are listed in Table 7. The axial mass is used as a proxy for all sources of the CCQE shape uncertainty, which is why the σ listed is larger than the discrepancies between current M_A^{CCQE} measurements.

4.2 DETECTOR SYSTEMATICS

The water subtracted cross-section is calculated by measuring the CC-0 π event rate in bins of p_μ and $\cos(\theta)$, and it is necessary to quantify how the detector response affects these quantities. Some factors affect the selected event rate within a single bin, while others can cause particular events to migrate between the bins. The detector effects that have the greatest impact on this analysis are listed below.

- P \emptyset D Mass
- Out of Fiducial Volume (OOFV)

Table 7: The T2KReWeight CC-0 π relevant cross-section systematic parameters and their uncertainties

Parameter	Target	Mean	σ
M_A^{CCQE} (MeV/c ²)	All	1.2	0.41
Fermi Momentum (p_F)	C	217	0.31
MeV/c	O	225	0.31
Binding Energy (E_B)	C	25	9
MeV	O	27	9
MEC Normalization	C	1.0 [†]	1.0
	O	1.0 [†]	1.0
CC Resonance Norm.	All	1.01	0.25
1- π form factor (GeV)	All	0.95	0.15
NCE M_A^{QE} shape	All	1.0	0.33
NCE M_A^{QE} Norm.	All	1.0	0.33
[†] O and C values are correlated. Off-diagonal term = 0.09			

- Angular Resolution
- Backward Track Selection
- Particle ID Pull
- P \emptyset D Energy Scale

All systematics are propagated on an event-by-event basis as detailed in Section 2.4.3. While the effect of each systematic can be calculated independently, the total cumulative uncertainty is obtained by varying each simultaneously to handle correlations directly. This is particularly important as several of these systematics have a strong track length dependency.

4.2.1 P \emptyset D Mass

Mass uncertainties for the material in the FV affect the expected number of CC-0 π events. Each event is reweighted by $w_m = m + \sigma_m x_{var}$, where m is a correction to the MC material mass, σ_m is the uncertainty on that mass, and x_{var} is a normally distributed variable thrown for systematic propagation. The material used for each event is found from the position of the true interaction vertex.

There are five sources of consequence for this systematic: the brass supports between the water bags, the lead between the P \emptyset Dules, dead material in the P \emptyset D (in particular, the tubing and electronics for the water-sensors), the carbon of the scintillator, and the oxygen from the water (when filled). The water sensors are not modeled in the MC, so a correction term is required to account for their mass. However, since the sensors are not present in the MC geometry, the position of the true vertex cannot be used. To address this, the uncertainties for the tubing and electronics for the water-sensors are combined with those for the brass, as the affect of each on the water-subtraction measurement is similar. This approach has been used in other P \emptyset D measurements[53].

There are known discrepancies between the modeled materials of the P \emptyset D and the P \emptyset D as it actually built, and the correction m is simply the ratio of these two values for a given material. The uncertainty σ_m is obtained from the uncertainty of physical measurements

Table 8: MC mass correction terms and their uncertainties[52]

Material	m	σ_m
Lead	0.9988	0.0218
Copper	1.1448	0.0332
Oxygen	0.9868	0.0084
Carbon	0.9988	0.0093

of the completed PØD. The values used are from [52] and can be found in Table.8. All corrections are very near to unity, with the exception of copper for the reasons explained above.

The errors on the mass calculations of all the materials are fully correlated, with the exception of the oxygen. Since the measurement of the water mass is made from comparisons between the water-in and water-out modes, it is independent from the overall mass of the PØD.

4.2.2 Out of Fiducial Volume

Out of fiducial volume (OOFV) events are ones in which the true interaction vertex is outside of the defined FV but are reconstructed as originating within the FV. While some of these events are misidentified due to reconstruction factors, such as the spatial resolution of the PØD scintillator or the Δ_t efficiency, there will always be an unavoidable OOFV background. Due to the geometry of the PØD, the true neutrino vertex can occur in dead material outside the FV, the particle then travels into the FV, and then the first interaction with the active scintillator occurs within the FV.

The overall OOFV rate is 6.4% (9.1%) for water-in (water-out) running, and the total contamination rate from events outside the PØD is 0.8% (2.3%). The higher out-of-PØD

Table 9: OOFV rates with statistical uncertainties for NEUT Production 6B Water-In & Water-Out modes.

Detector	Water-In (%)	Water-Out (%)
Tracker	< 1	< 1
DsECal	< 1	< 1
BrECal	< 1	1.3 (1.0)
P0DECal	5.2 (0.15)	11.2 (0.15)
P0D	87.0 (0.04)	69.1 (0.05)
SMRD	7.4 (0.12)	17.5 (0.10)

rate for water-out running is attributed to the absence of the stopping power of the water in the area surrounding the FV. In other words, there is less dead material to stop exterior particles from entering the P0D active region.

The errors in Table 9 are purely statistical. As described in Section 3.2.5, this analysis uses a common definition for the FV as other P0D results. In order to determine what effect that definition has on the OOFV rates, the boundaries of the FV in X and Y were varied by the position reconstruction resolution, $\sigma_{pos} = 32$ mm, while the Z parameters were not altered, as those are constrained by the geometry of the P0D water target. The relative OOFV rates for $XY \pm 1 \sigma_{pos}$ are equivalent to Table.9 within statistical errors, and no additional uncertainty associated with the particular position of the FV is applied.

The OOFV systematic uncertainty is applied as a weight to each event, where the weight is calculated by

$$w = 1 + \sigma_{Det} x_{var} \tag{4.1}$$

The parameter σ_{Det} is the uncertainty listed in Table 9 determined by the true origin of the OOFV event, and x_{var} is a normally distributed variable thrown for systematic

propagation. The nominal event weight $w = 1$ is unchanged for all FV events.

The reconstructed position of the interaction vertex can be smeared by the recoil of the target nucleus. Interactions that occur very near the boundary of the FV can be misidentified as being within it due to this effect. Previous studies in the PØD have indicated that this effect is under represented in the MC by a factor of 2[53]. To account for this discrepancy, an additional uncertainty is applied to OOFV events which originate in either the USECal or CECal. This weight is calculated by

$$w_{corr} = \mu + \sigma_{\mu} x_{var} \tag{4.2}$$

where $\mu = 2$ is the correction to the MC and $\sigma_{\mu} = 0.5$ is the corresponding uncertainty on that correction. The value of σ_{μ} is chosen such that $w_{corr} = 1$ is not excluded. These events account for 12.4% (10.4%) of the water-in (water-out) OOFV rate, which is 0.8% (0.9%) of the total event selection. Since this background originates in the ECals on either end of the water-target, it is independent of the PØD water status, and its affect on the water-subtraction measurement is minimal.

4.2.3 Angular Resolution

The muon angle θ is defined as the polar angle off of the axis defined by the path of the incoming neutrino. Since the ND280 detector is located in close proximity to the beamline, it is inaccurate to characterize the flux as coming from a point source. In MC, this axis can be found directly from the truth information used by the neutrino generators; for data, it is calculated using the reconstructed vertex position.

There are two independent systematics that affect what θ bin a muon will be placed into: the direction of the muon as determined by Δ_{time} , and the direction of the track in the PØD reconstruction. The first is addressed below (Section 4.2.4). The second can also be thought of as the “slope” of the track. The PØD reconstruction assigns a unit vector in the direction

traveled by the track in terms of the PØD XYZ axes, and the angular resolution systematic seeks to quantify the uncertainty on this vector.

Previous studies have shown that that the differences in the angular reconstruction between data and MC are negligible in the PØD, and the particle gun samples detailed in Section 3.2.6 are used here as well.

A systematic study on the slope of the PØD track does not require calculating θ , so the polar angle from the Z-axis of the PØD, α_Z , can be used instead². As can be seen in Figure 59, the reconstruction resolution for α_Z is virtually identical to that for $\cos(\theta)$.

For each selected event, α_Z is transformed to α'_Z by the relation

$$\alpha'_Z = \alpha_Z(1 + \delta_\alpha + \sigma_\alpha x_{var}) \quad (4.3)$$

where δ_α is the mean offset between the true and reconstructed α_Z , σ_α is a Gaussian uncertainty, and x_{var} is a normally distributed variable thrown for systematic propagation. For water-in (water-out), the value used for δ_α is -0.0037 (-0.0047), while σ_α is 0.048 (0.054).

4.2.4 Backward Track Selection

The backward track selection systematic is calculated by reweighting the number of backward-going tracks selected relative to the total number of selected tracks. There are several factors that enter into this calculation: the efficiency of correctly determining the direction of both forward and backward-going tracks, the agreement of Δ_{time} between data and MC, and the ratio, R^T , of the true number of backward-going tracks selected to the total number of tracks in both data and MC.

The total number of tracks determined to be backward-going (N_{back}) is a function of

²What is being studied here is the effect the uncertainty of the detector quantity that is the track's slope has for the final calculation of θ . This uncertainty at the detector level is propagated through the selection to determine its ultimate effect on $\cos(\theta)$

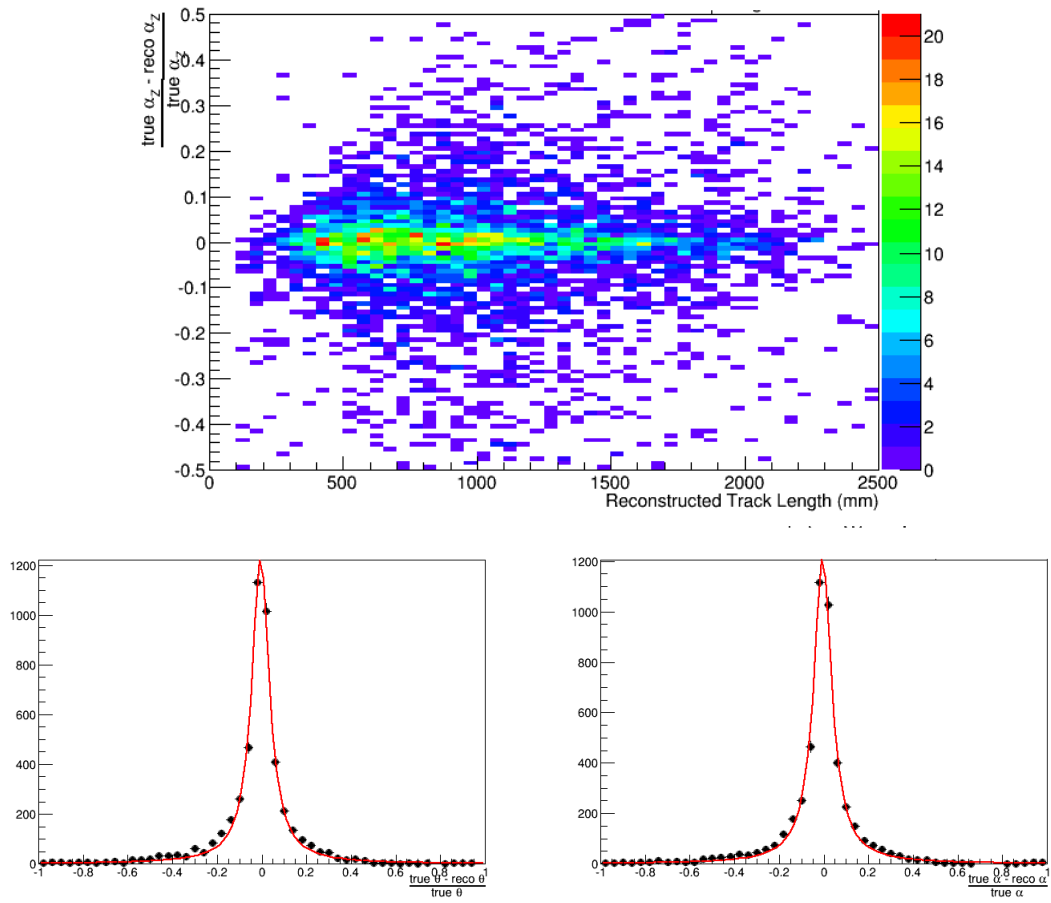


Figure 59: The angular resolution for α_Z vs reconstructed track length (top), and the overall resolution for both $\cos\theta$ (bottom left) and α_Z (bottom right) for the water-in particle gun study. These plots are also indicative of the water-out sample.

the efficiency of correctly selecting a backward-going track (ϵ_b), the false positive rate of forward-going tracks passing the selection (ϵ_f), and R^T , which can be written as

$$N_{back} = [\epsilon_b R^T + \epsilon_f (1 - R^T)] N_{tot} \quad (4.4)$$

Relying on an R^T from MC should generally be avoided, as that quantity will depend on the model used to generate the event³. In this case, the model dependence on this uncertainty can be reduced by introducing a non model-dependent correction term. Using R^T for data to do so would be ideal, though it is not something that can be known *a priori*. However, it can be extrapolated by the ansatz⁴

$$R_D^T = R_{MC}^T \frac{R_D^S}{R_{MC}^S} \quad (4.5)$$

where R_D^S and R_{MC}^S are the ratio of the number of selected backward tracks to the total number for data and MC, respectively. Combining Equation 4.4 and Equation 4.5, we can derive the expected selected ratio in data.

$$R_D^S = R_{MC}^S \frac{R_D^T}{R_{MC}^T} \quad (4.6)$$

$$= [\epsilon_b R_{MC}^T + \epsilon_f (1 - R_{MC}^T)] \left(\frac{R_D^T}{R_{MC}^T} \right) \quad (4.7)$$

$$= [\epsilon_b R_{MC}^T + \epsilon_f (1 - R_{MC}^T)] \left(\frac{R_D^S}{R_{MC}^S} \right)^\dagger \quad (4.8)$$

This final step introduces the quantity $\left(\frac{R_D^S}{R_{MC}^S} \right)^\dagger$, which is the measured ratio between R_D^S and R_{MC}^S in the final selection. In this way, an expected selection rate can be calculated with the model-dependent R_{MC}^T , which is then adjusted as the data dictates. This definition does require the data to be unblinded before the full effect of the systematic can be finalized.

³Which would not be an issue *if* our models were correct. Needless to say, this is not the case.

⁴The assumption behind this proposal is that the relationship between the selected sample and the true sample is roughly equivalent for both data and MC.

Table 10: The values used for calculating the Δ_{time} systematic weights detailed in Equation 4.9 & Equation 4.10. For R_{MC}^S , the values given are for NEUT MC, with GENIE in parentheses.

	ϵ_b	σ_b	ϵ_f	σ_f	R_D^S	R_{MC}^S	R_{MC}^T
Water-In	0.92	0.03	0.03	0.01	0.16	0.11 (0.11)	0.10
Water-Out	0.95	0.03	0.02	0.01	0.21	0.17 (0.16)	0.15

However, so long as the only change made after opening the data is to update the value of $\left(\frac{R_D^S}{R_{MC}^S}\right)^\dagger$, this analysis is not biased by this method.

The efficiency of Δ_{time} is 100% for tracks > 1000 mm. There is no need, then, to propagate this systematic for events in which the selected muon travels more than 1 m. However, events of all track lengths are corrected by $\left(\frac{R_D^S}{R_{MC}^S}\right)^\dagger$. The backward track selection systematic is propagated according to Equation 4.9, and the correction term is given in Equation 4.10.

$$w_{syst} = \begin{cases} 1 + [\sigma_b \epsilon_b R_{MC}^T x_b + \sigma_f \epsilon_f (1 - R_{MC}^T) x_f] \left(\frac{R_D^S}{R_{MC}^S}\right)^\dagger & \text{for } l \leq 1000 \text{ mm} \\ 1 & \text{for } l > 1000 \text{ mm} \end{cases} \quad (4.9)$$

$$w_{corr} = \left(\frac{R_D^S}{R_{MC}^S}\right)^\dagger \quad (4.10)$$

Here σ_b (σ_f) is the Gaussian uncertainty of ϵ_b (ϵ_f), and x_b and x_f are the independent normally distributed variables thrown for systematic propagation for ϵ_b and ϵ_f , respectively. The values used for these quantities can be found in Table.10.

4.2.5 Particle ID Pull

Sand muons provide an independent control sample to ascertain differences in detector response between data and MC, and the parameters used to calculate the Pull PID are derived from these samples (Section 3.2.8). These samples are used to extract the most

probable value (MPV) and statistical variation for the muon energy loss in each node, which can then be used to calculate the variance of the PID pull due to fluctuations in the measured energy.

As detailed in Sect. 3.2.8, the PID pull is calculated by

$$Pull = \sum_{node, n=0}^{node, n=N} \frac{Q_{meas} - \hat{Q}_{exp, n}}{\sigma_{exp, n}} \quad (3.3 \text{ reprinted})$$

There is some variance in the pull from each bin due to statistical fluctuations in the energy deposited by a particle in the PØD. These variations are independent of each other from node to node for a given particle. For a muon to have a correlated node-to-node energy loss different from the expected profile would require either (a) that the muon was in a different part of the Bethe-Bloch curve than expected, or (b) that the energy loss for that particular muon differs from the norm for some reason. Since the pull calculation uses bins in the MIP region of the muon (distance $\gtrsim 400$ mm; Figure 33), the expected energy loss profile at the end of the track is consistent for each particle, which accounts for (a). Barring sudden changes in either the PØD detector response or the identical nature of all muons, we can assume that (b) does not apply.

The overall uncertainty due to the PID pull can be found by passing 250,000 “toy experiments” to the calculation. A “measured” node energy, Q_{meas} , is passed to Equation 3.3. This energy is generated from the most probable value for the energy loss in that bin from sand muon MC, and then varied by the MC uncertainty. Each bin is varied independently for each toy experiment. The expected energy in the node and its uncertainty for each bin are parameters obtained from sand muon data ($\hat{Q}_{exp, n}$, and $\sigma_{exp, n}$, respectively). The pull is calculated for each toy experiment, and then histogrammed and fitted to a Gaussian distribution (Figure 60).

Variations of the pull value do not affect the reconstructed kinematics of the event, but they do affect whether a given event passes the selection criteria. For this reason, the pull systematic is propagated as a weight on the event, with a value of either 1 or 0. The pull

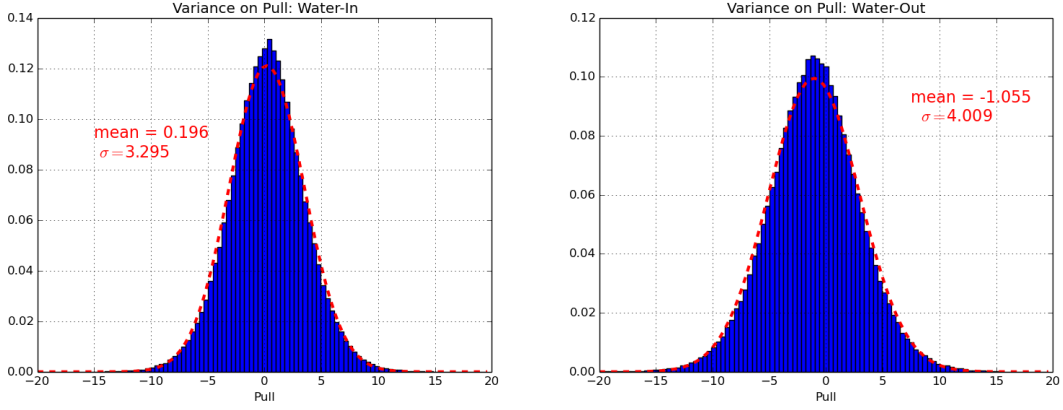


Figure 60: The variance of the PID pull variable for water-in (left) and water-out (right) running.

is varied by the mean offset (δ_{Pull}) and the Gaussian uncertainty (σ_{Pull}) found from the toy experiments described above. The event is then reweighted either to 1 if the event would pass the Pull cut with the varied value, or to 0 if it would not.

$$Pull' = Pull (1 + \delta_{Pull} + \sigma_{Pull} x_{var}) \quad (4.11)$$

$$w_{Pull} = \begin{cases} 0 & \text{for } Pull' \geq 20 \\ 1 & \text{for } Pull' < 20 \end{cases} \quad (4.12)$$

4.2.6 P \emptyset D Energy Scale

The MC-modeled detector response can differ from the real MPPCs, which can affect the reconstructed kinematics. If the energy scale is shifted, the MC muon momentum can be systematically offset from that of a real muon traveling through the P \emptyset D. Differences in energy scales could also, in principle, affect whether or not a hit in the scintillator is actually reconstructed. This topic is included for completeness, however, these issues are considered negligible for this analysis.

Table 11: ADC values for water-in and water-out mode for each bin. The binning scheme is detailed in Section 3.2.8.

Bin	Water-IN			Water-OUT		
	Data	MC	Data/MC	Data	MC	Data/MC
1	89.0	90.3	0.99	102.0	106.8	0.96
2	67.3	66.5	1.01	78.0	78.9	0.99
3	57.1	57.7	0.99	65.0	65.7	0.99
4	52.6	53.4	0.99	59.4	59.2	1.00
5	51.2	50.7	1.01	56.7	55.5	1.02
6	49.0	49.0	1.00	53.3	53.2	1.00
Average			1.00			0.99

The sand muon MC and data samples used for the PID can also be used to study the energy scale. The average energy deposited in the detector as a function of distance from the end of the track is compiled for both data and MC and then compared (for more detail on sand muon samples or the binning criteria, see Section 3.2.8). The six bins used cover both the MIP region of the p_μ phase-space and the region of higher momentum loss at the very end of the tracks. The average energy deposited by bin for each sample is given in Table 11.

The average sand muon energy deposition shows very good agreement between data and MC, with an average data/MC ratio for water-in (water-out) mode of 1.00 (0.99). Any systematic differences between MC and data are well within the spread of the reconstructed momentum resolution in the P \emptyset D. This systematic is not propagated with the other detector uncertainties.

4.3 TOTAL SYSTEMATIC UNCERTAINTY

The total systematic uncertainty from each source in each bin is shown below. Each histogram is a single bin in $\cos(\theta)$ plotted against the muon momentum. The total systematic uncertainty is found from adding the uncertainty from each source in quadrature.

The errors for the on-water calculation are not simply the sum of the errors from the water-in and water-out selections, since the on-water cross-section is calculated by subtracting one from the other and the errors between the two selections are correlated. Due to differences in the acceptance of each selection, there is not a perfect cancellation of shared detector systematics. The acceptance of various background interactions modes are also different between water-in and water-out. All of which makes the interplay of the systematics from each source on the final on-water measurement far from straight-forward.

The unfolding engine accounts for these correlations. The total error is calculated by measuring the uncertainty from each source on the unfolded result in each bin, and then adding each source in quadrature, and this is done for each selection independently, and then again for the subtracted result. No assumptions are made about the cancellation of any sources of error, or about any correlations.

A breakdown of the contribution of each error group on the total cross-section can be seen in Table 12, where an error group is a collection of error sources that have been propagated together. For example, all the individual detector systematics were propagated at the same time to account for correlations between error sources, and thus the error for the entire group of detector systematics is reported.

The single largest contribution to the total uncertainty is the flux, which is expected. The detector uncertainties are larger for the on-water cross-section than for either water-in or water-out. This is the only group for which that is the case, and it is due to the difference in acceptance between the water-in and water-out modes.

Table 12: The contribution to the uncertainty on the total cross-section by error source as a percentage of the total cross-section.

Group	Water-In	Water-Out	On-Water
Detector	0.0243 (3.1%)	0.0216 (3.5%)	0.0157 (4.7%)
Flux	0.0736 (9.3%)	0.0575 (9.4%)	0.0312 (9.2%)
Interaction	0.0247 (3.1%)	0.0256 (4.2%)	0.0089 (2.7%)
FSI	0.0220 (2.8%)	0.0219 (3.6%)	0.0069 (2.1%)
All Syst.	0.0741 (10.7%)	0.0701 (11.5%)	0.0367 (10.9%)
Statistics	0.0089 (1.1%)	0.0091 (1.5%)	0.0111 (3.3%)

5.0 RESULTS

5.1 FAKE DATA

The double differential cross-section results for water-in, water-out, and on-water are shown below. All plots are generated with NEUT MC and GENIE fake data, scaled to Run 2-4 p.o.t. Results are shown by bin in Figure 61, Figure 62, and Figure 63. The same results are converted into “physical” binning (i.e. in bins of the muon kinematics) for water-in (Figure 64 and Figure 65), water-out (Figure 66 and Figure 67), and on-water (Figure 68 and Figure 69). Systematics are shown for all sources; FSI, flux, interaction, detectors, and statistics. The solid red line is the true cross-section in each bin from NEUT, while the dashed blue line is the true cross-section from GENIE.

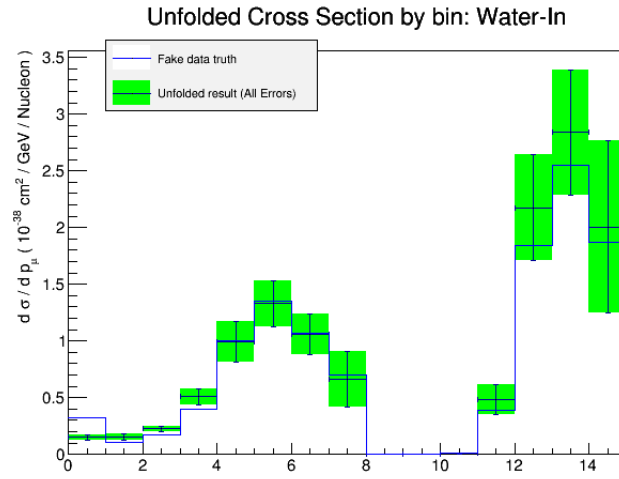


Figure 61: Water-in fake data cross-section results by bin. The total uncertainty is the uncertainty from each error source summed in quadrature.

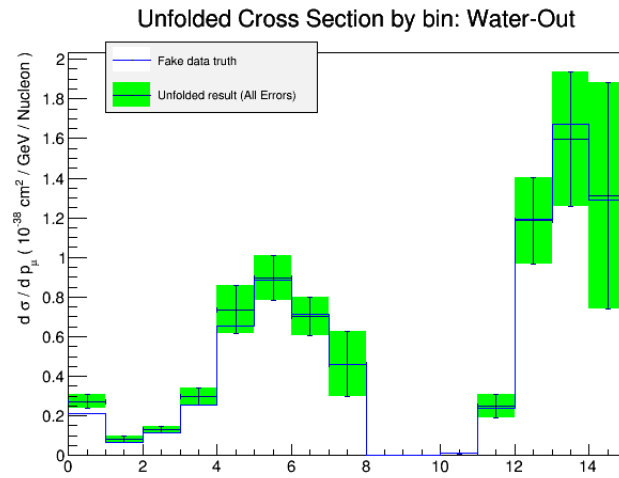


Figure 62: Water-out fake data truth cross-section results by bin. The total uncertainty is the uncertainty from each error source summed in quadrature.

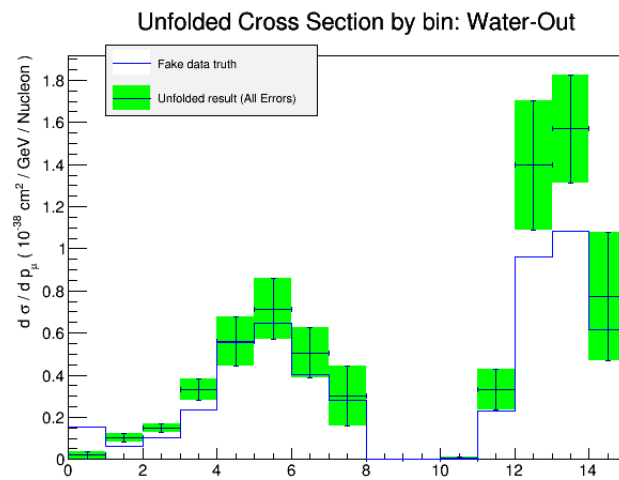


Figure 63: On-water fake data cross-section results by bin. The total uncertainty is the uncertainty from each error source summed in quadrature.

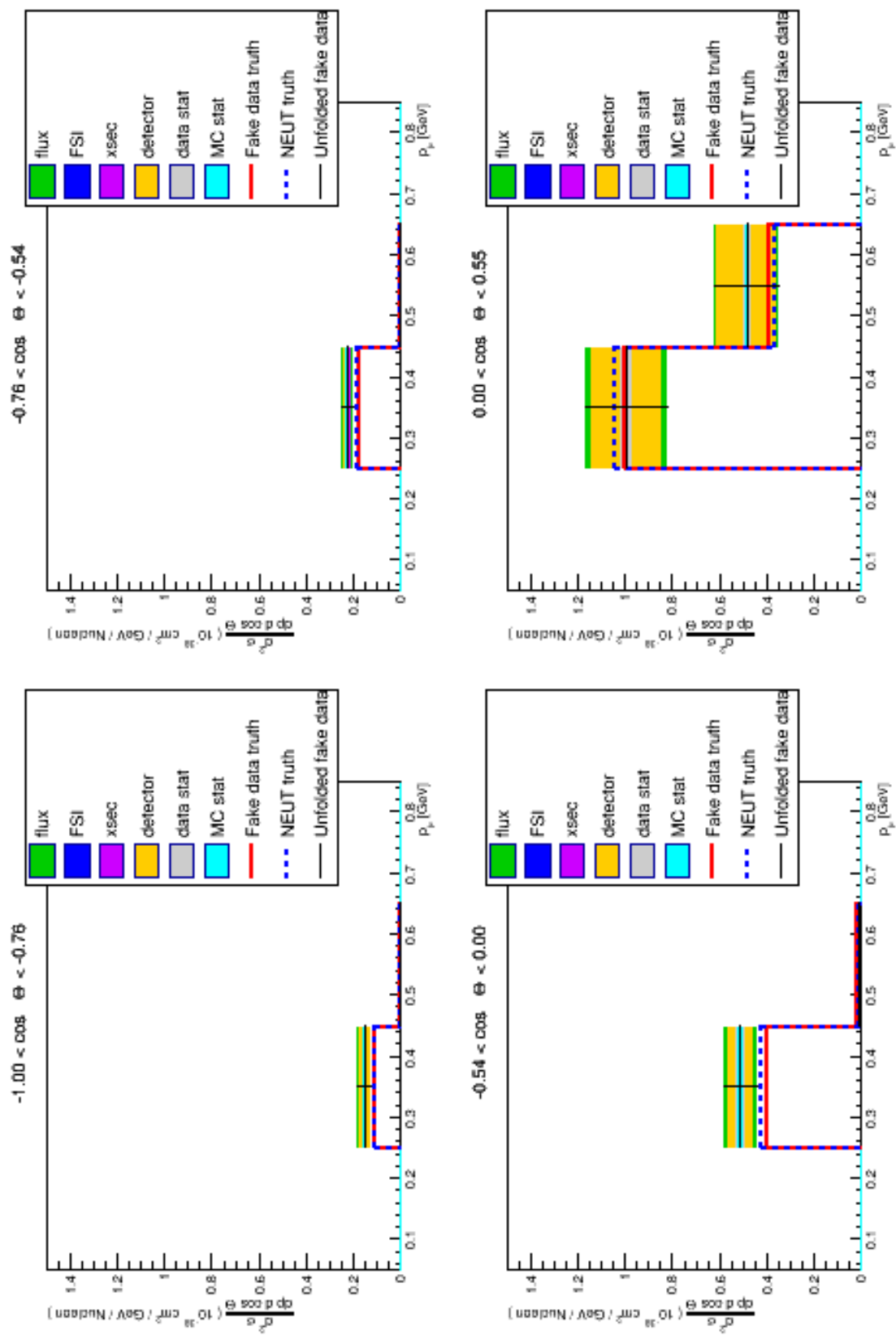


Figure 64: Water-in cross-section for $\cos \theta < 0$. Each histogram is a single $\cos \theta$ bin.

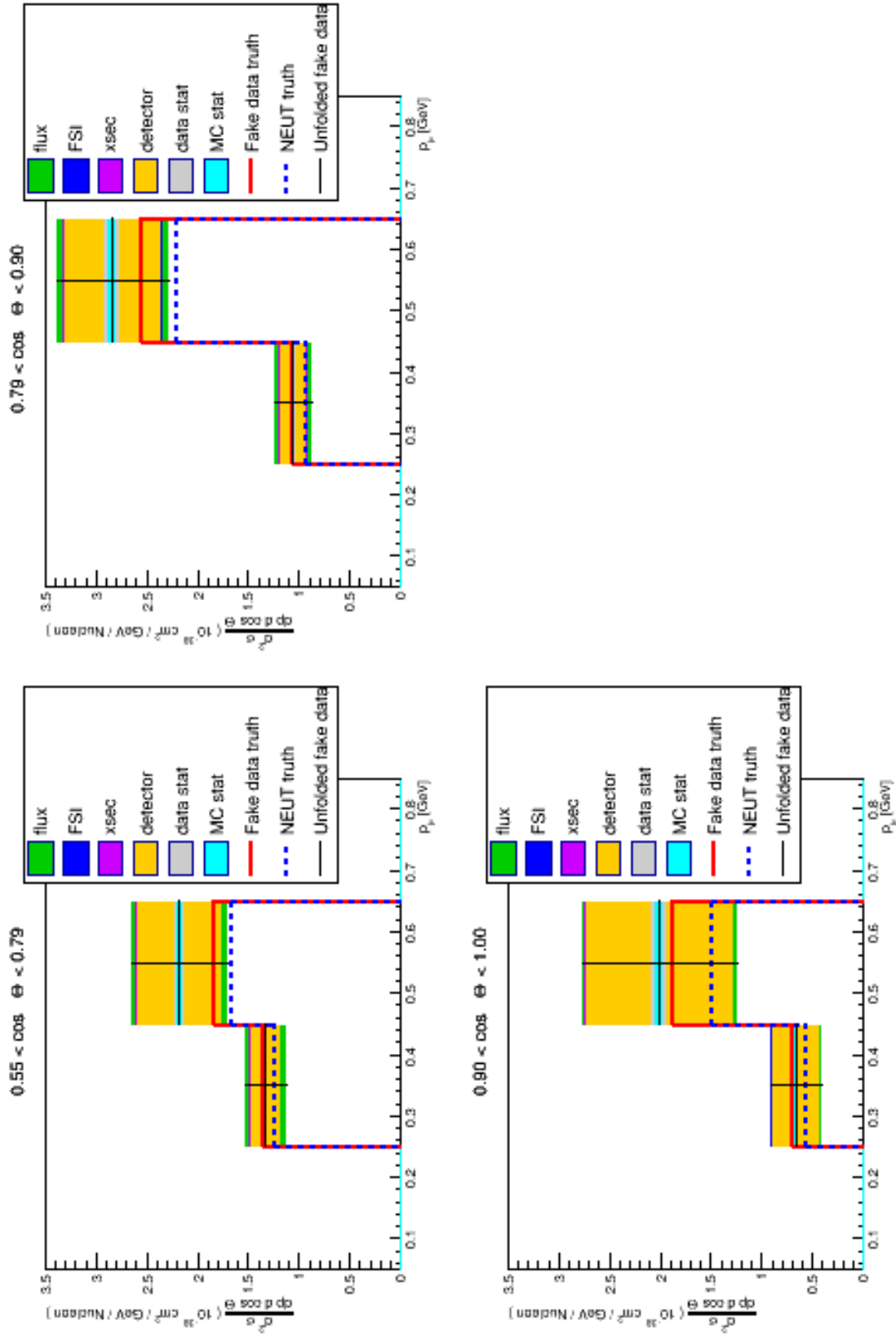


Figure 65: Water-in cross-section for $\cos \theta > 0$. Each histogram is a single $\cos \theta$ bin.

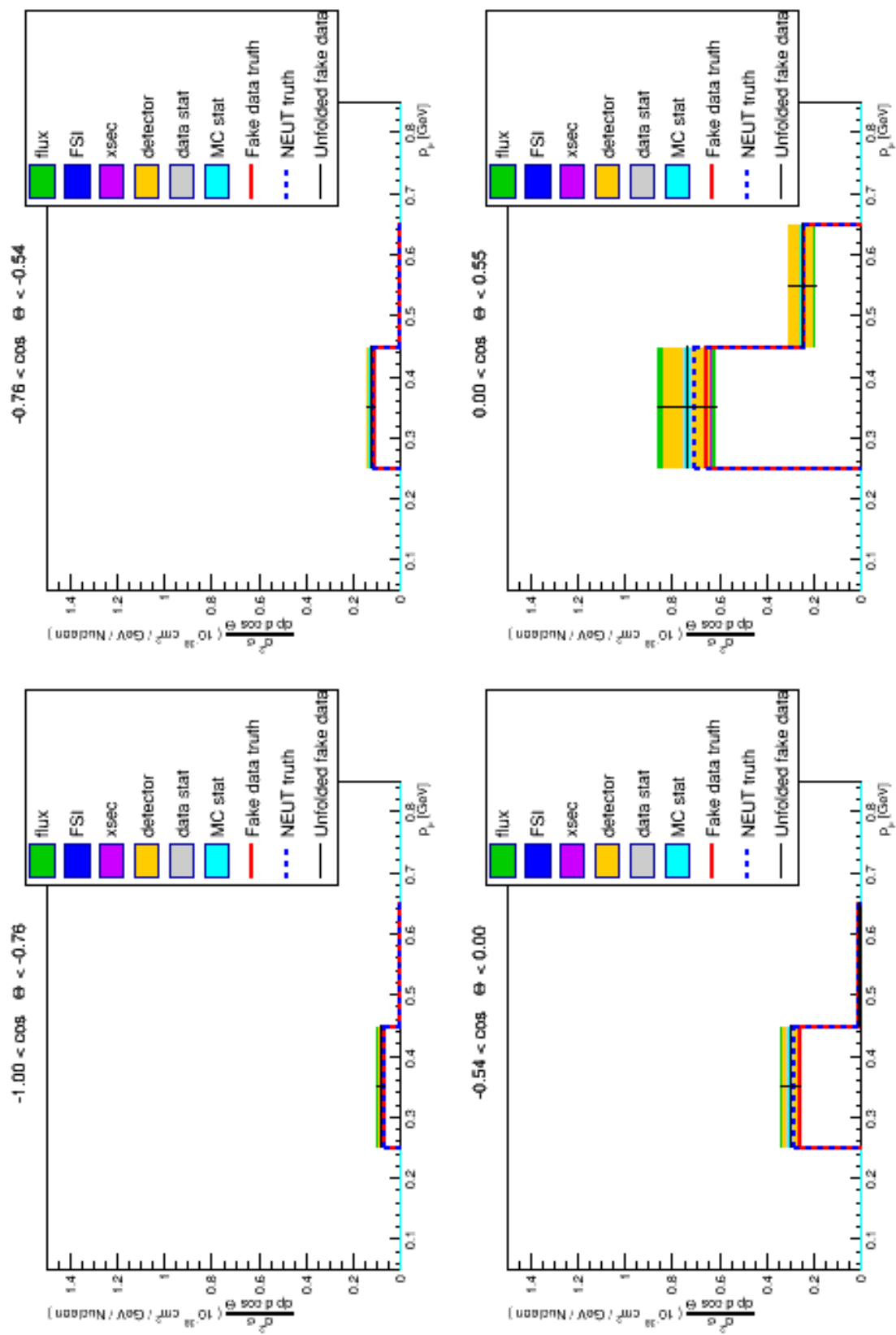


Figure 66: Water-out cross-section for $\cos \theta < 0$. Each histogram is a single $\cos \theta$ bin.

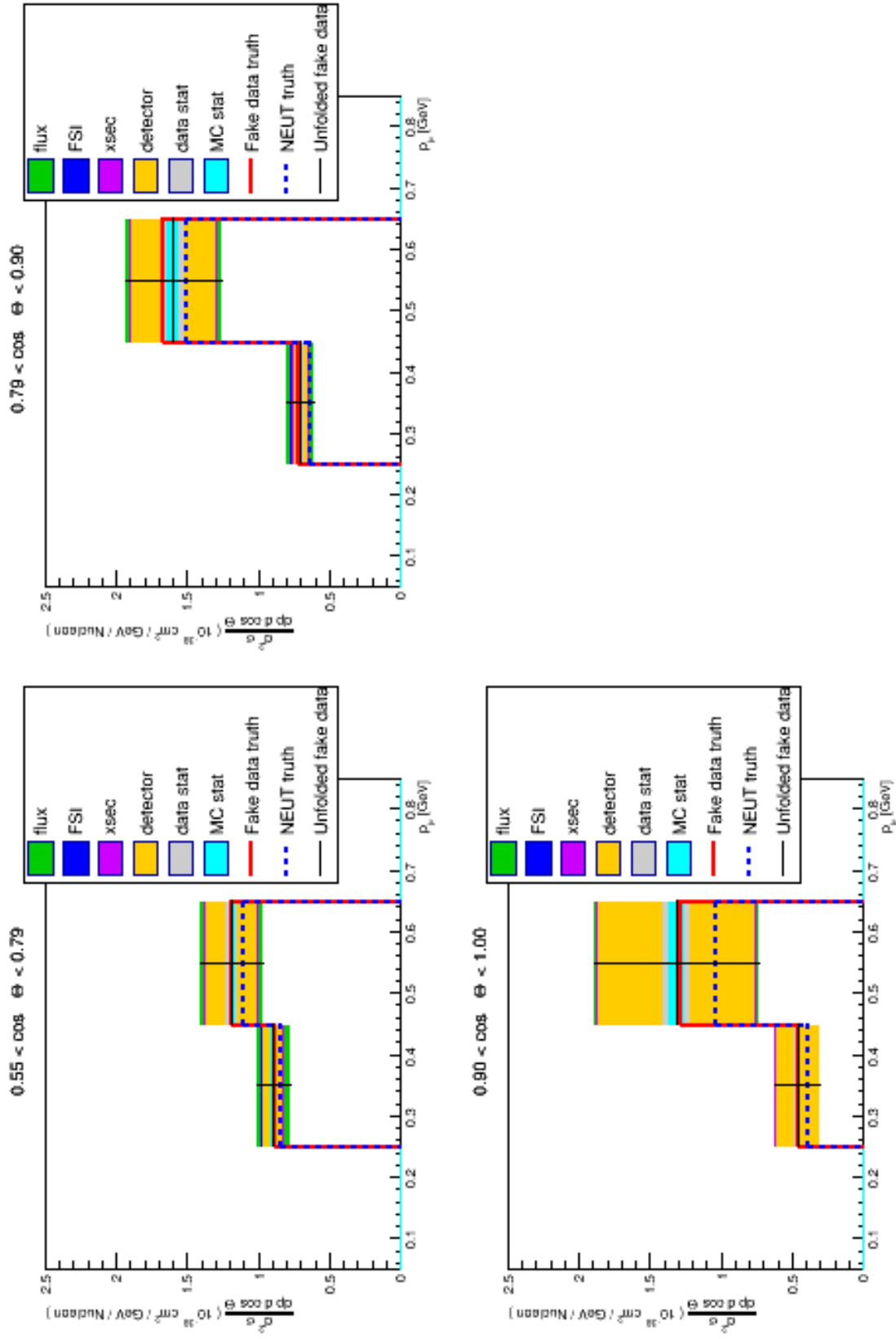


Figure 67: Water-out cross-section for $\cos \theta > 0$. Each histogram is a single $\cos \theta$ bin.

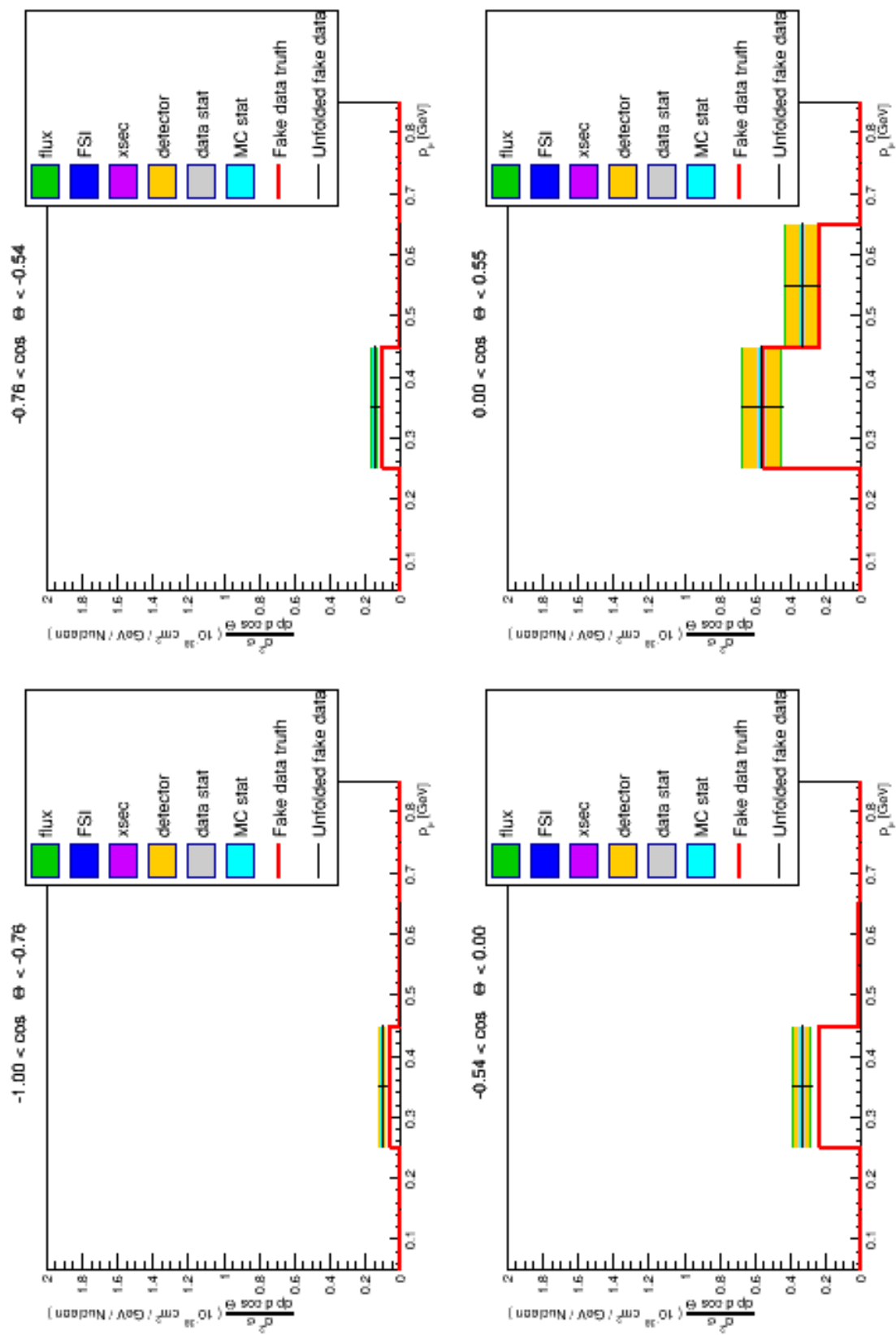


Figure 68: On-Water cross-section for $\cos \theta < 0$. Each histogram is a single $\cos \theta$ bin.

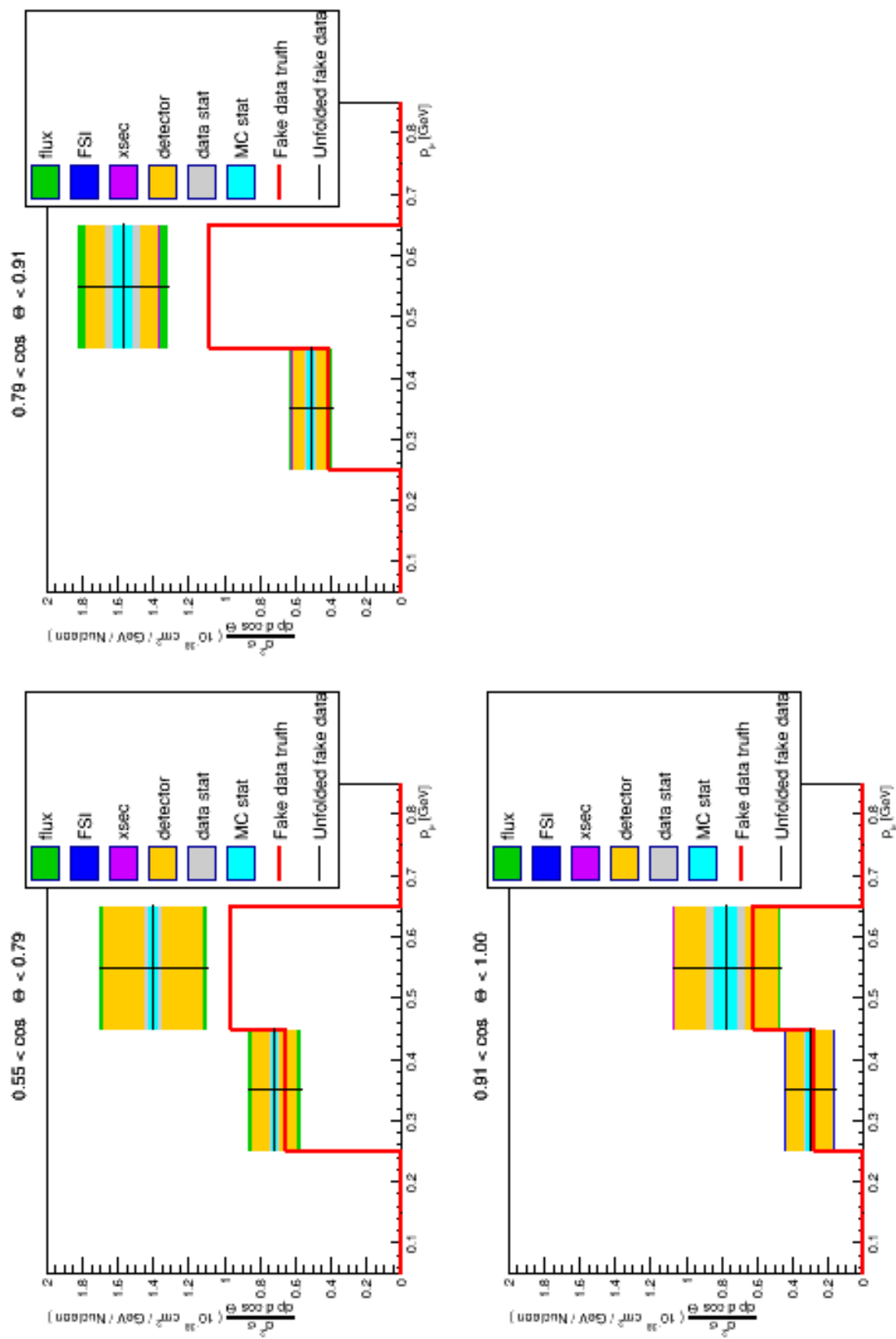


Figure 69: On-Water cross-section for $\cos \theta > 0$. Each histogram is a single $\cos \theta$ bin.

5.2 DATA

The selection process and cross-section calculation detailed in this paper were performed on data from T2K Runs 2-4, corresponding to 2.06×10^{20} p.o.t. in water-in mode and 2.12×10^{20} p.o.t. in water-out mode.

The reconstructed kinematics of the selected muon are shown in Figures 70 (water-in) and 71 (water-out). There is a clear excess of events in data compared to MC, particularly in the backward direction. This excess is approximately 7% higher for water-in, and 11% higher for water out. The ratio of backward tracks to total tracks (R_D^S ; see Section 4.2.4) is 0.16 (0.21) for water-in (water-out), which is significantly higher than either GENIE or NEUT (Table 10).

This excess is reflected in the unfolded results for water-in (Figures 75 and 76) and water-out (Figures 77 and 78), where the unfolded results are consistently higher than the NEUT MC truth. For the cross-section on water, this excess is subtracted out somewhat, and the cross-section is closer to the nominal generator truth (Figures 79 and 80). This implies that the excess is related to differences between the MC and actual cross-section on the detector materials, though this requires study beyond the scope of this paper. There are a number of analyses in development in T2K designed to understand the differences between the various MC generators and data in order to improve upon our current, incomplete models.

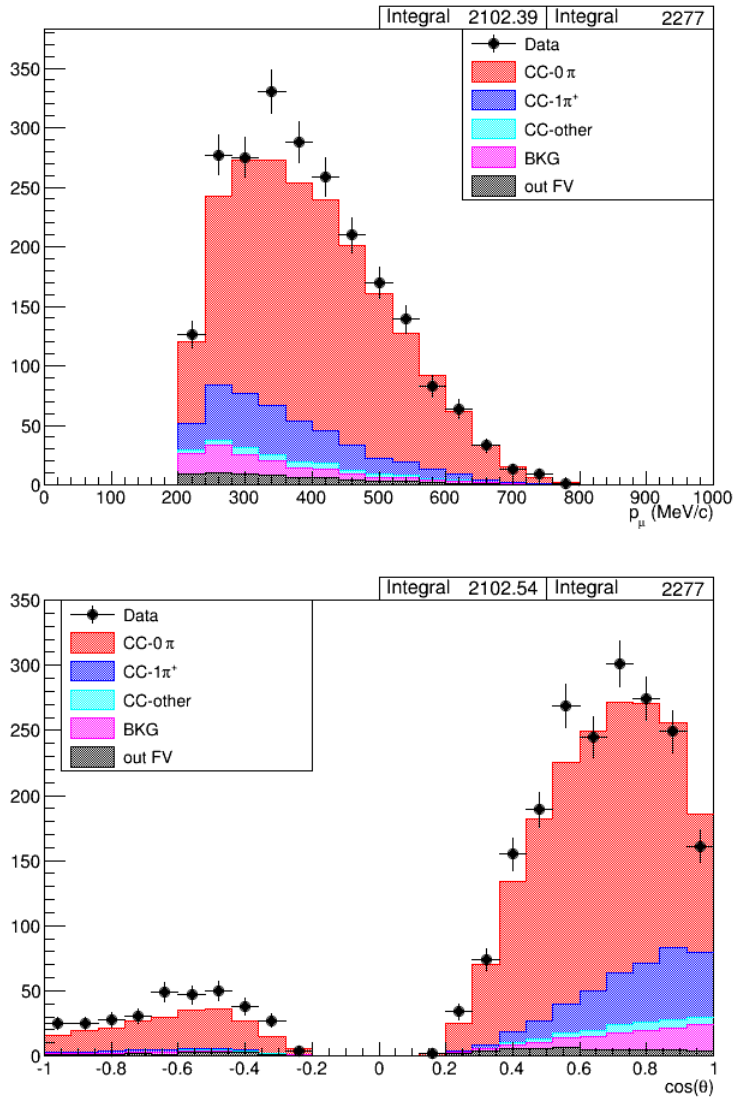


Figure 70: Water-in reconstructed muon kinematics: muon momentum p_μ (top) and $\cos \theta$ (bottom).

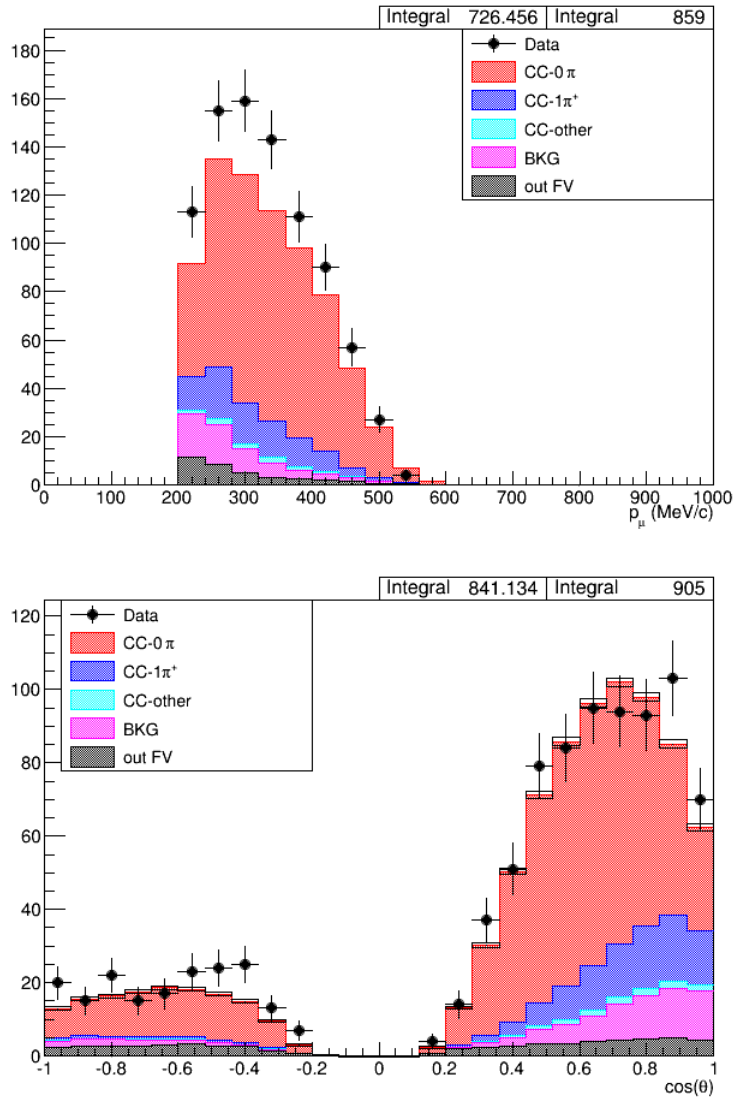


Figure 71: Water-out reconstructed muon kinematics: muon momentum p_μ (top) and $\cos \theta$ (bottom).

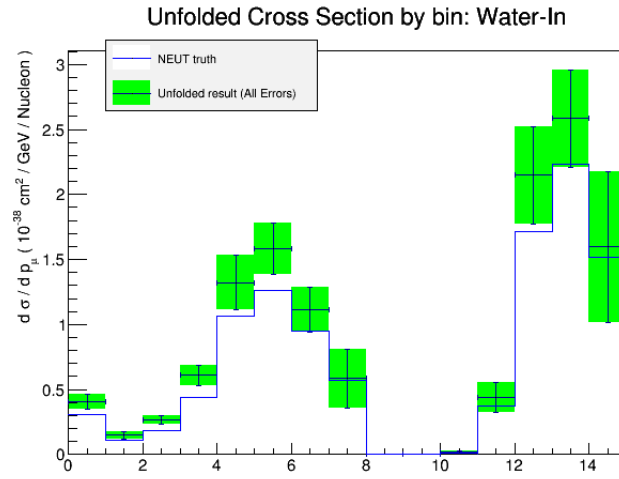


Figure 72: Water-in cross-section results by bin. The total uncertainty is the uncertainty from each error source summed in quadrature.

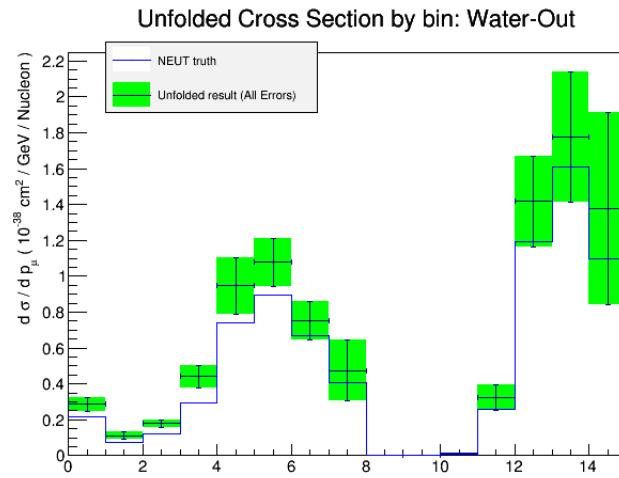


Figure 73: Water-out cross-section results by bin. The total uncertainty is the uncertainty from each error source summed in quadrature.

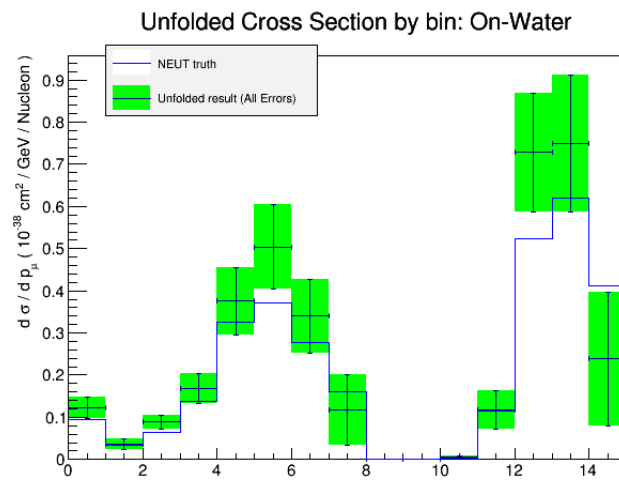


Figure 74: On-water cross-section results by bin. The total uncertainty is the uncertainty from each error source summed in quadrature.

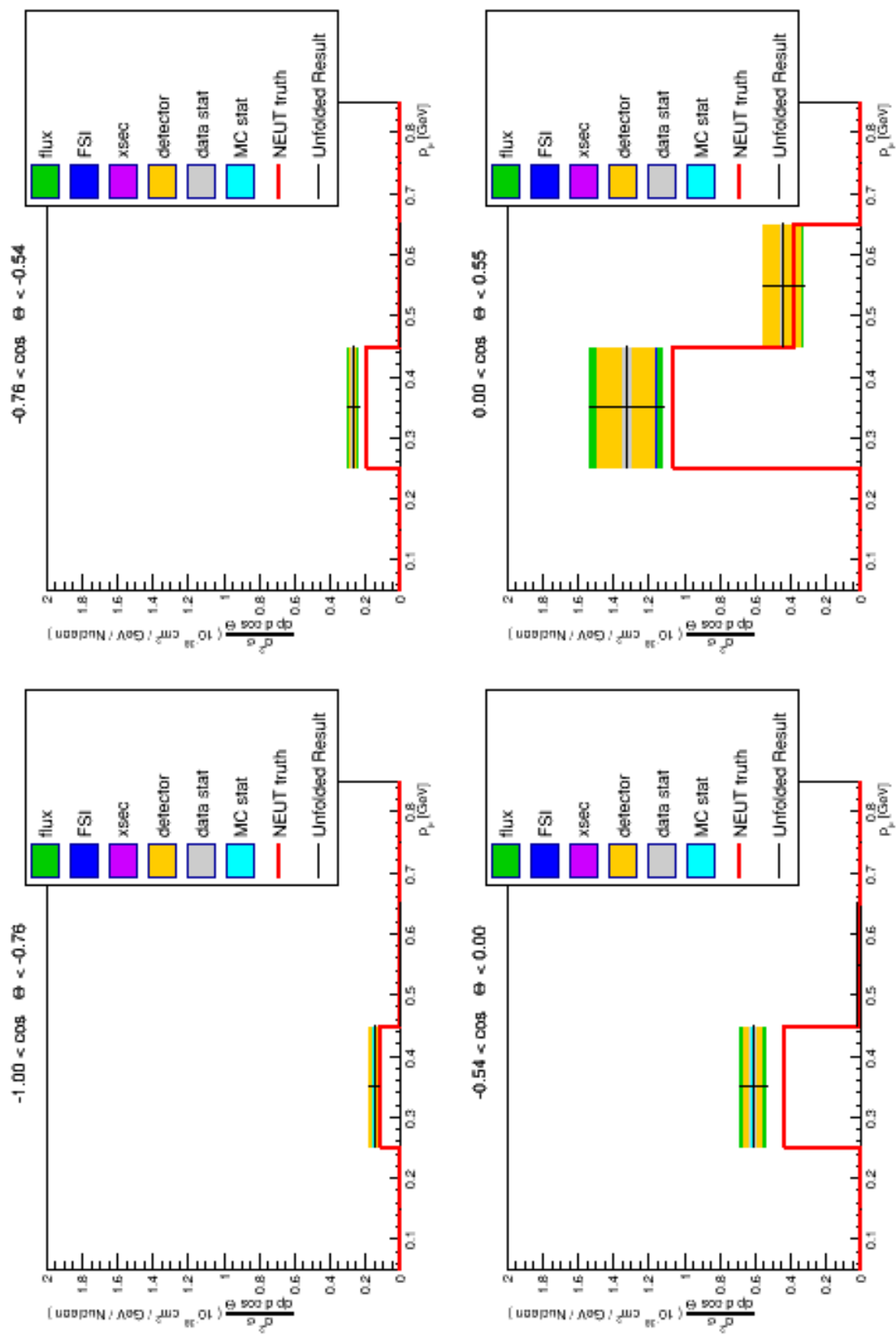


Figure 75: Water-in cross-section for $\cos \theta < 0$. Each histogram is a single $\cos \theta$ bin.

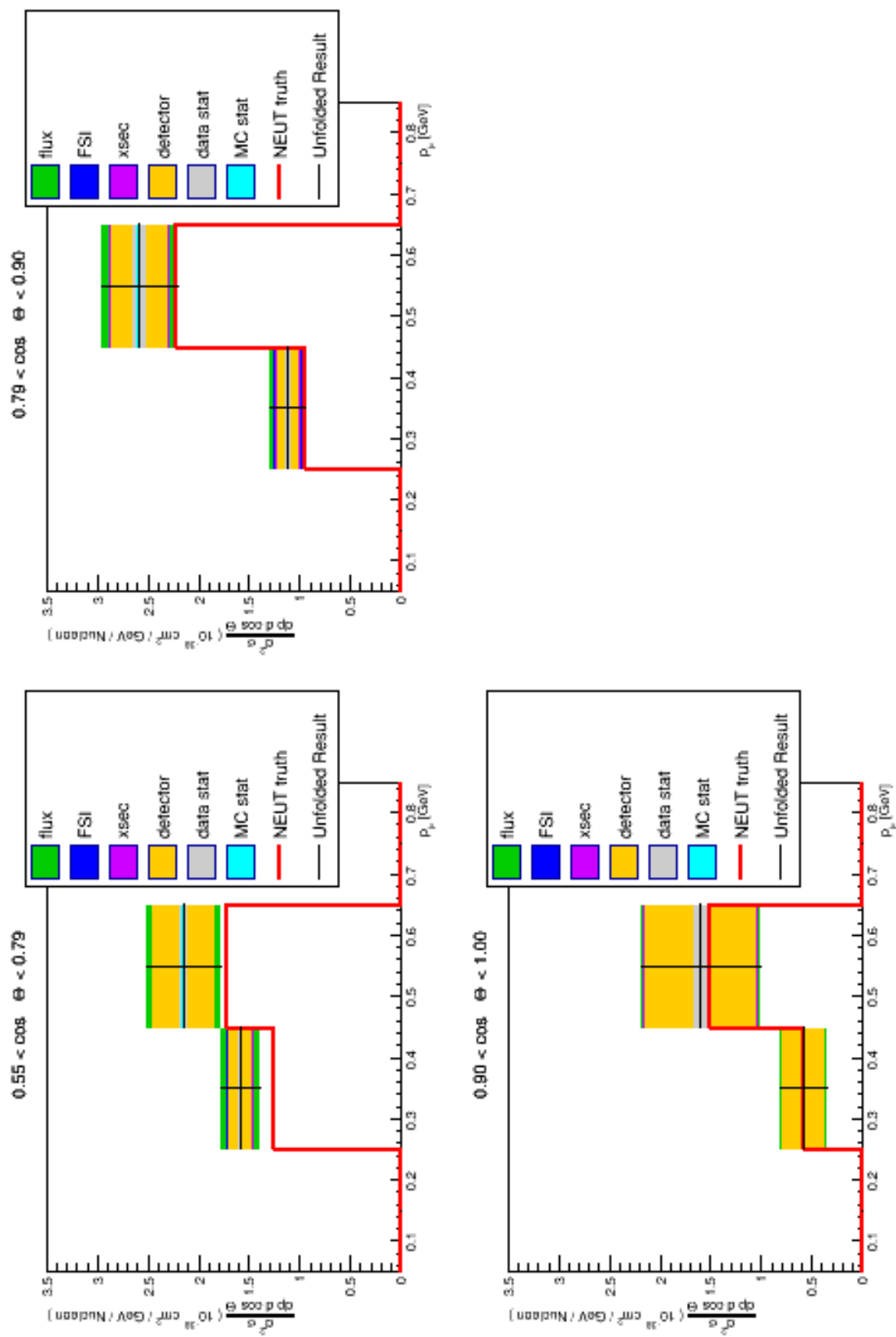


Figure 76: Water-in cross-section for $\cos \theta > 0$. Each histogram is a single $\cos \theta$ bin.

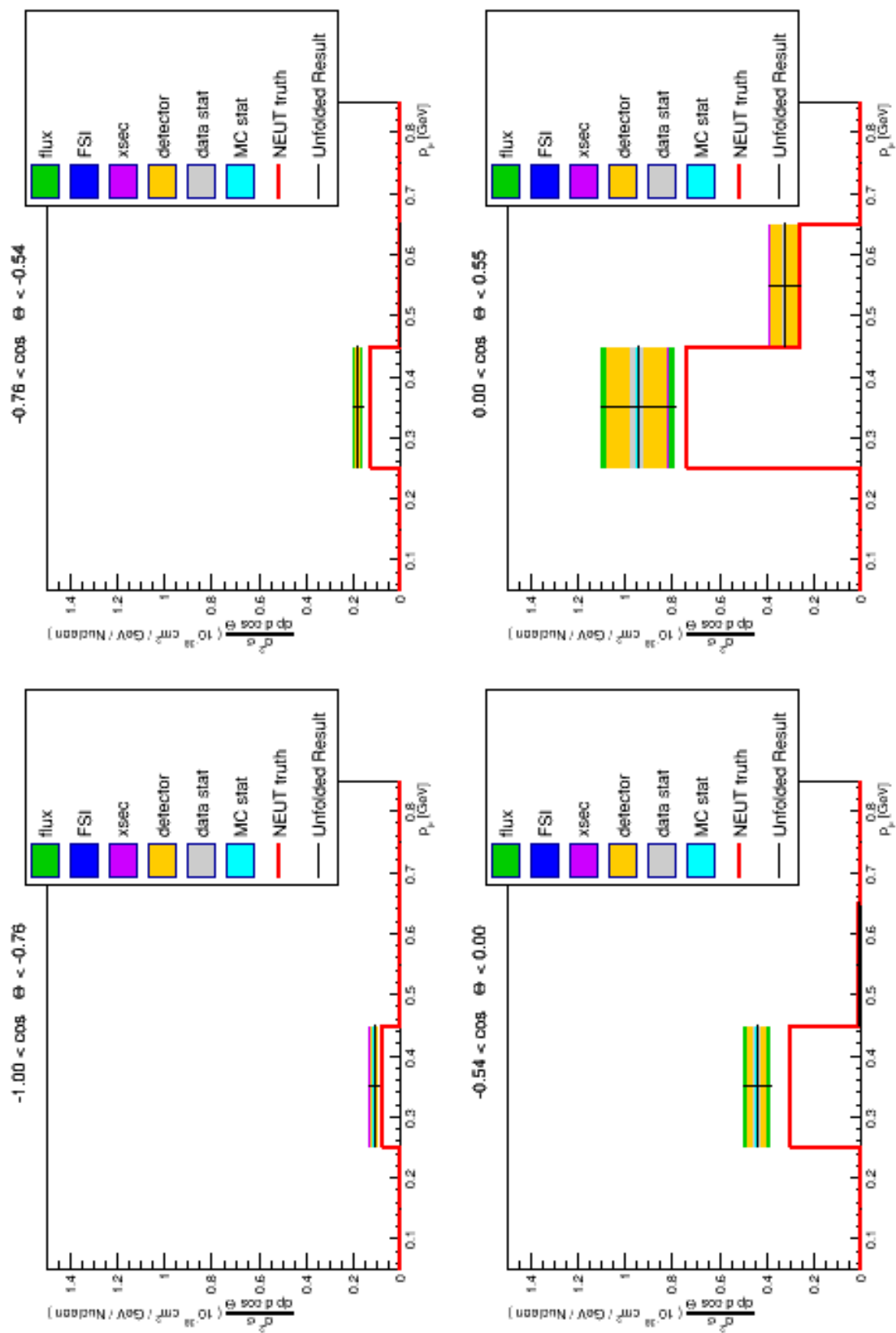


Figure 77: Water-out cross-section for $\cos \theta < 0$. Each histogram is a single $\cos \theta$ bin.

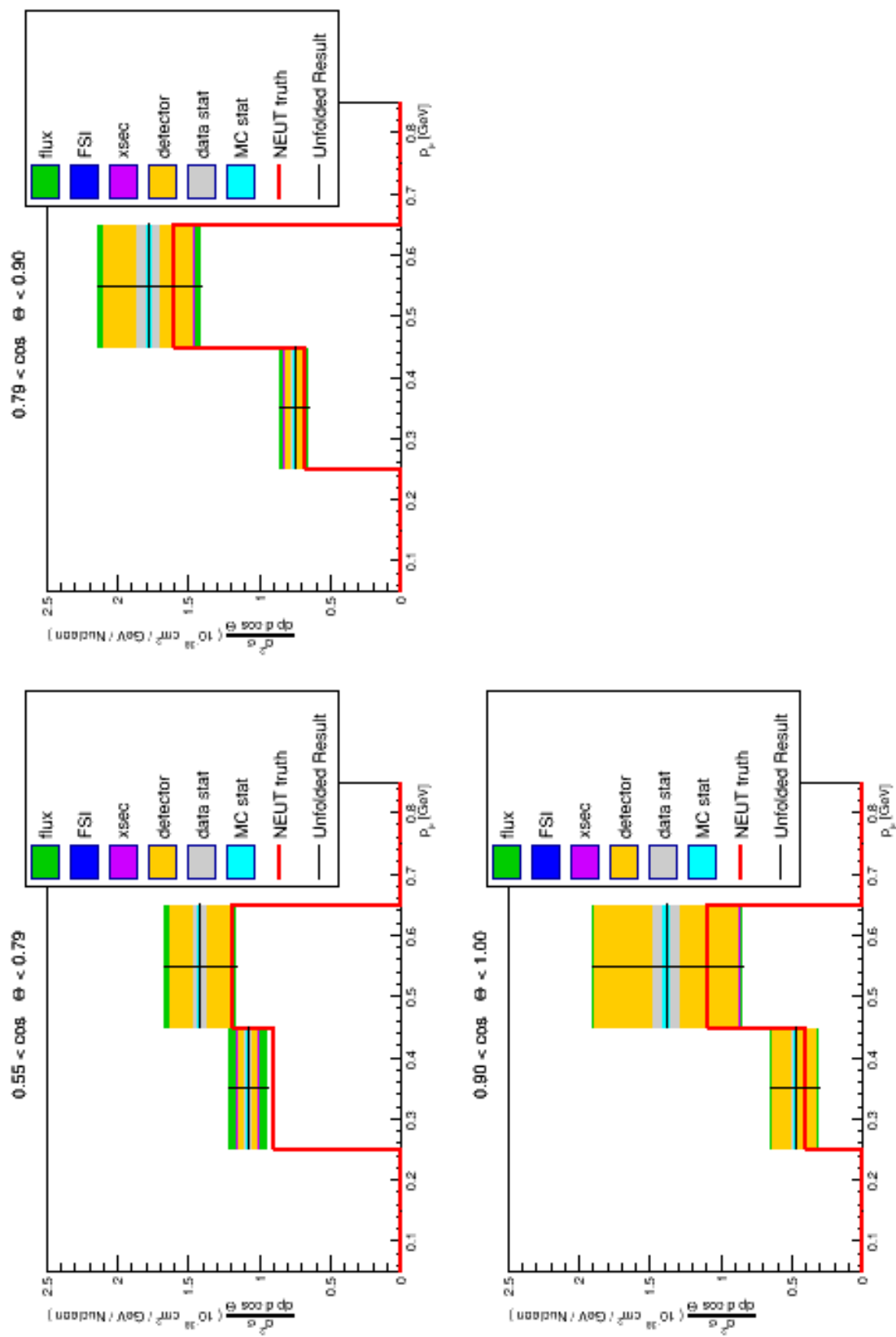


Figure 78: Water-out cross-section for $\cos \theta > 0$. Each histogram is a single $\cos \theta$ bin.

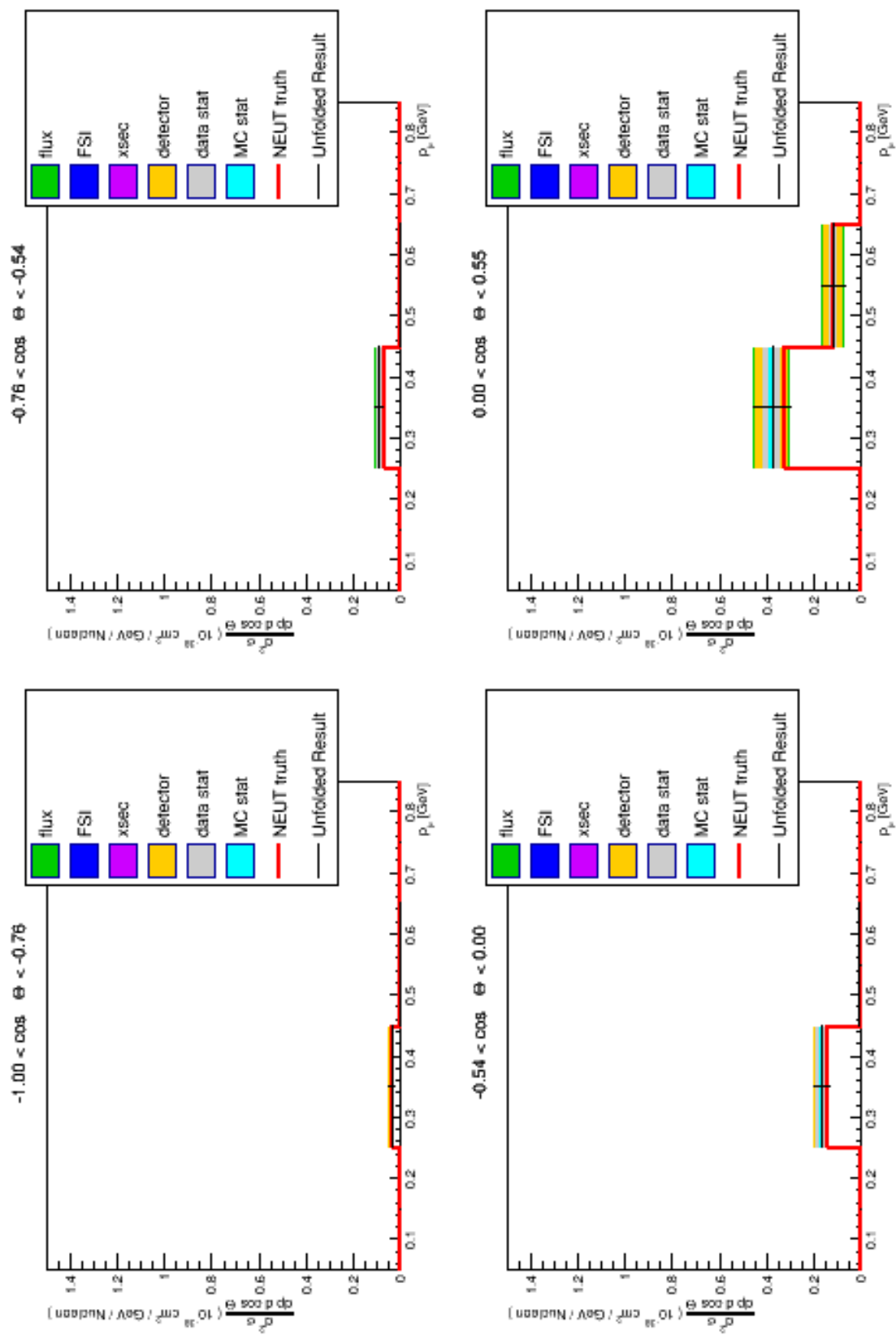


Figure 79: On-Water cross-section for $\cos \theta < 0$. Each histogram is a single $\cos \theta$ bin.

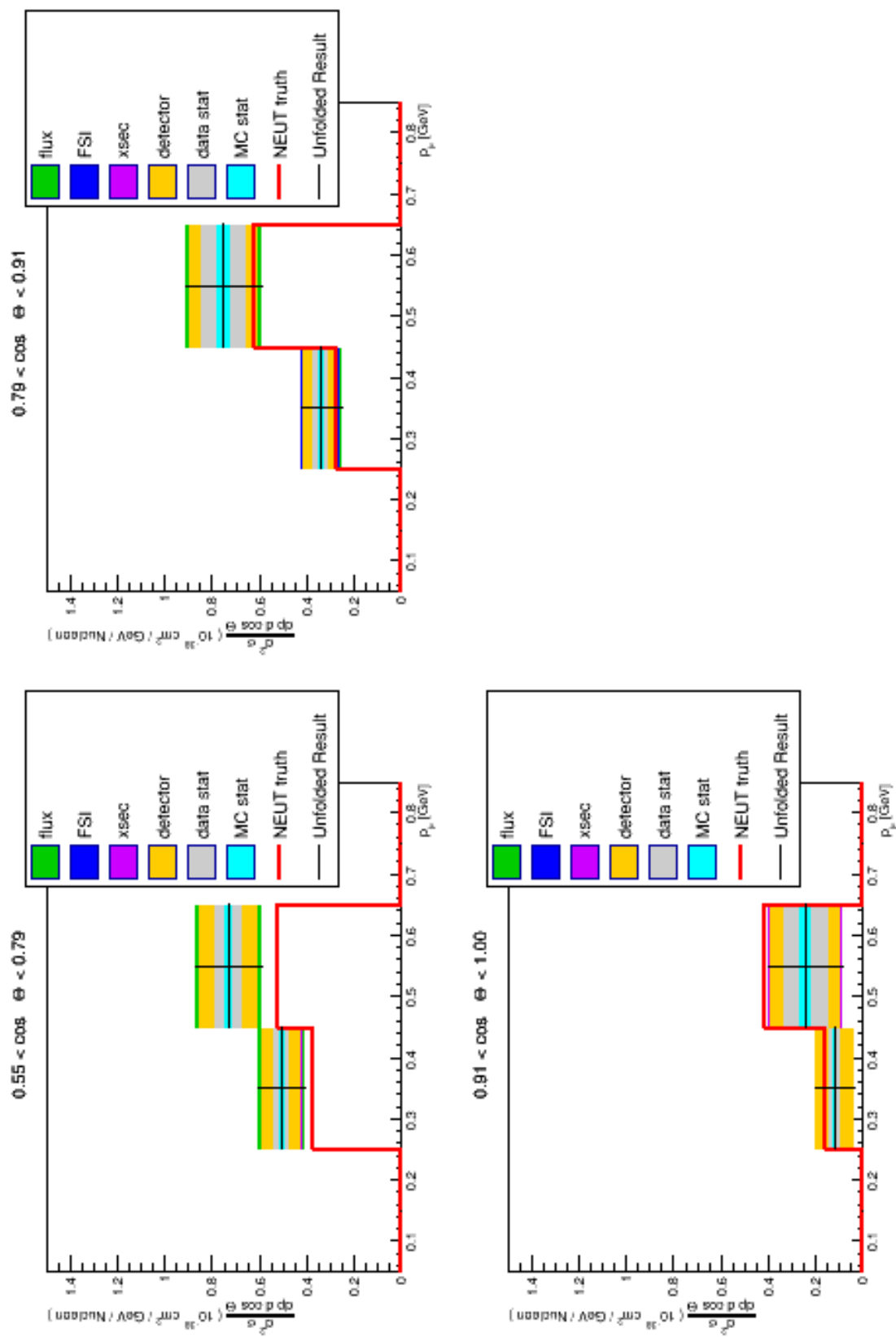


Figure 80: On-Water cross-section for $\cos \theta > 0$. Each histogram is a single $\cos \theta$ bin.

6.0 SUMMARY

This thesis has presented the results for a double differential ν_μ CC- 0π cross-section on water in the P \emptyset D in bins of p_μ and $\cos\theta_\mu$. The current state of neutrino oscillations and interactions was reviewed, and an overview of the T2K experiment (the near detector complex and the P \emptyset D in particular) was given.

The CC- 0π event selection was designed to find single muon tracks contained within the P \emptyset D in order to expand the available phase space for the existing P \emptyset D \rightarrow Tracker CC- 0π analysis. Two algorithms for reconstructing the muon momentum from the track length were developed, as well as a means of determining the upstream/downstream directionality of the muon track. This analysis is the first P \emptyset D analysis to access the full angular phase space of the out-going particle (a similar, but unfinished, analysis is in development for the Tracker).

The on-water cross-section was calculated using a single-iteration Bayesian unfolding scheme implemented in the xsTool software package. This method has been the T2K cross-section group's approved technique for recent analyses, including the P \emptyset D \rightarrow Tracker CC- 0π analysis, though alternatives and improvements upon this method are currently in development.

There is a clear excess in the data compared to the nominal MC prediction, particularly for the backward-going ($\cos\theta < 0$) muon tracks. This excess is present for both water-in and water-out modes, which implies that the predicted cross-section on the heavier P \emptyset D materials is too low in the current MC models, though further study needed to determine the origin

of these events. Due to the interplay between nuclear models, cross-section uncertainties, and detector effects, it is often difficult to pinpoint the source for data/MC discrepancies. Developing accurate and powerful methods to discriminate between the various neutrino interaction models is a high priority in the T2K research group, with several different analyses nearing completion.

The event selection presented in the paper was developed in the Highland2 analysis framework common to ND280 cross-section analyses. This analysis is the second P θ D-based analysis to be developed in Highland2, and the first using p0dRecon structures instead of globalRecon. The transition of the P θ D research group to Highland2 was lead Tianlu Yuan¹ and myself over the past several years. Developing and validating the p0dRecon infrastructure in Highland2 is the most significant component of my contribution to the T2K research program.

¹Formerly a T2K researcher as a graduate student at University of Colorado; now a post-doc at University of Wisconsin

APPENDIX A

NEUTRINO MIXING PARAMETERS

The current best fits for the 3ν mixing parameters are given in Table.13. Solar, atmospheric, reactor, and accelerator sources were used, but cosmological studies were not included into any global fits. All fits were performed in [58] and reproduced in the Particle Data Group 2016 Review[51]. Also listed are the 3σ “contours.” This survey reported their results using the mass parameter $|\Delta m^2| = m_3^2 - (m_1^2 + m_2^2)/2$. In this formulation, $\Delta m^2 > 0$ (< 0) when the masses are in the normal hierarchy NH (IH).

The fractional accuracies for the known oscillation parameters (excluding the Dirac and possible Majorana phases) are all $< 10\%$. While all values are allowed at the 3σ level, the data from T2K and NO ν A (both separately and jointly) suggest that $\sin\delta < 0$. As of yet there is no statistically significant indication of which mass hierarchy is correct. The best constraints on the sum of the absolute neutrino masses ($\Sigma \leq 0.23\text{eV}$) still come from cosmological studies[59].

Table 13: The current global best fits for the ν mixing parameters[51].

Parameter	Normal Hierarchy		Inverted Hierarchy	
	best fit	3σ	best fit	3σ
$\Delta m_{21}^2 (10^{-5} eV^2)$	7.37	6.93 - 7.97	7.37	6.93 - 7.97
$ \Delta m^2 (10^{-3} eV^2)$	2.50	2.37 - 2.63	2.46	2.33 - 2.60
$\sin^2 \theta_{12}$	0.297	0.250 - 0.354	0.297	0.250 - 0.354
$\sin^2 \theta_{23}$	0.437	0.379 - 0.616	0.569	0.383 - 0.637
$\sin^2 \theta_{13}$	0.0214	0.0185 - 0.0246	0.0218	0.0186 - 0.0248
δ_{CP}/π	1.35	0 - 2	1.32	0 - 2

APPENDIX B

MAJORANA AND DIRAC NEUTRINOS

If neutrinos are Majorana particles, the mass states cannot be rephrased and two additional Majorana phases are present. This is a consequence of the coupling of the left and right-handed components of the neutrino spinors. The Majorana phases are diagonalized in the basis of the matrix representation discussed above (sometimes called the Dirac representation matrix), and the mixing matrix can be rewritten as $U = U_D U_M$ (Fig. 81). However, since weak interactions are left-handed, the right-handed component of a Majorana neutrino plays no role in either neutrino interactions or oscillations, and there is no distinction between massive Dirac and Majorana neutrinos.

$$U = \begin{pmatrix} c_{12}c_{13} & s_{12}c_{13} & s_{13}e^{-i\delta} \\ -s_{12}c_{23} - c_{12}s_{23}s_{13}e^{i\delta} & c_{12}c_{23} - s_{12}s_{23}s_{13}e^{i\delta} & s_{23}c_{13} \\ s_{12}s_{23} - c_{12}c_{23}s_{13}e^{i\delta} & -c_{12}s_{23} - s_{12}c_{23}s_{13}e^{i\delta} & c_{23}c_{13} \end{pmatrix} \begin{pmatrix} 1 & 0 & 0 \\ 0 & e^{-i\frac{\alpha_{21}}{2}} & 0 \\ 0 & 0 & e^{-i\frac{\alpha_{31}}{2}} \end{pmatrix}$$

Figure 81: The PMNS neutrino mixing matrix. The diagonal matrix on the right contains the two Majorana phase terms, which are included for completeness. The term c_{ij} (s_{ij}) stands for $\cos\theta_{ij}$ ($\sin\theta_{ij}$), where θ_{ij} is one of the three mixing angles, and δ is the CP-violating phase.

BIBLIOGRAPHY

- [1] Wolfgang Pauli. Dear radioactive ladies and gentlemen, Dec 1930. <http://microboone-docdb.fnal.gov/cgi-bin/RetrieveFile?docid=953;filename=pauli%20letter1930.pdf>.
- [2] C. L. Cowan, F. Reines, F. B. Harrison, H. W. Kruse, and A. D. McGuire. Detection of the free neutrino: a confirmation. *Science*, 124(3212):103–104, 1956.
- [3] Raymond Davis, Don S. Harmer, and Kenneth C. Hoffman. Search for neutrinos from the sun. *Phys. Rev. Lett.*, 20:1205–1209, May 1968. <http://link.aps.org/doi/10.1103/PhysRevLett.20.1205>.
- [4] John N. Bahcall, Neta A. Bahcall, and Giora Shaviv. Present status of the theoretical predictions for the ^{37}Cl solar-neutrino experiment. *Phys. Rev. Lett.*, 20:1209–1212, May 1968. <http://link.aps.org/doi/10.1103/PhysRevLett.20.1209>.
- [5] K. S. Hirata, T. Kajita, K. Kifune, K. Kihara, and M. Nakahata. Observation of B-8 solar neutrinos in the Kamiokande-II detector. *Physical Review Letters*, 63:16–19, July 1989.
- [6] P. Anselmann et al. Solar neutrinos observed by GALLEX at Gran Sasso. *Phys. Lett.*, B285:376–389, 1992.
- [7] Dzh.N. Abdurashitov et al. Results from SAGE. *Phys. Lett.*, B328:234–248, 1994.
- [8] B. Pontecorvo. Neutrino experiments and the question of leptonic-charge conservation. *Sov. Phys. JETP*, 26:984–988, 1968.
- [9] Y. Fukuda et al. Evidence for oscillation of atmospheric neutrinos. *Phys. Rev. Lett.*, 81:1562–1567, 1998.
- [10] Q. R. Ahmad et al. Measurement of the rate of $\nu_e + d \rightarrow p + p + e^-$ interactions produced by ^8B solar neutrinos at the Sudbury Neutrino Observatory. *Phys. Rev. Lett.*, 87:071301, 2001.

- [11] Y. Fukuda et al. Constraints on neutrino oscillation parameters from the measurement of day night solar neutrino fluxes at Super-Kamiokande. *Phys. Rev. Lett.*, 82:1810–1814, 1999.
- [12] Z. Q. et al Liu. Study of $e^+e^- \rightarrow \pi^+\pi^-j/\psi$ and observation of a charged charmoniumlike state at belle. *Phys. Rev. Lett.*, 110:252002, Jun 2013. <http://link.aps.org/doi/10.1103/PhysRevLett.110.252002>.
- [13] M. et al Ablikim. Observation of a charged charmoniumlike structure in $e^+e^- \rightarrow \pi^+\pi^-j/\psi$ at $\sqrt{s}=4.26$ GeV. *Phys. Rev. Lett.*, 110:252001, Jun 2013. <http://link.aps.org/doi/10.1103/PhysRevLett.110.252001>.
- [14] Roel Aaij et al. Observation of J/p Resonances Consistent with Pentaquark States in Λ_b^0 J/K $^-$ p Decays. *Phys. Rev. Lett.*, 115:072001, 2015.
- [15] Georges Aad et al. Observation of a new particle in the search for the Standard Model Higgs boson with the ATLAS detector at the LHC. *Phys. Lett.*, B716:1–29, 2012.
- [16] Serguei Chatrchyan et al. Observation of a new boson at a mass of 125 GeV with the CMS experiment at the LHC. *Phys. Lett.*, B716:30–61, 2012.
- [17] Standard model of elementary particles, 2014. https://en.wikipedia.org/wiki/File:Standard_Model_of_Elementary_Particles.svg.
- [18] C. S. Wu, E. Ambler, R. W. Hayward, D. D. Hoppes, and R. P. Hudson. Experimental Test of Parity Conservation in Beta Decay. *Phys. Rev.*, 105:1413–1414, 1957.
- [19] C. H. Llewellyn Smith. Neutrino Reactions at Accelerator Energies. *Phys. Rept.*, 3:261, 1972.
- [20] J. A. Formaggio and G. P. Zeller. From ev to eev: Neutrino cross sections across energy scales. *Rev. Mod. Phys.*, 84:1307–1341, Sep 2012.
- [21] A. A. Aguilar-Arevalo et al. First Measurement of the Muon Neutrino Charged Current Quasielastic Double Differential Cross Section. *Phys. Rev.*, D81:092005, 2010.
- [22] A. Bodek, S. Avvakumov, R. Bradford, and Howard Scott Budd. Vector and Axial Nucleon Form Factors:A Duality Constrained Parameterization. *Eur. Phys. J.*, C53:349–354, 2008.
- [23] P. Adamson et al. Study of quasielastic scattering using charged-current ν -iron interactions in the MINOS near detector. *Phys. Rev.*, D91(1):012005, 2015.
- [24] X. Espinal and F. Sánchez. Measurement of the axial vector mass in neutrino-carbon interactions at k2k. *AIP Conference Proceedings*, 967(1):117–122, 2007.
- [25] R. et al Gran. Measurement of the quasielastic axial vector mass in neutrino interactions on oxygen. *Phys. Rev. D*, 74:052002, Sep 2006.

- [26] D. Casper. The Nuance neutrino physics simulation, and the future. *Nucl. Phys. Proc. Suppl.*, 112:161–170, 2002. [[161\(2002\)](#)].
- [27] S. Schael et al. Precision electroweak measurements on the Z resonance. *Phys. Rept.*, 427:257–454, 2006.
- [28] Ziro Maki, Masami Nakagawa, and Shoichi Sakata. Remarks on the unified model of elementary particles. *Prog. Theor. Phys.*, 28:870–880, 1962.
- [29] Carlo Giunti and Kim Chung Wook. *Fundamentals of Neutrino Physics and Astrophysics*. Oxford Univ., Oxford, 2007.
- [30] P. Adamson et al. Precision measurement of the speed of propagation of neutrinos using the MINOS detectors. *Phys. Rev.*, D92(5):052005, 2015.
- [31] T. Adam et al. Measurement of the neutrino velocity with the OPERA detector in the CNGS beam using the 2012 dedicated data. *JHEP*, 01:153, 2013.
- [32] K. Abe et al. The T2K experiment. *Nuclear Instruments and Methods in Physics Research Section A: Accelerators, Spectrometers, Detectors and Associated Equipment*, 659.1:106–135, 2011. <http://www.sciencedirect.com/science/article/pii/S0168900211011910>.
- [33] K. Abe et al. T2k neutrino flux prediction. *Physical Review D*, 87:012001, Jan 2013. <http://link.aps.org/doi/10.1103/PhysRevD.87.012001>.
- [34] N. Abgrall et al. Measurements of cross sections and charged pion spectra in proton-carbon interactions at 31 gev/ c . *Phys. Rev. C*, 84:034604, Sep 2011. <http://link.aps.org/doi/10.1103/PhysRevC.84.034604>.
- [35] K. Abe et al. Measurements of the T2K neutrino beam properties using the ingrid on-axis near detector. *Nuclear Instruments and Methods in Physics Research Section A: Accelerators, Spectrometers, Detectors and Associated Equipment*, 694:211–223, 2012.
- [36] S. Assylbekov et al. The T2K nd280 off-axis pi-zero detector. *Nuclear Instruments and Methods in Physics Research Section A: Accelerators, Spectrometers, Detectors and Associated Equipment*, 686:48–63, 2012.
- [37] A. Vacheret et al. Characterization and simulation of the response of multi-pixel photon counters to low light levels. *Nuclear Instruments and Methods in Physics Research Section A: Accelerators, Spectrometers, Detectors and Associated Equipment*, 656:69–83, 2011.
- [38] Y. Itow et al. The JHF-kamioka neutrino project. 2001.
- [39] R. Brun and T. Rademakers. ROOT: An object oriented data analysis framework. *Nucl. Instrum. Meth.*, A389:81–86, 1997.

- [40] S. Agostinelli et al. GEANT4: A Simulation toolkit. *Nucl. Instrum. Meth.*, A506:250–303, 2003.
- [41] Yoshinari Hayato. A neutrino interaction simulation program library NEUT. *Acta Phys. Polon.*, B40:2477–2489, 2009.
- [42] Omar Benhar and Adelchi Fabrocini. Two nucleon spectral function in infinite nuclear matter. *Phys. Rev.*, C62:034304, 2000.
- [43] G. D. Megias, T. W. Donnelly, O. Moreno, C. F. Williamson, J. A. Caballero, R. González-Jiménez, A. De Pace, M. B. Barbaro, W. M. Alberico, M. Nardi, and J. E. Amaro. Meson-exchange currents and quasielastic predictions for charged-current neutrino- ^{12}C scattering in the superscaling approach. *Phys. Rev. D*, 91:073004, Apr 2015.
- [44] C. Andreopoulos et al. The GENIE Neutrino Monte Carlo Generator. *Nucl. Instrum. Meth.*, A614:87–104, 2010.
- [45] A. Bodek and J.L. Ritchie. Further Studies of Fermi Motion Effects in Lepton Scattering from Nuclear Targets. *Phys. Rev.*, D24:1400, 1981.
- [46] V Lyubushkin et al. A Study of quasi-elastic muon neutrino and antineutrino scattering in the NOMAD experiment. *Eur. Phys. J.*, C63:355–381, 2009.
- [47] G. A. Fiorentini et al. Measurement of Muon Neutrino Quasielastic Scattering on a Hydrocarbon Target at E3.5GeV. *Phys. Rev. Lett.*, 111:022502, 2013.
- [48] G. D’Agostini. A Multidimensional unfolding method based on Bayes’ theorem. *Nucl. Instrum. Meth.*, A362:487–498, 1995.
- [49] G. D’Agostini. Improved Iterative Bayesian Unfolding. *arXiv preprint*.
- [50] J. S. Lilley. *Nuclear physics: principles and applications*. Wiley, 2001.
- [51] C. Patrignani et al. Review of Particle Physics. *Chin. Phys.*, C40(10):100001, 2016.
- [52] K Gilje. P θ d geometry and mass. T2K Internal Use Only.
- [53] Tianlu Yuan. A double differential measurement of the flux averaged ν_μ cc 0π cross section on water. T2K Technote and Thesis.
- [54] Daniel Graham Ruterbories. *Measurement of the total flux averaged neutrino induced neutral current elastic scattering cross section with the T2K Pi-Zero detector*. PhD thesis, Colorado State U., 2014.
- [55] K. et al Abe. Measurements of neutrino oscillation in appearance and disappearance channels by the t2k experiment with 6.6×10^{20} protons on target. *Phys. Rev. D*, 91:072010, Apr 2015.

- [56] Callum Wilkinson. NEUT development for T2K and relevance of updated 2p2h models. *PoS*, NUFACT2014:104, 2015.
- [57] P. A. Rodrigues et al. Identification of nuclear effects in neutrino-carbon interactions at low three-momentum transfer. *Phys. Rev. Lett.*, 116:071802, 2016.
- [58] F. Capozzi, E. Lisi, A. Marrone, D. Montanino, and A. Palazzo. Neutrino masses and mixings: Status of known and unknown 3ν parameters. *Nucl. Phys.*, B908:218–234, 2016.
- [59] P. A. R. Ade et al. Planck 2013 results. XVI. Cosmological parameters. *Astron. Astrophys.*, 571:A16, 2014.